N

Lawrence Berkeley Laboratory
UNIVERSITY OF CALIFORNIA

Materials & Molecular
Research Division

MASTER

MEASUREMENT OF THE PARITY NONCONSERVING NEUTRAL WEAK INTERACTION IN ATOMIC THALLIUM

Philip Howard Bucksbaum
(Ph.D. thesis)

November 1980

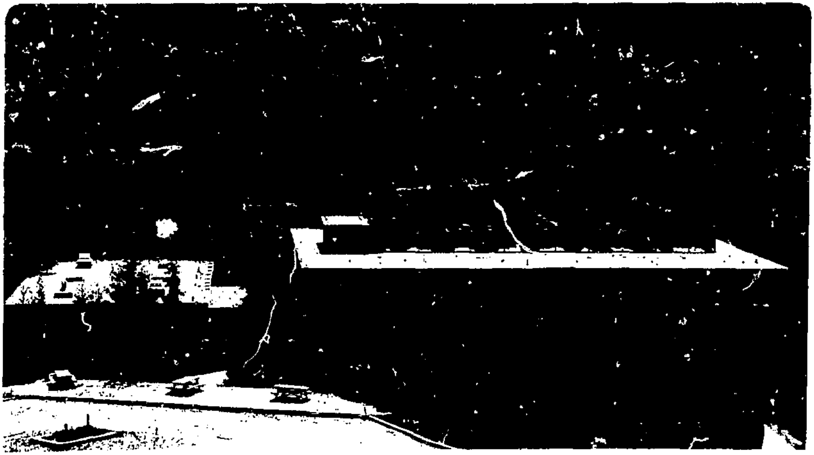

Prepared for the U.S. Department of Energy under Contract W-7405-ENG-48

MEASUREMENT OF THE PARITY NONCONSERVING NEUTRAL WEAK INTERACTION IN ATOMIC THALLIUM

Contents

APPENDIX. COMPUTER PROGRAMS

ACKNOWLEDGEMENTS

Eugene Commins has contributed time, effort, and ideas to every aspect of this experiment. Over the past 5 years he has been my principal advisor, teacher, and co-worker, as well as a good friend.

I also wish to thank:

Steven Chu and Ralph Conti, who taught me how to do experimental physics;

David Neuffer, our sleepy theorist;

Larry Hunter, who has worked closely with me during the past two years;

Persis Drell, for assistance and much encouragement;

Dane Anderberg and Bob Hamilton, both expert glassblowers;

The Atomic Physics Group: Richard Marrus, Mike Prior, and Howard Shugart;

The many members of the University of California, Berkeley, Physics Department and the Lawrence Berkeley Laboratory, whose collective knowledge and expertise have helped solve hundreds of technical problems: John Davis, Al Daft, Ken Grove, Ed Colledge, and graduate students in the Clark, Davis, Hahn, Jeffrie Kerth, Packard, and Shen groups, to name only a few.

I thank Linda Billard for typing this manuscript, and for helpful editorial suggestions.

This work was supported by the Chemical Sciences Division, Office of Basic Energy Sciences, U. S. Department of Energy, contract No. W-7405-ENG-48, through the Molecular Materials Research Division of the Lawrence Berkeley Laboratory. I received additional support from a National Science Foundation Graduate Fellowship Award during the 3 years 1975-1978.

Finally, I wish to thank my wife, Dessa, and my family, who have always enthusiastically supported me.

This thesis is dedicated to the memory of my mother, Corinne S. Bucksbaum, and her father, I. W. Schlass.

MEASUREMENT OF THE PARITY NONCONSERVING NEUTRAL WEAK INTERACTION IN ATOMIC THALLIUM

Philip Howard Bucksbaum

Lawrence Berkeley Laboratory, University of California
Berkeley, California 94720

ABSTRACT

This thesis describes an experiment to measure parity nonconservation in atomic thallium. A frequency doubled, flashlamp pumped tunable dye laser is used to excite the $6P_{1/2}(F = 0) \rightarrow 7P_{1/2}(F = 1)$ transition at 292.7 nm, with circularly polarized light. An electrostatic field E of 100-300 V/cm causes this transition to occur via Stark induced electric dipole. Two field free transitions may also occur: a highly forbidden magnetic dipole M, and a parity nonconserving electric dipole $\mathcal{E}_p$. The latter is presumed to be due to the presence of a weak neutral current interaction between the 6p valence electron and the nucleus, as predicted by gauge theories which unite the electromagnetic and weak interactions. Both M and $\mathcal{E}_p$ interfere with the Stark amplitude βE to produce a polarization of the $7P_{1/2}$ state. We measure this with a circularly polarized infrared laser beam probe, tuned to the $7P_{1/2} \rightarrow 8S_{1/2}$ transition. This selectively excites $m_F = +1$ or -1 components of the $7P_{1/2}$ state, and we see the polarization as an asymmetry in $8S \rightarrow 6P_{3/2}$ fluorescence when the probe helicity is reversed. The polarization due to M is $\Delta_M = -2M/(\beta E)$. We use it to calibrate the analyzing efficiency. The polarization due to $\mathcal{E}_p$ is $\Delta_p = 2i\mathcal{E}_p/(\beta E)$, and can be distinguished from Δ_M by its properties under reversal of the 292.7 nm photon

helicity and reversal of the laser direction. A preliminary measurement yielded a parity violation in agreement with the gauge theory of Weinberg and Salam (Conti et al., 1979).

Work in the past 2 years has focused on identifying, measuring, and eliminating all sources of systematic errors, in order to make a 25 percent measurement of $\mathcal{E}_p$. Chapter IV is an exhaustive study of the systematics. This work is now complete, and a precision measurement is now underway. Substantial changes in the apparatus and the running procedure have been implemented to reduce systematics, and these are explained in Chapter III. The data which have been used in these investigations are summarized in Chapter V.

CHAPTER I: PARITY NONCONSERVATION INDUCED BY THE WEAK NEUTRAL INTERACTION

"L'uivers est dissymétrique."--Louis Pasteur

A. Introduction

This is the report of a search for parity nonconserving neutral weak processes in atomic thallium. When the experiment was first planned by Eugene Commins, Steven Chu, and Ralph Conti in late 1974, scattering interactions of the type $\nu_\mu + N \rightarrow \nu_\mu + X$ had recently been reported at CERN (Hasert et al., 1973) and Fermilab (Benvenuti et al., 1974). These were consistent with the model of weak interactions in which a heavy neutral spin 1 (vector) bozon (Z^0) is exchanged between a neutrino (ν_μ) and a quark-parton within a nucleon (N), as in the Feynman diagram below:

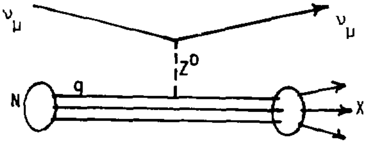

Figure I.1. A neutrino scatters from a quark in a nucleus. The bubbles represent strong interactions.

Neutral weak processes had never been observed before, but they had been predicted by gauge theories which unify the weak and electromagnetic interactions.

Since then, many different types of neutral current interactions have been observed, and the properties of Z^0 are found to be in good agreement with the particular gauge theory proposed by Weinberg and Salam (see Section I.C). The most unusual property of Z^0 exchange is the violation of parity, which was first discovered in the reaction $e + N \rightarrow e + N$ by Prescott et al. (1978), and shortly thereafter by Barkov et al. (1979), and by us (Conti et al., 1979).

B. Parity Nonconservation in Atoms

Parity is the symmetry of a physical system with respect to spatial inversion (vector $V \rightarrow -V$). A simple mirror image is a parity inversion combined with a rotation. The study of parity in nature has a rich history. Two books on this subject are by Gardner (1964) and Sakurai (1964). Although we will assume the reader is familiar with the basic concept of parity invariance, a few comments may help to clarify the rest of the discussion.

Parity noninvariance (or "nonconservation," or "violation") is far more common than parity invariance in our everyday environment. In most cases, this is simply a consequence of geometry, not of elementary forces. The mirror image of the world would work just the same. (There are even rare cases of people with all their internal organs mirror-inverted from normal (Newman, 1940). One hesitates to call this abnormal, since it seems to cause no impairment.)

The simplest possible system which displays this geometrical handedness or "chirality," is a molecule which consists of four atoms, all different, such as ammonia-like NHDT:

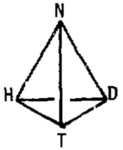

or

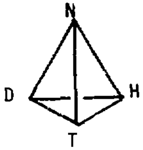

Even though the parity violation is not always visible on a macroscopic scale, chirality in molecules can often be detected. For instance, d-tartaric acid, a derivative of grapes, is a chiral molecule which rotates the plane of linearly polarized light to the right, whereas its mirror image ℓ-tartaric acid rotates the polarization to the left. (This fact, first discovered by Louis Pasteur, was the motivation for the quote which begins the chapter.) However, the size, mass, and energy levels of the two molecules are still identical unless the fundamental forces within and between the atoms violate parity (Harris et al., 1978).

A single atom does not have geometrical handedness, so it is a good place to look for weak induced parity violation. An atom is held together by the electrostatic Coulomb potential $\Phi(\vec{r}) = q_1 q_2/|r|$, which is symmetric under parity inversion operation $\underline{P}[\Phi(\vec{r})] \equiv \Phi(-\vec{r})$. It is easy to show that if the atomic Hamiltonian H contains only symmetric potentials $V(\vec{r}_1 \ldots \vec{r}_i) = V(-\vec{r}_1 \ldots -\vec{r}_i)$ then H commutes with

$\underline{P}$. Furthermore, since $[H,\underline{P}] = 0$, the eigenstates $|u_n(\vec{r})\rangle$ of H are eigenstates of $\underline{P}$ with eigenvalues ±1. The probability density $\langle u_n|u_n\rangle$ is inversion symmetric. If we introduce another term H_P to the Hamiltonian which does not commute with $\underline{P}$, the parity invariance is broken. This is the effect of neutral weak Z^0 exchange between the nucleus and the electrons in an atom. The Feynman diagrams representing first order weak and electromagnetic processes interfere, producing parity violation (Fig. I.2).

We may separate the eigenvectors $|u_n\rangle$ into two groups according to the $\underline{P}$ eigenvalues: $|\psi_n\rangle$ for $P = -1$, and $|\chi_m\rangle$ for $P = +1$. H_W, which is responsible for Z^0 exchange may be broken into scalar and pseudoscalar parts H_S and H_P according to their parity transformation properties: $\underline{P}H_S\underline{P}^{-1} = H_S$; $\underline{P}H_P\underline{P}^{-1} = -H_P$. Only H_S commutes with $\underline{P}$. H_P will cause the $|\psi_n\rangle$ to mix with the $|\chi_m\rangle$. To first order

$$|\psi_n\rangle \to |\overline{\psi_n}\rangle = |\psi_n\rangle \pm \sum_m \frac{|\psi_m\rangle\langle\chi_m|H_P|\psi_n\rangle}{E_n - E_m} \quad . \tag{I-1}$$

The ± sign refers to the handedness of the coordinate system, which determines whether H_P or $-H_P$ appears.

The precise form of H_P must be determined from experiment. We assume that Z^0 exchange reduces to a Fermi type current-current interaction at small momentum transfers found in atoms. The requirements for a "zero range" potential is that $\hbar/M_{Z^0}c \ll a_0 = \hbar^2/m_e e^2$, thus that $M_{Z^0} \gg m_e e^2/\hbar c = m_e\alpha$ and $M_{Z^0}c^2 \gg m_e c^2\alpha$. The most general expression for H_P will contain scalar (S), pseudoscalar (P), vector (V), axial vector (A), and tensor (T) terms:

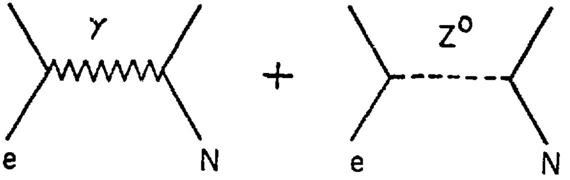

XBL 801-4572

Figure I.2 Feynman diagrams which interfere to cause parity nonconservation in atomic processes.

$$H_P = \sum_{V,A,S,P,T} \frac{1}{\sqrt{2}} G_F C_k (\bar{\psi}_N \Gamma_k \psi_N)(\bar{\psi}_e \Gamma_k \gamma_5 \psi_e) \quad . \tag{I-2}$$

where G_F is the Fermi coupling constant, 1.15×10^{-5} GeV^{-2}.

The more familiar charged weak interactions, in which it is believed that a heavy charged boson $W^{\pm}$ is exchanged, have been known to violate parity for over 20 years (Lee and Yang, 1956; Wu et al., 1957). The vector properties of the charge changing leptonic and hadronic weak currents analogous to Eq. (I-2) have been studied extensively (see Commins, 1973) and are found to be nearly pure "V - A." That is, $C_V = 1$, $C_A =$ (-1 for leptons, -1.25 for hadrons). This type of current violates both P and C (charge conjugation) but is even under T (time reversal).

The C_P term in Eq. (I-2) corresponds to $\Gamma_P = \gamma^5$, and thus vanishes in the nonrelativistic limit of the nucleon current. Hinds et al. (1976) and Sandars (1968) have shown that C_S and C_T are T-odd, and lead to permanent electric dipole moments in atoms. These would cause linear Stark shifts, and experimental searches in Tl, Xe, and Cs place an upper limit on C_S and C_T of 10^{-3} G_F (Hinds et al., 1976, Player and Sandars 1970, Bouchiat 1975, Gould 1970). We will therefore ignore all contributions to H_P except C_V and C_A. Rewriting these, and continuing to ignore momentum dependent additional terms, one obtains:

$$H = H_P^{(1)} + H_P^{(2)} \tag{I-3}$$

$$H_P^{(1)} = \frac{G_F}{\sqrt{2}} C_V \bar{\Psi}_e \gamma_\lambda \gamma_5 \psi_e \bar{\Psi}_N \gamma^\lambda \psi_N = \frac{G}{\sqrt{2}} \bar{\Psi}_e \gamma_\lambda \gamma_5 \psi_e \left[\sum_i C_{1p} \bar{\Psi}_{pi} \gamma^\lambda \psi_{pi} \right.$$

$$\left. + \sum_i C_{1n} \bar{\Psi}_{ni} \gamma^\lambda \psi_{ni} \right] \tag{I-4}$$

$$H_P^{(2)} = \frac{G_F}{\sqrt{2}} C_A \bar{\Psi}_e \gamma_\lambda \psi_e \bar{\Psi}_N \gamma^\lambda \gamma^5 \psi_N = \frac{G_F}{\sqrt{2}} \bar{\Psi}_e \gamma_\lambda \psi_e \left[\sum_i C_{2p} \bar{\Psi}_{pi} \gamma^\lambda \gamma^5 \psi_{pi} \right.$$

$$\left. + \sum_i C_{2n} \bar{\Psi}_{ni} \gamma^\lambda \gamma^5 \psi_{ni} \right] \quad . \tag{I-5}$$

C_{1p}, C_{1n}, C_{2p}, and C_{2n} refer to couplings to protons or neutrons. The sums are taken over all the nucleons in the nucleus. The Weinberg-Salam model predicts

$$C_{1n} = -1/2 \tag{I-6a}$$

$$C_{1p} = 1/2 - 2 \sin^2\theta_W \tag{I-6b}$$

$$C_{2n} = -(g_A)(1/2 - 2 \sin^2\theta_W) \tag{I-6c}$$

$$C_{2p} = +(g_A)(1/2 - 2 \sin^2\theta_W) \tag{I-6d}$$

$$g_A = 1.25 \quad .$$

θ_W, the weak coupling angle, or "Weinberg" angle (Weinberg 1972) is determined only by experiment, although some recent gauge theories attempt to predict it (e.g., Fairlie 1979). In this thesis the Sakurai (1979) value $\sin^2\theta_W = 0.23$ will be used. This is based on an average over experimental data from all neutral current experiments through 1978.

Although the actual thallium calculations involved a fully relativistic treatment of the atomic wavefunctions, it is instructive to perform a nonrelativistic reduction of Eqs. (I-4) and (I-5). Inserting Eq. (I-6), we have

$$H_P^{(1)} = \frac{G_F}{2\sqrt{2}} [(1 - 4 \sin^2\theta_W)Z - N] \, \bar{u}_e\gamma_\lambda\gamma_5 u_e \bar{\psi}_n \gamma^\lambda \psi_N \qquad (1\text{-}7)$$

$$\bar{\psi}_N \gamma^\lambda \psi_N \rightarrow \chi_N^\dagger \chi_N \quad \text{for} \quad \lambda = 0$$

$$\rightarrow 0 \quad \text{for} \quad \lambda = 1,2,3$$

$$\bar{u}_e\gamma_\lambda\gamma_5 u_e \rightarrow \chi_e^\dagger \frac{\vec{\sigma}\cdot\vec{p}}{2m_e} \chi_e + \left(\frac{\sigma\cdot p}{2m_e} \chi_e\right)^\dagger \chi_e \quad \text{for} \quad \lambda = 0 \quad ,$$

where χ is the two component Pauli wavefunction. Since $\chi_N^\dagger\chi_N$ is non-zero only at the nucleus, it can be represented as a delta function. Then the interaction reduces to an effective potential

$$H_P^{(1)} = \int \chi_e^\dagger V_P^{(1)}(r) \; \chi_e d^3r \quad , \qquad (I\text{-}8)$$

where

$$V_P^{(1)} = \frac{G_F}{2\sqrt{2}} Q_W[\vec{\sigma}\cdot\vec{p}\delta^3(r) + \delta^3(\vec{r}) \; \vec{\sigma}\cdot\vec{p}] \qquad (I\text{-}9)$$

and

$$Q_W = (1 - 4\sin^2\theta_W)\,Z - N \quad . \tag{I-10}$$

The nonrelativistic reduction of $H_p^{(2)}$ yields

$$V_p^{(2)} = \frac{g_A G_F}{2\sqrt{2}} \quad (1 - 4\sin^2\theta_W)\ \vec{\sigma}\cdot\vec{\sigma}_N\ \vec{\sigma}\cdot\vec{p}\ \delta^3)r\_ + \delta^3(r)\ \vec{\sigma}\cdot\vec{\sigma}_n\ \vec{\sigma}\cdot\vec{p} \tag{I-11}$$

where σ_n is the nuclear spin.

The factor Q_W appears in $V_p^{(1)}$ because the electron size (de Broglie wavelength $\sim\hbar/|p|$) is much larger than the nuclear diameter, so that all nucleons add coherently to the effect. Bouchiat and Bouchiat (1975a) first pointed out that this gives rise to a Z^3 enhancement to the size of the parity violation, because the electron momentum at the nucleus times its density at the nucleus scales as Z^2, and Q_W scales as Z. The neutrons contribute more than 90 percent of $V_p^{(1)}$, because the factor $(1 - 4\sin^2\theta_W)$ in Q_W is only ~0.1.

$V_p^{(2)}$ is much smaller than $V_p^{(1)}$ for two reasons. First, the $(1 - 4\sin^2\theta_W)$ factor now multiplies the entire expression. Seconds, Q_W is not present, because the interaction involves nuclear spin, and the nucleon spins tend to cancel in pairs. For these reasons, our thallium experiment is only sensitive to $V_p^{(1)}$, and we only measure the coupling constant C_{1n} in Eq. (I-4).

C. Gauge Theories

Neutral currents are predicted by nonabelian gauge theories. We will only briefly outline this subject in the rest of this chapter, but many good reviews now exist (Abers and Lee 1973, S. Weinberg 1974, Beg and Sirlin 1974, J. Illiopoulos 1976, De Rujula 1975).

1. Local Gauge Invariance.

Gauge theories are based on the notion that the fundamental interactions between elementary particles are necessary consequences of a symmetry of nature: the invariance of a particle's equations of motion with respect to local gauge transformations on its wavefunction. A local gauge transformation is defined by

$$\psi(x_\mu) \rightarrow \psi'(x_\mu) = \psi(x_\mu)\, e^{i\alpha(x_\mu)} \qquad \text{(I-12)}$$

where α is a real function of x. This is analogous to the statement that conservation laws follow directly from invariance principles, (e.g., angular momentum conservation follows from rotational invariance).

For example, the Dirac Lagrangian density of a free electron is

$$\mathcal{L}_D = 1/2\ \bar{\psi}(i\gamma^\lambda \partial_\lambda - m)\,\psi - 1/2[i(\partial_\mu \bar{\psi})\,\gamma^\mu + m\,\bar{\psi}]\,\psi \quad . \qquad \text{(I-13)}$$

We now perform an infinitesimal gauge transformation on ψ:

$$\delta\psi = \psi' - \psi = i\alpha(x_\mu)\,\psi \quad . \qquad \text{(I-14)}$$

The Lagrangian $\mathcal{L}_D$ is not invariant under this transformation, but invariance is restored by adding a term

$$\mathcal{L}_I = -e\bar{\psi}\gamma^\mu\psi A_\mu(x_\mu) \tag{I-15}$$

provided that A_μ also transforms under the gauge transformation

$$\delta A_\mu(x_\mu) = -\frac{1}{e}\gamma_\mu\alpha(x_\mu) \tag{I-16}$$

Adding $\mathcal{L}_I$ to $\mathcal{L}_D$ is equivalent to replacing ∂_μ in $\mathcal{L}_D$ with the "covariant derivative" $\nabla_\mu = \partial_\mu + ieA_\mu$. If A_μ is the electromagnetic vector potential, and e is the electric charge, then we have just reproduced the electromagnetic coupling of the electron. $\mathcal{L}_I$ is the interaction Lagrangian, and Eq. (I-16) is a gauge transformation on A_μ, which leaves $\mathcal{L}_D + \mathcal{L}_I$ invariant. We may also add the term which corresponds to the energy of the field alone

$$\mathcal{L}_{EM} = -1/4\, F_{\mu\nu}F^{\mu\nu} \quad , \quad F_{\mu\nu} = \partial_\mu A_\nu - \partial_\nu A_\mu \quad , \tag{I-17}$$

which is also gauge invariant.

Electromagnetism is called an "abelian" gauge theory because successive gauge transformations commute. It turns out that this is equivalent to the statement that the electromagnetic quantum (photon) carries no charge, so that photons do not directly couple to each other.

2. The Yang-Mills Field. A gauge theory of weak interactions must include charged current processes such as β decay as well as neutral currents. We therefore define a new internal degree of freedom, weak isospin, and arrange quarks and leptons into weak isodoublets, such as:

$$\psi = \begin{bmatrix} \nu_e \\ e^- \end{bmatrix} \tag{I-18}$$

For example, electron capture is a weak isospin-flip process in which $e^- \rightarrow \nu_e$:

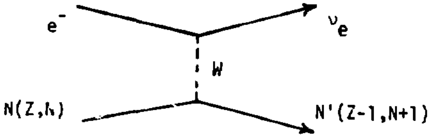

If we require ψ be invariant under local weak isospin gauge transformations [SU(2)], ψ is called a Yang-Mills field (Yang and Mills 1954). The local SU(2) gauge transformation is:

$$\delta\psi = \sum_i i\epsilon^i\left(\frac{\tau_i}{2}\right)\psi = i\tilde{\epsilon}\,\psi \quad , \tag{I-19}$$

where τ_i are 2x2 Pauli spin matrices, and ϵ^i is a function of x_μ. Gauge invariance is restored to $\mathcal{L}_D$ by the replacement

$$\partial_\mu \to \nabla_\mu = \partial_\mu + ig\tilde{A}_\mu \qquad \text{(I-20)}$$

where $\tilde{A}_\mu = \sum_i A_\mu^i(\tau_i/2)$, provided that

$$\partial\tilde{A}_\mu = -\frac{1}{g}\,\partial_\mu\tilde{\epsilon} + i[\tilde{\epsilon},\tilde{A}_\mu] \quad . \qquad \text{(I-21)}$$

The field energy term must also be gauge invariant:

$$\mathcal{L}_{YM} = -1/4\ f_{\mu\nu}f^{\mu\nu} \quad , \qquad \text{(I-22)}$$

where

$$f_{\mu\nu} = \partial_\mu\tilde{A}_\nu - \partial_\nu\tilde{A}_\mu + ig[\tilde{A}_\mu,\tilde{A}_\nu] \quad . \qquad \text{(I-23)}$$

The commutator term in Eq. (I-23), which has no analog in electromagnetism, implies that the weak isovector fields are themselves charged, so that $\mathcal{L}_{YM}$ contains A^3 and A^4 interactions. The commutators in the equations above also mean that successive infinitesimal gauge transformations do not commute; the Yang-Mills fields are nonabelian.

SU(2) and abelian [U(1)] gauge invariance can be simultaneously imposed by the replacement

$$\partial_\mu \to \nabla_\mu = \partial_\mu + ig\tilde{A}_\mu + ig'B_\mu \qquad \text{(I-24)}$$

in Eq. (I-13), where B_μ is the U(1) vector potential. When A^i_μ and B_μ are quantized, two charged quanta

$$\frac{1}{\sqrt{2}}(A^1_\mu \pm iA^2_\mu)$$

and two neutral quanta (A^3_μ, B_μ) appear. This is the basis of the SU(2)xU(1) weak/electromagnetic unified field theories. The vector fields A^i_μ and B_μ cannot be identical to the weak fields $W^\pm_\mu$ and Z^0_μ and the photon field A_μ, for several reasons:

(a) A^i_μ and B_μ are massless, but because of the short range of the weak interaction, $W^\pm$ and Z^0 must be massive.

(b) Charged weak interactions violate parity maximally. This means that $\mathcal{L}_D$ must be invariant under chiral gauge transformations

$$\delta\psi = i\left[\sum_i \gamma^5 \frac{\tau_i}{2} \eta^i(x_\mu)\right]\cdot\psi \quad . \tag{I-25}$$

(c) If (b) is satisfied, the mass term in $\mathcal{L}_D$ must be zero. So we not only have massless bosons, but massless fermions in the theory as well! Despite these problems, the Yang-Mills theory has one great technical advantage. It is renormalizable; the field theoretical calculations do not diverge.

3. Spontaneous Symmetry Breaking. All of these problems were eventually solved without sacrificing renormalizability. We will briefly describe spontaneous symmetry breaking, which gave mass to the weak bosons (Weinberg 1967, Salam 1968).

Let us add the following SU(2)xU(1) globally invariant Lagranian density to $\mathcal{L}_D$:

$$\mathcal{L}_G = (\partial_\mu \phi^\dagger)(\partial^\mu \phi) - \mu^2 \phi^\dagger \phi - \lambda(\phi^\dagger \phi)^2 \quad . \tag{I-26}$$

ϕ is an isodoublet of complex scalar fields

$$\phi = \begin{pmatrix} \dfrac{\phi_1 + i\phi_2}{\sqrt{2}} \\ \\ \dfrac{\phi_3 + i\phi_4}{\sqrt{2}} \end{pmatrix} \quad . \tag{I-27}$$

The fields ϕ need not be thought of as physical particles; this is just a mathematical guess. If $\mu^2 > 0$, then when ϕ is quantized, four real scalar fields appear, and the vacuum (lowest energy state) has $\phi = 0$. If $\mu^2 < 0$, the vacuum state is degenerate. After quantization, we have three massless scalar fields (Goldstone bosons) and one massive scalar field, $m = \sqrt{-2\mu^2}$. *If we require the new Lagrangian be invar*iant under local SU(2)xU(1) gauge transformations, an amazing thing happens: the Goldstone bosons disappear! In their place, three mass terms appear for the gauge fields. This is called the Higgs phenomenon (Higgs 1964). By introducing the ϕ fields, we have simultaneously *preserved renormalizability and created massive bosons. The price we* pay is the introduction of one massive "Higgs" boson. We define the neutral gauge fields using what is now standard notation:

$$g'/g \equiv \tan \theta_W \qquad \cdot \qquad \text{(I-28)}$$

$$Z^0_\mu = \cos \theta_W A^3_\mu - \sin \theta_W B_\mu \qquad \text{(I-29)}$$

$$A_\mu = \sin \theta_W A^3_\mu + \cos \theta_W B_\mu \qquad . \qquad \text{(I-30)}$$

θ_W is customarily called the Weinberg Angle. The new Lagrangian has the following properties:

A_μ appears as the electromagnetic vector potential. The electric charge is $e = g \sin \theta_W$. If W intermediates charged weak processes, then

$$\frac{G_F}{\sqrt{2}} = \frac{\lambda}{-2\mu^2} \qquad \text{(I-31)}$$

$$m_W^2 = \frac{\pi\alpha}{\sqrt{2}\, G_F \sin^2\theta_W} = \frac{(37.5 \text{ GeV})^2}{\sin^2\theta_W}$$

$$m_Z^2 = \frac{m_W^2}{\cos^2\theta_W} = \frac{4(37.5 \text{ GeV})^2}{\sin^2 2\theta_W} \qquad . \qquad \text{(I-33)}$$

4. Fermion Masses. The massive scalar Higgs boson which is created by spontaneous symmetry breaking remains a puzzling addition to the Lagrangian. It has not yet been identified with a real particle in nature. Even more curious is the fact that Higgs interactions can give mass to the massless fermions. It turns out that a Yukawa type coupling between the Higgs boson and the leptons is renormalizable, and can be gauge invariant. For example, if we consider a simplified

Lagrangian where the only fermions are e, μ, and their neutrinos ν_e and ν_μ, then it can be shown (Commins 1978) that the following new mass terms arise in the Lagrangian:

$$\mathcal{L}_M = [g_1\bar{e}e + g_2\bar{\mu}\mu + (h_1\cos^2\phi + h_2\sin^2\phi)\ \bar{\nu}_1\nu_1 + (h_1\sin^2\phi + h_2\cos^2\phi)\ \bar{\nu}_2\nu_2 \tag{I-34}$$

where

$$\begin{aligned} \nu_e &= \cos\phi\nu_1 + \sin\phi\nu_2 \\ \nu_\mu &= -\sin\phi\nu_1 + \cos\phi\nu_2 \end{aligned} \tag{I-35}$$

and η, g_1, g_2, h_1, h_2 are real constants which come from the Higgs couplings. Extension to theories with more lepton doublets (e.g., τ, ν_τ) is straightforward, but introduces more mixing angles.

Although only the first term in Eq. (I-34) has anything to do with atomic physics, we cannot resist digressing a bit to discuss the implications of the rest of the expression. If h_1 and h_2 are zero, neutrinos are massless. However, if not, then a new internal degree of freedom exists, the mixing angle ϕ. To understand its implications, consider the quark doublets in Eq. (I-36). There, d_c and s_c are each Cabibbo mixtures of the SU(3) flavor eigenstates d and s. In fact, the Cabibbo angle θ_c may arise in exactly the same way as the neutrino angle ϕ, when we give mass to the <u>quarks</u> in the Weinberg-Salam model through Higgs Yukawa couplings. Now, it is an experimentally determined fact that the flavor eigenstates are not weak SU(2) eigenstates; in other words θ_C is not equal to zero. We may therefore speculate that if neutrinos have mass, then the eigenstates of definite mass (ν_1 and ν_2) need not be the eigenstates of definite lepton number (ν_e and ν_μ)! Gribov and Pontecorvo (1976) have pointed out that this could give rise to neutrino oscillations in which $\nu_e \leftrightarrow \nu_\mu$, analogous to strangeness oscillations in $K^0\bar{K}^0$. Reines et al. (1980) are testing this with reactor produced neutrinos. Neutrino oscillations have been suggested as a mechanism to explain the deficiency in solar neutrinos detected by the experiment of Davis, Cleveland, and others (Fowler, 1977).

5. The Weinberg Salam Model. Parity nonconservation is not part of the theory at this point. However, it can be arranged by the isovector assignment of quarks and leptons. In the Weinberg Salam model, fermions exist in left handed isodoublets and right handed isosinglets (Glashow et al., 1970). For example, the electron field can be separated $e = e_L + e_R = 1/2(1 - \gamma_5)e + 1/2(1 + \gamma_5)\, e$. The isodoublet assignments reflect the observed charged weak couplings:

$$\begin{pmatrix}\nu_e \\ e\end{pmatrix}_L , \quad \begin{pmatrix}\nu_\mu \\ \mu\end{pmatrix}_L , \quad \begin{pmatrix}\nu_\tau \\ \tau\end{pmatrix}_L \qquad \text{Leptons}$$

$$\begin{pmatrix}u \\ d_C\end{pmatrix}_L , \quad \begin{pmatrix}c \\ s_C\end{pmatrix}_L , \quad \begin{pmatrix}t \\ b\end{pmatrix}_L \qquad \text{Quarks} \tag{I-36}$$

$$d_C = d \cos \theta_C + s \sin \theta_C \quad , \quad s_C = s \cos \theta_C - d \sin \theta_C \tag{I-37}$$

c = Cabibbo angle .

The right handed fields are all isosinglets: e_R, ν_{eR}, u_R, d_{cR}, etc.

The gauge field interactions in the Lagrangian may now be separated into three parts, corresponding to electromagnetic, charged weak, and neutral weak processes:

$$\mathcal{L}_{INT} = \mathcal{L}_{EM} + \mathcal{L}_{N} \tag{I-38}$$

$$\mathcal{L}_{EM} = -e\bar{\psi}\gamma^{\lambda}\psi A_{\lambda} = -eJ^{\lambda}_{EM}A_{\lambda} \quad ; \tag{I-39}$$

$$\mathcal{L}_{C} = -\frac{g}{2\sqrt{2}}\left(J^{\lambda+}_{C}W^{+}_{\lambda} + J^{\lambda-}_{C}W^{-}_{\lambda}\right) \quad , \tag{I-40}$$

where

$$J^{\lambda\pm}_{C} = \bar{\psi}\gamma^{\lambda}(1 - \gamma_5)\frac{\tau^{\pm}}{2}\psi \quad \text{and} \quad \tau^{\pm} = \tau_1 \pm i\tau_2 \quad ; \tag{I-41}$$

$$\mathcal{L}_{N} = -\frac{g}{2\cos\theta_W}J^{\lambda}_{N}Z_{\lambda} \tag{I-42}$$

where

$$J^{\lambda}_{N} = \bar{\psi}\gamma^{\lambda}(1 - \gamma_5)\frac{\tau_3}{2}\psi - 2\sin^2\theta_W J^{\lambda}_{EM} \quad . \tag{I-43}$$

We would like to apply $\mathcal{L}_N$ to the process of weak e – N coupling at zero momentum transfer since this is the relevant weak interaction in atoms. Following Weinberg (1972), we assume that the quarks contribute coherently in the nucleon. The amplitude for e – p elastic scattering is then

$$a(ep\rightarrow ep) = -\frac{G_F}{2\sqrt{2}}\,\bar{u}_e'\gamma_\lambda(1 - 4\sin^2\theta_W - \gamma_5)\,u_e\cdot\bar{u}_p'\gamma^\lambda(1 - 4\sin^2\theta_W - g_A\gamma_5)\,u_p\ ,$$

where g_A was defined in Eq. (I-6e). For e – n scattering, the amplitude is

$$a(en\rightarrow en) = +\frac{G_F}{2\sqrt{2}}\,\bar{u}_e'\gamma_\lambda(1 - 4\sin^2\theta_W - \gamma_5)\,u_e\cdot\bar{u}_n'(1 - g_A\gamma_5)\,u_n\ . \quad \text{(I-45)}$$

The couplings in Eq. (I-6) come from these amplitudes.

D. Experimental Determination of Neutral Current Couplings

Several other experiments are also searching for parity nonconservation in the neutral weak coupling. High energy inelastic polarized electron scattering at SLAC (Prescott et al., 1978) has had the most spectacular success so far. Atomic physics experiments are underway in Bismuth at Oxford (Baird et al., 1977), Seattle (Lewis et al., 1977), Novosibirsk (Barkov et al., 1979), and Moscow (Sobel'man et al., 1980). All heavy atom experiments are sensitive only to C_{1n} (see Eq. (I-4)). Experiments in hydrogen which, although much more difficult, potentially can measure all four couplings in Eq. (I-6), are also underway at the University of Michigan, University of Washington, and Yale. These are summarized in Commins and Bucksbaum (1980).

The results of electron scattering and atomic physics experiments (eq sector) may be combined with neutrino-nucleon (νq) and neutrino-electron (νe) scattering data to provide a stringent test of neutral weak interaction theories. In carrying out this analysis it is useful to begin with the simplest possible model-independent assumptions (Hung and Sakurai 1979, Sakurai 1979). Thus we start merely by assuming μe universality, that the contributions of heavy quarks c,s,... may be neglected, and that all neutral weak currents possess only vector and axial vector components. We may then write the effective Hamiltonians:

$$H_{\nu q} = -\frac{G_F}{\sqrt{2}}\,\bar{\nu}\gamma_\lambda(1-\gamma_5)\,\nu\Big\{1/2[\bar{u}\gamma_\lambda(\alpha-\beta\gamma_5)\,u - \bar{d}\gamma_\lambda(\alpha-\beta\gamma_5)\,d]$$

$$+ 1/2[\bar{u}\gamma_\lambda(\gamma-\delta\gamma_5)\,u + \bar{d}\gamma_\lambda(\gamma-\delta\gamma_5)]\Big\} \quad ; \qquad \text{(I-46)}$$

$$H_{\nu e} = -\frac{G_F}{\sqrt{2}}\,[\bar{\nu}_\mu\gamma_\lambda(1-\gamma_5)\,\nu_\mu][\bar{e}(g_V\gamma_\lambda - g_A\gamma_\lambda\gamma_5)\,e] \quad ; \qquad \text{(I-47)}$$

$$H_{eq} = -\frac{G_F}{\sqrt{2}}\Big\{\bar{e}\gamma_\lambda\gamma_5 e\Big[\frac{\tilde{\alpha}}{2}\,(\bar{u}\gamma_\lambda u - \bar{d}\gamma_\lambda u) + \frac{\tilde{\gamma}}{2}\,(\bar{u}\gamma_\lambda u + d\gamma_\lambda^{-}d)\Big]$$

$$+ \bar{e}\gamma_\lambda e\Big[\frac{\tilde{\beta}}{2}\,(\bar{u}\gamma_\lambda\gamma_5 u - \bar{d}\gamma_\lambda\gamma_5 d) + \frac{\tilde{\delta}}{2}\,(\bar{u}\gamma_\lambda\gamma_5 u + \bar{d}\gamma_\lambda\gamma_5 d)\Big]\Big\} \quad . \qquad \text{(I-48)}$$

The ten coupling constants $\alpha,\beta,\ldots\tilde{\beta},\tilde{\delta}$ must be determined by experiment. Note that Eq. (I-48) reduces to Eqs. (I-4) and (I-5) provided

$$C_{1p} = -1/2(3\tilde{\gamma} + \tilde{\alpha}) \quad , \quad C_{1n} = -1/2(3\tilde{\gamma} - \tilde{\alpha}) \quad , \qquad \text{(I-49)}$$

which follow from the assumption that $p = 2u + d$, $n = 2d + u$.

The neutrino-nucleon scattering data yield values of α, β, γ, and δ which are determined up to an overall sign ambiguity. These are listed in Table I-1, column 1. For a review of neutrino-scattering, see Cline and Fry (1977). Note that β is determined from a recent measurement of the cross section for

$$\bar{\nu}_e + D \rightarrow \bar{\nu}_e + n + p \qquad \text{(I-50)}$$

in which low-energy electron-antineutrinos are employed (Pasierb et al., 1979). In $\bar{\nu}_e + e \rightarrow \bar{\nu}_e + e$ charged and neutral currents can participate. All other neutrino scattering experiments have so far utilized high energy ν_μ or $\bar{\nu}_\mu$.

The coupling constants g_V, g_A for ν_e scattering have now been measured to be:

$$\begin{aligned} g_A &= -0.52 \pm 0.06 \\ g_V &= 0.06 \pm 0.08 \quad . \end{aligned} \qquad \text{(I-51)}$$

Actually there is an ambiguity involving $g_A \leftrightarrow g_V$ here; we have written the "axial vector dominant" solution.

Next, the results of the SLAC electron scattering experiment;

Table 1-1. Determination of Neutral-Current Coupling Parameters (from Sakurai 1979)[c]

Parameter	Model Independent[a]	Fractorization Dependent[b]	W-S Model	W-S Model, $\sin^2\theta_W = 0.23$
α	$\pm0.58\pm0.14$	0.58 ± 0.14	$1-2\sin^2\theta$	0.54
β	$\pm0.92\pm0.14$	0.92 ± 0.14	1	1
γ	$\pm0.28\pm0.14$	-0.28 ± 0.14	$-\frac{2}{3}\sin^2\theta$	-0.153
δ	$\pm0.06\pm0.14$	0.06 ± 0.14	0	0.0
g_V	0.00 ± 0.18	0.03 ± 0.12	$-\frac{1}{2}(1-4\sin^2\theta)$	-0.04
	or -0.52 ± 0.13			
g_A	-0.56 ± 0.14	-0.56 ± 0.14	$-\frac{1}{2}$	-0.5
	or -0.07 ± 0.15			
$\bar{\alpha}$	-0.72 ± 0.25	-0.72 ± 0.25	$-(1-2\sin^2\theta)$	-0.54
$\bar{\beta}$	----	0.06 ± 0.21	$-(1-4\sin^2\theta)$	-0.08
$\tilde{\gamma}$	0.38 ± 0.28	0.38 ± 0.28	$\frac{2}{3}\sin^2\theta$	0.153
$\tilde{\delta}$	----	0.00 ± 0.02	0	0.0
$\bar{\alpha}+\frac{1}{3}\tilde{\gamma}$	-0.60 ± 0.16	-0.60 ± 0.16	$-(1-\frac{20}{9}\sin^2\theta)$	-0.489
$\tilde{\beta}+\frac{1}{3}\bar{\delta}$	0.31 ± 0.51	0.06 ± 0.21	$-(1-4\sin^2\theta)$	0.08

---

[a] Coupling constants determined without recourse to factorization or gauge theory considerations.

[b] Coupling constants determined with factorization constants included.

[c] This table is explained fully in section D.

$$\tilde{\alpha} + \frac{\tilde{\gamma}}{3} = -0.60 \pm 0.16 \qquad \text{(I-52)}$$

$$\tilde{\beta} + \frac{\tilde{\delta}}{3} = 0.31 \pm 0.51 \quad . \qquad \text{(I-53)}$$

The results of the Novosibirsk and Berkeley Tl and Bi experiments: $Q_W(\mathrm{Bi}) = -140 \pm 40$ and $Q_W(\mathrm{Tl}) = -280 \pm 140$ are expressible in terms of $\tilde{\alpha}$ and $\tilde{\gamma}$ by means of the relation:

$$Q_W = -e\tilde{\gamma}(Z + N) + \tilde{\alpha}(Z - N) \quad . \qquad \text{(I-54)}$$

We plot the experimental constraints on $\tilde{\alpha}$ and $\tilde{\gamma}$ in Figure I.3. Thus we obtain:

$$\tilde{\alpha} = -0.72 \pm 0.25 \qquad \text{(I-55)}$$

$$\tilde{\gamma} = 0.38 \pm 0.28 \quad . \qquad \text{(I-56)}$$

Further restrictions on the coupling constants are obtained if one assumes a model with single Z^0 boson exchange (the "factorization" hypothesis). Assuming μe universality, this is characterized by seven independent parameters for coupling Z^0 to ν_L, $u_{L,R}$, $d_{L,R}$, and $e_{L,R}$. Since we started with ten parameters $\alpha, \beta, \ldots \tilde{\delta}$ there must be three independent "factorization" relations connecting the latter. Hung and Sakurai (1977) have shown these to be

Figure I.3 Results of the SLAC polarized electron experiment (a_1) and the Novosibirsk (Bi) and Berkeley (Tℓ) atomic physics experiments are plotted in the $\tilde{\alpha}$-$\tilde{\gamma}$ plane. The factorization hypothesis together with ν-hadron scattering data contain the allowed region of the $\tilde{\alpha}$-$\tilde{\gamma}$ plane as shown (from Sakurai 1979).

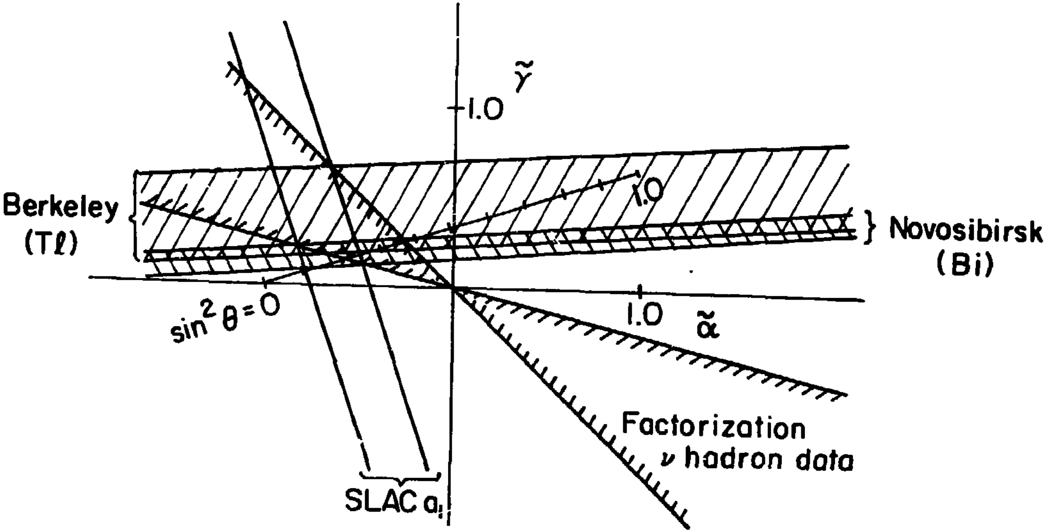

XBL801-4581

Fig. I.3

$$\tilde{\gamma}/\tilde{\alpha} = \gamma/\alpha \tag{I-57}$$

$$\tilde{\delta}/\tilde{\beta} = \delta/\beta \tag{I-58}$$

$$g_V/g_A = \alpha\tilde{\beta}/\tilde{\beta}\alpha \quad . \tag{I-59}$$

Let us plot the allowed values of γ/α from νq data (Table 1-1) in Fig. I.3 and utilize Eq. (I.57). Then we see that the SLAC and Bi, Tl results fall within the region permitted by νq data; this provides model-independent evidence for factorization.

Since $\tilde{\beta}$ and $\tilde{\delta}$ have not yet been separately determined, one cannot test Eq. (I-58) directly. However, combining Eqs. (I-57), (I-58), and (I-59), one obtains:

$$g_V/g_A = \frac{[\alpha + (\gamma/3)][\beta + (\delta/3)]}{[\tilde{\alpha} + (\tilde{\gamma}/3)][\tilde{\beta} + (\tilde{\delta}/3)]} \quad . \tag{I-60}$$

From Eqs. (I-52) and (I-53) one can determine the right hand side of Eq. (I-60). This determines that only the "axial-vector dominant" solution for g_V, g_A is acceptable in νe scattering, as we have written in Eq. (I-51).

One may make use of the SLAC experimental result [Eqs. (I-52) and (I-53)] and the factorization condition [Eq. (I-85)], with δ/β determined from νq data to obtain:

$$\tilde{\beta} = 0.29 \begin{smallmatrix} +0.55 \\ -0.51 \end{smallmatrix}$$

$$\tilde{\delta} = 0.02 \begin{smallmatrix} +0.17 \\ -0.06 \end{smallmatrix}$$

Another factorization relation:

$$\begin{Bmatrix} \tilde{\beta} \\ \tilde{\delta} \end{Bmatrix} = \begin{Bmatrix} \beta \\ \delta \end{Bmatrix} \frac{g_V}{g_A} \; \frac{\tilde{\alpha} + (\tilde{\gamma}/3)}{\alpha + (\gamma/3)}$$

yields more precise limits:

$$\tilde{\beta} = 0.06 \pm 0.21$$

$$\tilde{\delta} = 0.00 \pm 0.02$$

Now, the signs of the $\bar{\nu}_e e$ coupling constants g_V, g_A can be determined experimentally, since the neutral-current and charged-current amplitudes interfere. (We make a standard V-A choice of sign for the latter.) Also, the signs of the eq constants $\tilde{\alpha}$, $\tilde{\beta}$, $\tilde{\gamma}$, $\tilde{\delta}$ are determined because of interference with the electromagnetic amplitude of known sign. One cannot measure directly the absolute sign of νq coupling constants. However, it can be shown (Sakurai 1979) that the factorization hypothesis, together with the assumption that the coupling strength c_ν^2 in $\nu + \nu \rightarrow \nu + \nu$ is positive, removes the sign ambiguity in the νq constants. Table I-1 column 2 gives the present values of the ten coupling parameters which are thus obtained. The Weinberg-Salam model predictions of these parameters are also given in Table I-1 column 3, and it is clear that very satisfactory agreement is obtained for $\sin^2\theta_W = 0.23$ (column 4). However, it is obviously desirable and important to improve the precision of determination of the parameters, especially γ, δ, $\tilde{\beta}$, $\tilde{\gamma}$ and $\tilde{\delta}$. Better values of $\tilde{\gamma}$ will soon be obtained from heavy atom experiments within the next few years. Beyond this one may hope that various experiments will eventually shed light on small but important effects such as the electron-electron parity violating coupling, momentum-transfer dependent terms and higher order corrections to the Weinberg-Salam model. The latter would be particularly exciting to observe since the ability to predict them is one of the most important features of unified gauge field theories.

CHAPTER II: THALLIUM CALCULATIONS

A. Brief Description of the Experiment

Thallium is an 81 electron atom, with 80 electrons forming closed shells $1s^2 \ldots 5d^{10} 6s^2$. The remaining 6p valence electron participates in all the low-lying transitions, with minimal interconfiguration interactions. We may therefore idealize the atom as hydrogenic with a $6P_{1/2}$ ground state and a spin 1/2 nucleus. Although there are two natural isotopes, Tl^{205} and Tl^{203}, the nuclear magnetic moments are nearly identical, so the hyperfine splittings are almost the same. Also, the isotope shifts are smaller than the hfs splittings in the transitions of interest. Figure II.1 is a thallium level diagram.

Weak interactions between the nucleus and the valence electron perturb the atomic wavefunctions so that they are no longer eigenstates of the parity operator P. The ground state, which has odd parity under the influence of the electrostatic Coulomb interaction, will contain admixtures of $S_{1/2}$: $H = H_{EM} + H_W$; recall from Chapter I that H_W has scalar and speudoscalar parts, H_S and H_P:

$$|\overline{6P_{1/2}}\rangle \approx |6P_{1/2}\rangle + \sum_n \frac{\langle nS_{1/2}|H_P|6P_{1/2}\rangle}{E_n - E_{6P}} |nS_{1/2}\rangle \quad . \qquad \text{(II-1)}$$

Likewise $nS_{1/2}$ will be perturbed

$$|\overline{nS_{1/2}}\rangle \approx |nS_{1/2}\rangle + \sum_m \frac{\langle mP_{1/2}|H_P|nS_{1/2}\rangle}{E_m + E_n} |mP_{1/2}\rangle \qquad \text{(II-2)}$$

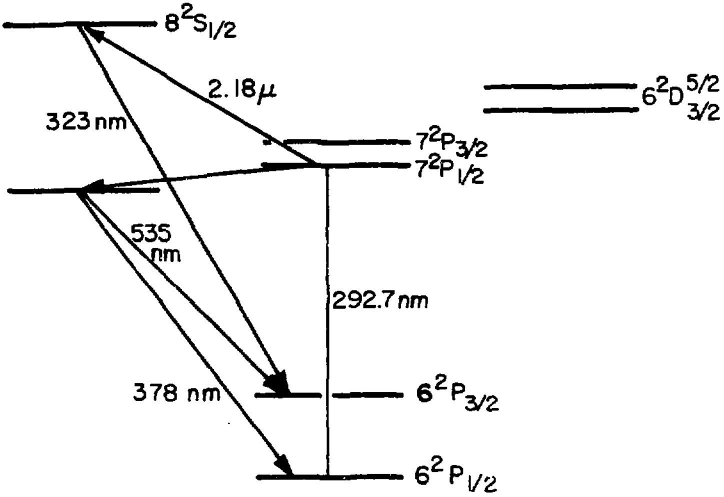

XBL807-5570

Figure II.1 Low lying levels of thallium.

The contributions of higher angular momentum states $P_{3/2}$, D, F, etc. may be ignored, since the perturbation H_W is a contact (delta function) interaction at low energies, so only those states with a significant overlap with the nucleus need be considered.

The pseudoscalar Hamiltonian H_p contributes to transition amplitudes too. Consider the transition $6P_{1/2} \rightarrow 7P_{1/2}$:

$$M(6P_{1/2} \rightarrow 7P_{1/2}) = -e\langle \overline{7P_{1/2}} | \vec{A}_{RAD} \cdot \vec{p} | \overline{6P_{1/2}} \rangle \quad ,$$

where A_{RAD} is the vector potential of a laser field with $\nu = 292.7$ nm. The electromagnetic amplitude is forbidden magnetic dipole ($\mathcal{M}$); it would be zero because of the orthogonality of the initial and final wavefunctions, in the absence of relativistic corrections and other small effects. But now there is a weak-induced electric dipole amplitude as well:

$$M = \langle \mathcal{M} \rangle + \langle \mathcal{E}_p \rangle \quad ,$$

$$\mathcal{E}_p = \sum_n \frac{\langle 7P_{1/2} | \hat{\varepsilon} \cdot \vec{r} | nS_{1/2} \rangle \langle nS_{1/2} | H_p^\dagger | 6P_{1/2} \rangle}{E_n + E_6}$$

$$+ \sum_n \frac{\langle 7P_{1/2} | H_p | nS_{1/2} \rangle \langle nS_{1/2} | \hat{\varepsilon} \cdot \vec{r} | 6P_{1/2} \rangle}{E_n - E_7} \quad . \qquad \text{(II-3)}$$

As an example, consider light which is circularly polarized

$$\hat{\epsilon}_{\pm} = \frac{1}{\sqrt{2}} (\hat{\epsilon}_x \pm i\hat{\epsilon}_y)$$

and traveling along with $\hat{z}$ axis. $\hat{\epsilon}_{\pm}$ represents photons with ±1 helicity; that is, $\langle \hat{\epsilon}_{\pm} \cdot \vec{r} \rangle = \langle r_{\pm} \rangle = \mp\langle d_{\pm} \rangle$ where d's are the components of a spherical tensor of rank 1. d_+ is proportional to a raising operator by the Wigner Eckhart Theorem, so $\hat{\epsilon}_+$ carries +1 unit of angular momentum. We dwell on this because the sign is important later.

The electric and magnetic dipole amplitudes for the transitions are

$$\langle M \rangle_{\pm} = \langle \overline{7P_{1/2}} | \hat{k}_z \times \hat{\epsilon}_{\pm} \cdot \vec{\mu} | \overline{6P_{1/2}} \rangle = \mp i \langle \mu_{\pm} \rangle = \mp i g_J \mu_0 \langle J_{\pm} \rangle \qquad \text{(II-4)}$$

$$\langle \mathcal{E}_p \rangle_{\pm} = \langle 7P_{1/2} | \hat{\epsilon}_{\pm} \cdot \vec{r} | \overline{6P_{1/2}} \rangle = \langle r_{\pm} \rangle = \mp \langle d_{\pm} \rangle \quad . \qquad \text{(II-5)}$$

Using the Wigner Eckhart Theorem again for j = 1/2,

$$\mp \langle j'm' | d_{\pm} | jm \rangle = \mp \langle 1/2\ m' | 1\ \pm 1\ 1/2\ m \rangle \langle f \| r \| i \rangle$$

$$= \sqrt{2/3}\ \delta_{jj'} \delta_{m\pm 1, m'} \langle f \| r \| i \rangle = \delta_{jj'} \delta_{m\pm 1, m'} \mathcal{E}_p \qquad \text{(II-6)}$$

$$\pm i \langle j'm' | J_{\pm} | jm \rangle = \pm \frac{i}{\sqrt{2}} \delta_{jj'} \delta_{m\pm 1, m'} \langle f | i \rangle = \pm i \delta_{jj'} \delta_{m\pm 1, m} M \quad . \qquad \text{(II-7)}$$

The transition rate for h = +1 is $|\mathcal{E}_p + iM|^2$ and the transition rate for h = -1 is $|\mathcal{E}_p - iM|^2$.

The circular dichroism δ is defined as the asymmetry in the transition rate $\sigma_\pm$ for alternating +1 or −1 helicity light:

$$\delta = \frac{\sigma_+ - \sigma_-}{\sigma_+ + \sigma_-} = \frac{-2i\ M\mathcal{E}_p}{|M|^2 + |\mathcal{E}_p|^2} = \frac{|\mathcal{E}_p + i\ M|^2 - |\mathcal{E}_p - i\ M|^2}{|\mathcal{E}_p - i\ M|^2 + |\mathcal{E}_p + i\ M|^2} \quad . \qquad \text{(II-8)}$$

It can be shown (Bouchiat 1974) that $\mathcal{E}_p$ must be purely imaginary if time reversal invariance is obeyed. Our sign convention throughout this thesis will always be that δ is calculated by adding the +1 helicity rates, and subtracting the −1 helicity rates. Whenever ± signs appear it is understood that the top sign is for h = +1 and the bottom sign is for h = −1. Note that

$$\delta \approx -\frac{2i\mathcal{E}_p}{M} = +\frac{2\ \mathrm{Im}\ \mathcal{E}_p}{M} \quad , \qquad \text{(II-9)}$$

since $\mathcal{E}_p \ll M$. δ for thallium has been calculated as

$\delta_{tneo} = +2.1 \times 10^{-3}$ (Neuffer, 1977; central field Thomas Fermi)
$\delta_{theo} = +2.0 \times 10^{-3}$ (Khriplovich, 1976;
semi-empirical extrapolation)

for $\sin^2\theta_W = 0.23$. A previous measurement by us yielded the value

$$\delta_{exp} = +(5.2 \pm 2.4) \times 10^{-3} \quad \text{(Conti 1979)} \quad .$$

Direct observation of the circular dichroism is impossible because of obscuring backgrounds ~10^3 times larger than $|M|^2$. Instead, we have resorted to a suggestion of M. and C. Bouchiat (1974), where we induce Stark effect transitions by means of an electric field. Figure II.2 shows the coordinate system we will use throughout this thesis. The 292.7 nm laser beam travels along the $+\hat{x}$ direction. An electric field is applied along the $\hat{y}$ axis, which may be reversed. What effects will parity nonconservation produce in this system? An equivalent question is to ask what pseudoscalars can be formed from the physically measurable quantities $\hat{\varepsilon}$, $\vec{k}$, h, $\vec{E}$, and $\vec{J}$ in the atomic system. h itself is a pseudoscalar; $h = \hat{\varepsilon}\times\hat{\varepsilon}^{*}\cdot\vec{k}/|k|$. That corresponds to the circular dichroism, already discussed. The expression we seek must correspond to the interference between the Stark induced and weak induced electric dipoles. It must therefore be even under T (time reversal operator) and not reverse with $\vec{k}$ (since electric dipole transitions do not depend on k). The only suitable pseudoscalar is h $\vec{k}\times\vec{E}\cdot\vec{J}$. Since $\vec{k}\times\vec{E}$ is the $\hat{z}$ direction, we predict that the weak interaction may produce a non-vanishing expectation value for J_z--that is, a polarization along $\hat{z}$--in the excited $7P_{1/2}$ state. That is exactly what happens.

Here, then, is a brief description of the experiment. Circularly polarized uv light at 292.7 nm enters a thallium vapor cell, traveling along $+\hat{x}$. An electric field has already been applied along $\pm\hat{y}$. The neutral weak interaction interferes with the Stark effect to produce a polarization along $\hat{z}$. The method we use to analyze this polarization

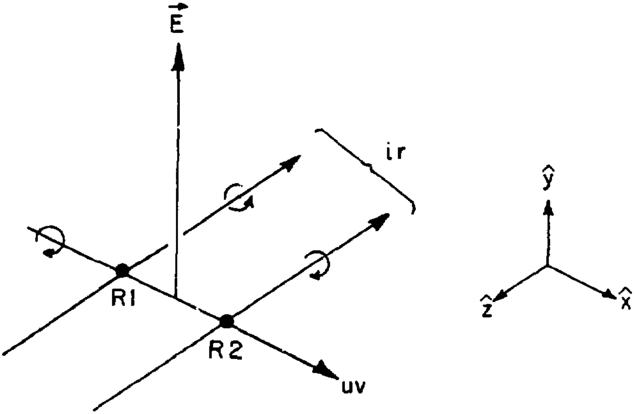

XBL 807-5571

Figure II.2 Coordinate system for the experiment.

is one of the unique features of the experiment. We could have simply analyzed the circular polarization of the fluorescent light emitted by the excited atoms as they cascade down to the ground state. The 535.0 nm fluorescence from $7S_{1/2} \rightarrow 6P_{3/2}$ decay is favorable for this (see Chu et al., 1977). But there is a twelve-fold reduction in the analyzed polarization, due to cascade depolarization and resonance trapping. Therefore, following a suggestion by R. Conti in 1977, we analyze the $7P_{1/2}$ polarization by selectively exciting the $m_J = +1/2$ or $-1/2$ components of this state to the $8S_{1/2}$ state, using circularly polarized light at 2.18μ traveling along the $\hat{z}$ axis. This gives us practically no reduction in analyzing power.

In the remainder of this chapter we will review the calculations, explaining the $8S_{1/2}$ optical pumping, and write down an expression for the polarization of the $7P_{1/2}$ state.

B. Thallium Calculations

M, $\mathcal{E}_p$, and the Stark effect have all been calculated by David Neuffer (1977a). He obtained the thallium wavefunctions by using a one electron central field (OECF) approximation. Neuffer modeled the $1s^2 \ldots 5d^{10}6s^2$ electron orbitals as a spherical "Tietz" potential (Tietz 1954) with an added exponential tail:

$$V(r) = \frac{e^2(Z-1)}{r(1+\epsilon r)^2} e^{-\gamma r} - \frac{e^2}{r} \quad . \qquad \text{(II-10)}$$

This potential is a good approximation to the solution of the Thomas Fermi Equation. The Dirac equation describing the motion of the remaining valence electron in the presence of V(r) was integrated numerically. The free parameters η and γ were chosen to fit the energy levels of the $6P_{1/2}$ and $7P_{1/2}$ states.

Neuffer checked the wavefunctions by comparing them to as many known values in thallium as possible: energy levels, hyperfine splittings, and oscillator strengths between higher S and D states and the ground state. The good agreement with known hyperfine splittings was particularly noteworthy, since they test the electron wavefunctions near the nucleus, where the neutral weak interactions also occur.

C. The Stark Effect

The excitation of thallium from $6P_{1/2} \rightarrow 7P_{1/2}$ in this experiment takes place mainly due to the Stark effect, which is induced by a static electric field of 100 to 300 V/cm in the vapor cell. The absorption rate due to the magnetic dipole transition alone is smaller by 10^{-5}, while the parity violating E1 rate is down by a factor 5×10^{-11}! The Stark amplitudes have been calculated, using wavefunctions generated by David Neuffer's modified Thomas-Fermi central field calculation. We also plan to determine it experimentally as an adjunct to our current work. Explanations of the Stark effect are found in Neuffer (1977a) as well as Chu (1976) and Conti (1979).

The presence of an electric field $\vec{E} = E\hat{y}$ perturbs the $6P_{1/2}$ and $7P_{1/2}$ states by means of the perturbation Hamiltonian $H' = -e\vec{E}\cdot\vec{r}$, mixing them with $S_{1/2}$ and $D_{3/2}$ states:

$$|\overline{NP_{1/2}}\rangle = |NP_{1/2}\rangle - \sum_{nS} \frac{|nS\rangle\langle nS|eEy|NP_{1/2}\rangle}{E_{NP_{1/2}} - E_{nS}} - \sum_{nD_{3/2}} \frac{|nD_{3/2}\rangle\langle nD_{3/2}|eEy|NP_{1/2}\rangle}{E_{NP} - E_{nD_{3/2}}} \qquad \text{(II-11)}$$

Parity conserving electric dipole transitions between $6P_{1/2}$ and $7P_{1/2}$, impossible in the field-free case, now dominate:

$$\langle\overline{7P_{1/2}}|H_{em}|\overline{6P_{1/2}}\rangle \approx \langle\overline{7P_{1/2}}|E1|\overline{6P_{1/2}}\rangle \propto e\langle\overline{7P_{1/2}}|\hat{\epsilon}\cdot\vec{r}|\overline{6P_{1/2}}\rangle$$

$$= e^2E \sum_{S,D_{3/2}} \left\{ \frac{\langle 7P_{1/2}|\hat{\epsilon}\cdot\vec{r}|n\rangle\langle n|y|6P_{1/2}\rangle}{E_{6P} - E_n} + \frac{\langle 7P_{1/2}|y|n\rangle\langle n|\hat{\epsilon}\cdot\vec{r}|6P_{1/2}\rangle}{E_{7P} - E_n} \right\} , \qquad \text{(II-12)}$$

Since $\vec{k} = k\hat{x}$ by definition of our coordinate axes, $\hat{\epsilon} = \cos\theta\hat{y} + e^{i\phi}\sin\theta\hat{z}$ is completely general. There are two different reduced Stark matrix elements corresponding to $\hat{\epsilon}\parallel\vec{E}(\alpha)$, and $\hat{\epsilon}\perp\vec{E}(\beta)$:

$$\alpha = \frac{e^2}{9} \sum_{nS} R_{7P,nS}R_{6P,nS}\left(\frac{1}{E_7 - E_{nS}} + \frac{1}{E_6 - E_{nS}}\right)$$

$$+ \frac{2e^2}{9} \sum_{nD_{3/2}} R_{7P,nD}R_{6P,nD}\left(\frac{1}{E_7 - E_{nD}} + \frac{1}{E_6 - E_{nD}}\right) \qquad \text{(II-13)}$$

$$\beta = \frac{e^2}{9} \sum_{nS} R_{7P,nS}R_{6P,nS}\left(\frac{1}{E_6 - E_{nS}} - \frac{1}{E_7 - E_{nS}}\right)$$

$$+ \frac{2e^2}{9} \sum_{nD_{3/2}} R_{7P,nD}R_{6P,nD}\left(\frac{1}{E_7 - E_{nD}} - \frac{1}{E_6 - E_{nD}}\right) \qquad \text{(II-14)}$$

$R_{nP,nL} = \langle nL|r|nP\rangle$ = a radial matrix element. The values obtained by Neuffer are

$$\alpha = 2.05 \times 10^{-5} \frac{|e|\hbar}{2m_e c} (\mathrm{V/cm})^{-1}$$

$$\beta = 1.78 \times 10^{-5} \frac{|e|\hbar}{2m_e c} (\mathrm{V/cm})^{-1}$$

An experimental measurement of α or β separately is difficult, since it requires accurate knowledge of laser intensity, thallium density, light collection efficiency, filter transmission, and phototube gains. The ratio β/α has been measured as 0.84 ± 0.05 (Chu et al., 1977) vs. Neuffer's prediction of 0.80.

The theoretical uncertainty of α and β, based on comparison of some of the dipole matrix elements with experimental values, is about 20 percent. The ultimate aim of this experiment is a determination of $\mathcal{E}_p/\beta$ to 25 percent, where $\mathcal{E}_p$ is the parity violating E1 amplitude.

Higher precision experiments will demand a more accurate β. By direct measurement of the most significant dipole matrix elements in the Stark mixing, we hope to improve β substantially.

The Stark amplitudes are given in Table II-1 for each hyperfine transition from $6P_{1/2}$ to $7P_{1/2}$.

D. Magnetic Dipole

The magnetic dipole amplitude M contains contributions from relativistic effects, interconfiguration interactions, orbit-orbit corrections and others, which are listed in Table II-2. Although its contribution to the total transition rate is completely dominated by the Stark effect, its interference provides the calibration for the size of $\mathcal{E}_p$. Consequently the first experiment in this research program was a measurement of M (Chu 1977a).

Unfortunately, the same large backgrounds which obscure the circular dichroism make the field free transition rate $\propto |M|^2$ very difficult to measure. Instead, a suggestion of Bouchiat and Bouchiat (1974) is employed: A static electric field is applied along $\hat{y}$, perpendicular to the laser beam along $\hat{x}$. As in the parity violating case, a polarization of the atom now occurs along $\hat{z}$, which is proportional to <u>two</u> scalars, $\hat{\epsilon}\times\vec{E}\cdot\vec{\kappa}\ \hat{\epsilon}\cdot\vec{J}$ and $\hat{\epsilon}\times\vec{J}\cdot\vec{\kappa}\ \hat{\epsilon}\cdot\vec{E}$, which describe separate M-Stark interference terms. The first, which requires $\hat{\epsilon}\perp\vec{E}$, involves the β Stark transitions from the $F = 0,1 \to F' = 1$ states. The second has $\hat{\epsilon}\parallel\vec{E}$, and only concerns the α $1 \to 1$ transitions. (The other two transitions, $0 \to 0$ and $1 \to 0$, have $\langle\vec{J}\rangle = 0$.)

Table II-1. Stark amplitudes $6P_{1/2} \to 7P_{1/2}$ for $\vec{E} = E\hat{y}$; $\hat{\epsilon} = \cos\theta\hat{y} + e^{i\phi}\sin\theta\hat{z}$.

	$6P_{1/2}(0,0)$	(1, -1)	(1,0)	(1,1)
$7P_{1/2}$ (0,0)	$\alpha E\cos\theta$	$-\beta E\frac{i}{\sqrt{2}}\sin\theta e^{i\phi}$	0	$\beta E\frac{i}{\sqrt{2}}e^{i\phi}\sin\theta$
(1,-1)	$-\beta E\frac{i}{\sqrt{2}}e^{i\phi}\sin\theta$	$\alpha E\cos\theta$	$-\beta E\frac{i}{\sqrt{2}}e^{i\phi}\sin\theta$	0
(1,0)	0	$-\beta E\frac{i}{\sqrt{2}}\sin\theta e^{i\phi}$	$\alpha E\cos\theta$	$-\beta E\frac{i}{\sqrt{2}}e^{i\phi}\sin\theta$
(1,1)	$\beta E\frac{i}{\sqrt{2}}e^{i\phi}\sin\theta$	0	$-\beta E\frac{i}{\sqrt{2}}e^{i\phi}\sin\theta$	$\alpha E\cos\theta$

Table II-2. M1 calculations of Neuffer (1977a): contributions to M in $6^2P_{1/2} \rightarrow 7^2P_{1/2}$ in thallium ($|\mu_0| = |e|\hbar/2m_ec$)

Relativistic		$-1.75 \times 10^{-5}\,|\mu_0|$
Interconfiguration interaction		$-1.9 \times 10^{-6}\,|\mu_0|$
"Lamb" correction		$-4 \times 10^{-7}\,|\mu_0|$
Orbit-orbit correction		$-1.20 \times 10^{-5}\,|\mu_0|$
Hyperfine mixing:		
	0 → 1	$+2.6 \times 10^{-6}\,|\mu_0|$
	1 → 0	$-2.6 \times 10^{-6}\,|\mu_0| \times \sqrt{1/3}$

Table II-3 shows the various M amplitudes for the $6P_{1/2} \rightarrow 7P_{1/2}$ transitions. Combining these with the Stark transitions in Table II-1, we find polarizations

$$P_{0-1} = -\frac{2M}{\beta E} \quad , \quad \propto \hat{\epsilon} \times \vec{E} \cdot \vec{k} \; \hat{\epsilon} \cdot \vec{J} \tag{II-15}$$

$$P_{1-1} = \frac{4M}{3\alpha E} \quad , \quad \propto \hat{\epsilon} \times \vec{J} \cdot \vec{k} \; \hat{\epsilon} \cdot \vec{E} \quad . \tag{II-16}$$

These are shown in Fig. II.3.

Figure II.4 summarizes the data from the M1 experiment. The experimental value for M is

$$M = -(2.3 \pm 0.3) \times 10^{-5} \frac{|e|\hbar}{2m_e c} \quad .$$

Neuffer predicts

$$M = -(3.2 \pm 1) \times 10^{-5} \frac{|e|\hbar}{2m_e c} \quad .$$

E. Weak Induced Electric Dipole $\mathcal{E}_p$

The electric dipole amplitude for $6P_{1/2} \rightarrow 7P_{1/2}$ is given by Eq. (II-3). The $6P_{1/2} \rightarrow nS$ dipole matrix elements can be experimentally determined, but the $7P_{1/2} \rightarrow nS$ matrix elements must be calculated. The weak perturbation $\langle \psi_f | H_p | \psi_i \rangle$ is the $V_N A_e$ part of the weak electron-nucleon current interaction discussed in Section A:

Table II-3: M1 amplitudes $6P_{1/2} \rightarrow 7P_{1/2}$ for $\vec{E} = E\hat{y}$; $\hat{\varepsilon} = \cos\theta\hat{y} + e^{i\phi}\sin\theta\hat{z}$.

$7P_{1/2}$	$6P_{1/2}(0,0)$	(1, -1)	(1,0)	(1,1)
(0,0)	0	$\frac{i}{\sqrt{2}} M \sin\theta e^{i\phi}$	$-M\cos\theta$	$\frac{i}{\sqrt{2}} M \sin\theta e^{i\phi}$
(1,-1)	$-\frac{iM}{2} e^{i\phi} \sin\theta$	$-M\cos\theta$	$-\frac{1}{2} M \sin\theta e^{i\phi}$	0
(1,0)	$-M\cos\theta$	$\frac{i}{\sqrt{2}} M \sin\theta e^{i\phi}$	0	$-\frac{i}{\sqrt{2}} M \sin\theta e^{i\phi}$
(1,+1)	$-\frac{i}{\sqrt{2}} \sin\theta e^{i\phi}$	0	$\frac{i}{\sqrt{2}} M \sin\theta e^{i\phi}$	$+M\cos\theta$

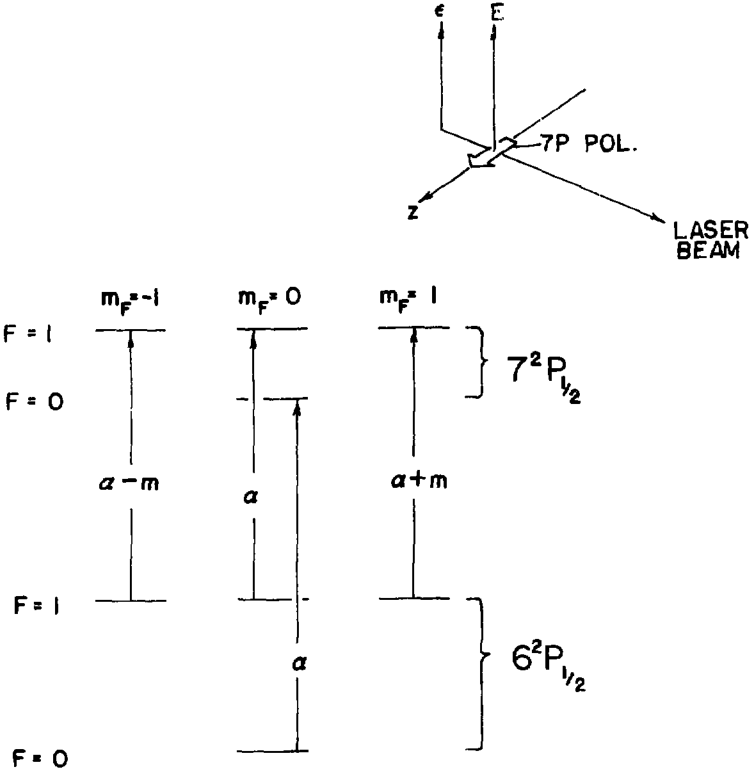

$$P_{1-1} = \frac{(a+m)^2 - (a-m)^2}{(a+m)^2 + (a-m)^2 + a^2} \cong \frac{4m}{3a}$$

$$P_{0-0} = 0$$

XBL 778-9840

Figure II.3 Stark and M1 amplitudes for $6P_{1/2} \rightarrow 7P_{1/2}$ in thallium.

(a) Transitions for laser polarization $\hat{\varepsilon} \parallel \vec{E}$.

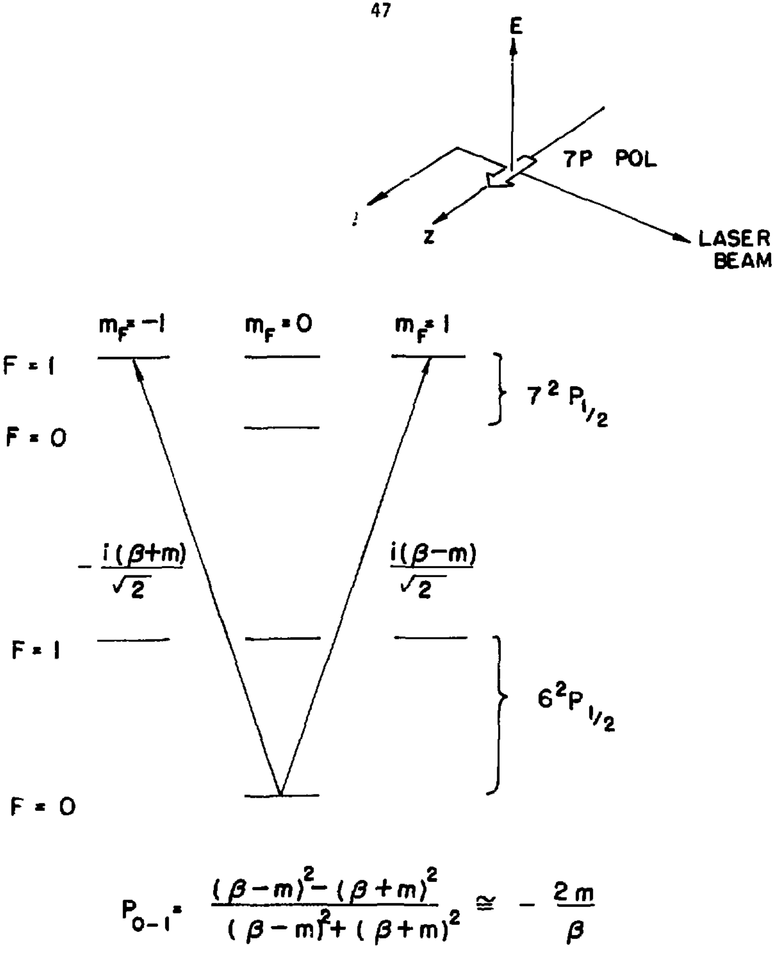

$$P_{0-1} = \frac{(\beta-m)^2-(\beta+m)^2}{(\beta-m)^2+(\beta+m)^2} \cong -\frac{2m}{\beta}$$

XBL 778-9845

Figure II.3 (b) (0→1) transitions for $\hat{\varepsilon} \perp \vec{E}$.

Figure II.4 Data from experiment to measure the Stark-M1 interference. Atomic polarization is plotted with respect to inverse electric field, for three hyperfine transitions, as indicated. Lines are least squares fits to the data. Theory predicts the slopes should be in the ratio $4/3\alpha : 0 : -2/\beta$.

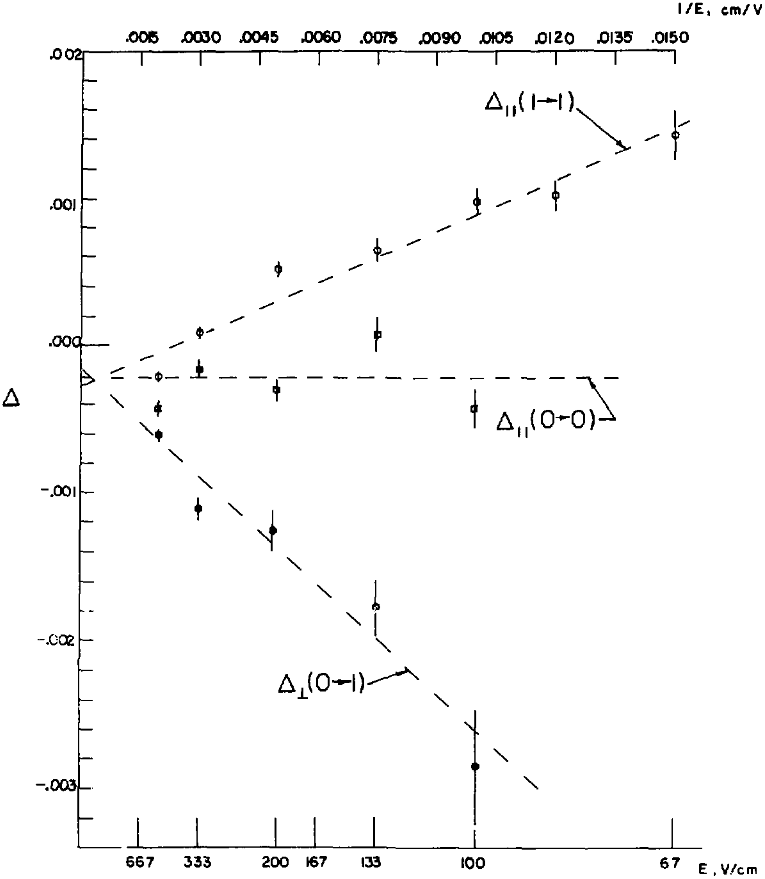

XBL 767-8831

Fig. II.4

$$\langle \psi_f | H_p | \psi_i \rangle = - \frac{G}{2\sqrt{2}} Q_W \bar{u}'_e \gamma_\lambda \gamma_5 u_e \bar{\psi}'_N \gamma^\lambda \psi_N$$

$$= - \frac{G}{2\sqrt{2}} Q_W \int \psi^*_f(\vec{r}) \, \gamma_5 \psi_i(\vec{r}) \, \rho_N(r) \, d^3r \qquad \text{(II-17)}$$

where ρ_N is the (spherically symmetric) nuclear density function. In Nueffer's calculations, the integral was found to be insensitive to the exact form of a $\rho_N(r)$ (Neuffer 1977a) even for a point nucleus. The answer is

$$\mathcal{E}_p = i(1.9 \times 10^{-10}) \frac{|e|\hbar}{2m_e c} Q_W \quad .$$

Using the current world average for $\sin^2\theta_W = 0.23$,

$$Q_W = (1 - 4 \sin^2\theta_W) Z - N \approx - 118 \quad .$$

Table II-4 lists the electric dipole amplitudes for the $6P_{1/2} \to 7P_{1/2}$ transitions.

F. Selective Excitation to the 8S State

The polarization of the $7P_{1/2}$ state can be efficiently analyzed by optical pumping to the 8S state with circularly polarized photons traveling along the quantization axis. We denote the eight Zeeman levels of the $7P_{1/2}$ and $8S_{1/2}$ states as shown in Fig. II.5. Then the rate equations are

Table II-4. Parity nonconserving E1 amplitudes $6P_{1/2} \rightarrow 7P_{1/2}$ for $\vec{E} = E\hat{y}$; $\hat{\epsilon} = \cos\theta\hat{y} + e^{i\phi}\sin\theta\hat{z}$.

	$6P_{1/2}(0,0)$	(1, -1)	(1,0)	(1,1)
$7P_{1/2}$				
(0,0)	0	$-i\mathcal{E}_p \cos\theta$	$-i\mathcal{E}_p \sin\theta e^{i\phi}$	$-i\mathcal{E}_p \cos\theta$
(1,-1)	$+\frac{i\mathcal{E}_p}{\sqrt{2}} \cos\theta$	$-\frac{i\mathcal{E}_p}{\sqrt{2}} \sin\theta e^{i\phi}$	$+i\mathcal{E}_p \cos\theta$	0
(1,0)	$-i\mathcal{E}_p \sin\theta e^{i\phi}$	$-i\mathcal{E}_p \cos\theta$	0	$+i\mathcal{E}_p \cos\theta$
(1,1)	$\frac{i\mathcal{E}_p}{\sqrt{2}} \cos\theta$	0	$-i\mathcal{E}_p \cos\theta$	$-i\mathcal{E}_p \sin\theta e^{i\phi}$

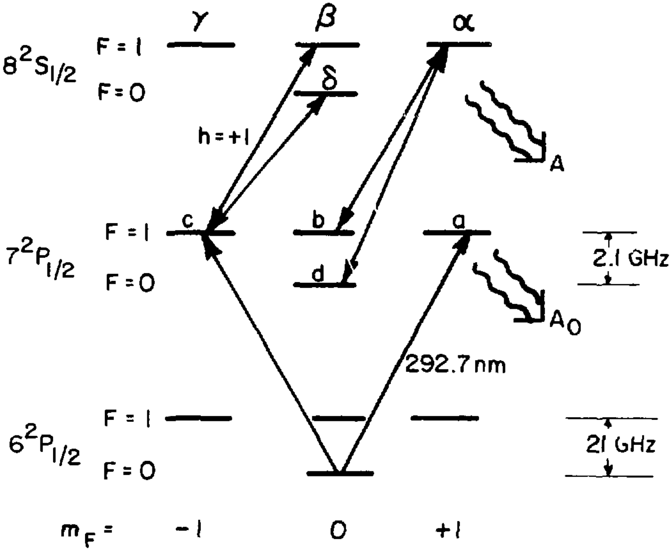

XBL 807-5572

Figure II.5 $7P_{1/2} \rightarrow 8S$ selective excitation. Circularly polarized infrared photons selectively excite $7P_{1/2}$ $m_F = -1$ or $m_F = +1$ atoms to the 8S state. A and A_0 are spontaneous decay rates.

$$\dot{a} = S_{11} - A_0 a + L(\beta + \delta - 2a) + \frac{1}{3} A_{87}(\alpha + \beta + \delta) \qquad \text{(II-18a)}$$

$$\dot{b} = S \;\; - \;\; A_0 b + L(\gamma - b) + R(\alpha - b) + \frac{1}{3} A_{87}(\alpha + \gamma + \delta) \qquad \text{(II-18b)}$$

$$\dot{c} = S_{1-1} - A_0 c + R(\beta + \delta - 2c) + \frac{1}{3} A_{87}(\beta + \gamma + \delta) \qquad \text{(II-18c)}$$

$$\dot{d} = S_{00} - A_0 d + R(\alpha - d) + L(\gamma - d) + \frac{1}{3} A_{87}(\alpha + \beta + \gamma) \qquad \text{(II-18d)}$$

$$\dot{\alpha} = -A\alpha + R(b + d - 2\alpha) + \frac{1}{4} A_1(\alpha + \beta + \gamma + \delta) \qquad \text{(II-18e)}$$

$$\dot{\beta} = -A\beta + R(c - \beta) + L(a - \beta) + \frac{1}{4} A_1 \; (\alpha + \beta + \gamma + \delta) \qquad \text{(II-18f)}$$

$$\dot{\gamma} = -A\gamma + L(b + d - 2\gamma) + \frac{1}{4} A_1(\alpha + \beta + \gamma + \delta) \qquad \text{(II-18g)}$$

$$\dot{\delta} = -A\delta + R(c - \delta) + L(a - \delta) + \frac{1}{4} A_1(\alpha + \beta + \gamma + \delta) \qquad \text{(II-18h)}$$

where

A_0 = $7P_{1/2}$ spontaneous decay rate = 2.14×10^7 sec^{-1}

A = $8S_{1/2}$ spontaneous decay rate = 4.36×10^7 sec^{-1}

A_{87} = $8S_{1/2} \rightarrow 7P_{1/2}$ spontaneous transition rate = 0.357×10^7 sec^{-1}

A_1 = $8S_{1/2} \rightarrow 6P_{1/2}$ spontaneous transition rate = 1.8×10^7 sec^{-1}

R = induced absorption rate for right circularly polarized light

L = induced absorption rate for left circularly polarized light

S_{11} = induced absorption rate for 6P, F = 0 → 7P, $(F, m_F) = (1,1)$ (the "0-1" transition)

S_{00} = induced absorption rate for 6P, F = 0 → 7P, F = 0 (the "0-0" transition)

S_{1-1} = induced absorption rate for 6P, F = 0 → 7P, (F, m_F) = (1,-1)("0-1" transition).

These equations assume no coherence between substates a, b, c, d of the 7P state, or between the L and the R photons. Both of these assumptions are, strictly speaking, false; but it can be shown that the results are unchanged. For example, consider the (0-1) transitions: The 6P → 7P → 8S transitions must be considered as a two photon coherent process:

$$
\begin{aligned}
|a_{6P\rightarrow 8S}|^2 = {} & \Big|\langle 8S(1,0)|\hat{\epsilon}_R\cdot\vec{r}\,|7P(1,-1)\rangle\langle 7P(1,-1)|\hat{\epsilon}_{uv}\cdot\vec{r}\,|6P(0,0)\rangle \\
& + \langle 8S(1,0)|\hat{\epsilon}_L\cdot\vec{r}\,|7P(1,1)\rangle\langle 7P(1,1)|\hat{\epsilon}_{uv}\cdot\vec{r}\,|6P(0,0)\rangle\Big|^2 \\
& + \Big|\langle 8S(0,0)|\hat{\epsilon}_R\cdot\vec{r}\,|7P(1,-1)\rangle\langle 7P(1,-1)|\hat{\epsilon}_{uv}\cdot\vec{r}\,|6P(0,0)\rangle \\
& + \langle 8S(0,0)|\epsilon_L\cdot\vec{r}\,|7P(1,+1)\rangle\langle 7P(1,1)|\hat{\epsilon}_{uv}\cdot\vec{r}\,|6P(0,0)\rangle\Big|^2 \quad .
\end{aligned}
$$

From symmetry considerations, $\langle 00|\hat{\epsilon}_R\cdot\vec{r}\,|1,1\rangle = \langle 10|\hat{\epsilon}_R\cdot\vec{r}\,|1,1\rangle = \langle 10|\hat{\epsilon}_L\cdot\vec{r}\,|1,-1\rangle = -\langle 00|\hat{\epsilon}_L\cdot\vec{r}\,|1,-1\rangle$. After making these substitutions, the cross terms in Eq. (II-13) vanish, so that the result is as if the state were incoherent. The (0-0) transitions follow similarly.

To solve these rate equations, we will assume statistical equilibrium. This is valid because the laser pulses, which are 500 ns long, are much longer than the time it takes to establish equilibrium, which is determined by the 7P and 8S lifetimes of ~50 ns. The equations also assume that the $8S_{1/2} \rightarrow 6P_{1/2}$ transition is resonantly trapped. This is true if the mean free path of a 258.1 nm $8S \rightarrow 6P_{1/2}$ photon is much smaller than the other dimensions of importance, in this case the region of laser beam overlap of ~(0.3 cm)^3. The mean free path is given by $\lambda = n_\gamma c/B_1 \rho n$ where B_1 is the Einstein B coefficient, ρ the energy density of 258.1 nm light, and n the density of Tl in the cell. n_γ is the density of 258.1 photons. Therefore

$$\lambda = n_\lambda \times \frac{8\pi h\nu^3}{c^3 A_1} \times \frac{\Delta\nu_D}{h\nu n_\gamma} \times \frac{1}{n} \times c = \frac{8\pi\nu^2 \Delta\nu_D}{c^2 n A_1} \quad ,$$

and for $\Delta\nu_D = 10^9$ Hz, $n = 10^{15}$ cm^{-3}, and $A_1 = 1.8 \times 10^7$ sec^{-1}, $\lambda = 21\ \mu$, so the resonance trapping assumption is valid. Resonance trapping introduces a term $1/4\ B_1 \rho n$ to each of Eqs. (II-5) through (II-8); but if the trapping is complete, this is just equal to one-fourth the rate at which 258.1 photons are produced or $1/4\ A_1(\alpha + \beta + \gamma + \delta)$. This simplification allows the equations to be solved more easily.

We want to calculate the signal size which we should expect in the 323 nm channel, as compared to the 535 nm signal which would be seen if all the 7P atoms were allowed to decay via $7S_{1/2}$. We also need to know the polarization analyzing power of the pumping method at the frequencies where data are taken. The total signal size is given by the quantity $A(\alpha + \beta + \gamma + \delta)$. This can be extracted from Eqs. (II-18a-h). (See, for example, Conti (1979); also Appendix A.) This is a function of the 2.18 μ intensity and quality of circular polarization, the uv laser intensity and tuning. The numbers which go into this calculation are as follows: The Doppler width, which can be calculated, is 1.5 GHz; the total inhomogeneous linewidth is measured to be 1.6 GHz; the isotopic abundance is taken to be 70 percent T^{205} 30 percent T^{203} (CRC Handbook); the isotope shift in this transition is 1.27 GHz (Flusberg et al., 1976; Drell et al., 1979); the ratio of strengths of the 0-1 and 0-0 transitions is measured to be $\beta^2/\alpha^2 = 0.7$. Figure II.6 is a plot of signal vs the induced absorption coefficient for the 7P → 8S pumping. The vertical scale is normalized so that the 7P population, when tuned to 0-1 line, is one. At absorption rates of 3×10^8 sec^{-1}, roughly the regime where we work, about 6 percent of the 7P atoms decay via 323 light. When we tune to the 0-0 line, the number of 7P atoms increases by the ratio $\alpha^2/\beta^2 = 1.44$, but the 8S pumping of the 7P(F = 0) atoms with circularly polarized light is more efficient, so that the signal size is increased by a factor of 1.8 or so. The figure also shows that the two regions have different signal sizes due to the different quality of circular polarization in each region. This will be discussed in Section E.

The second feature we wish to extract from the rate equations is the analyzing power, defined as the signal asymmetry $(S_R - S_L)/(S_R + S_L)$ when the infrared polarization is reversed, divided by the polarization of the 7P state $(S_{11} - S_{1-1})/(S_{11} + S_{1-1} + S_{00})$. Here the quality of infrared polarization becomes more critical. Figure II.7 shows the

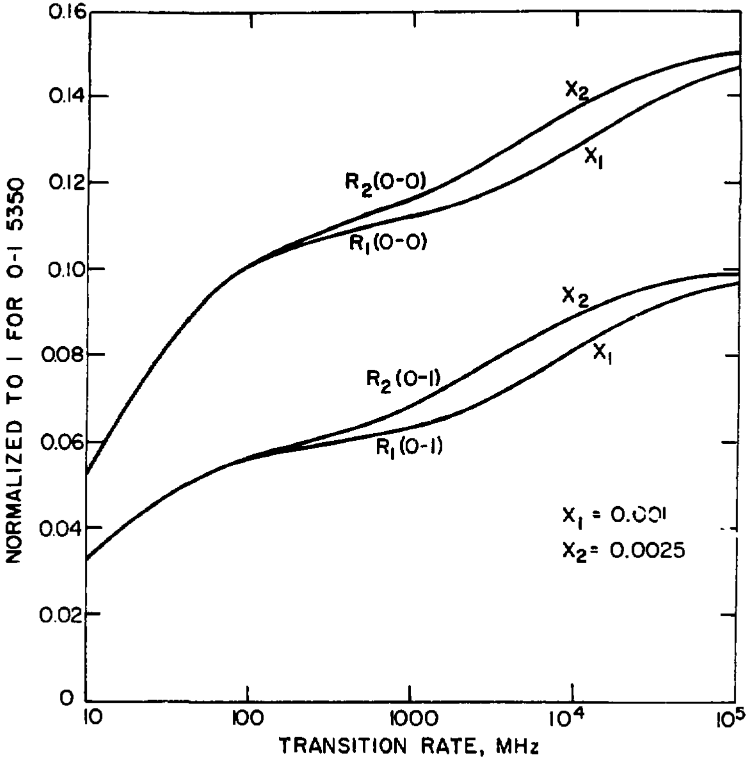

XBL 807-5573

Figure II.6 *323 nm decay fraction vs. $7P_{1/2}$-8S induced absorption* rate. The top two curves are for the (0→0) transition in each region. The regions differ because the quality of 2.18μ circular polarization is not equal between them. x is the measured fraction of incorrect helicity photons which pollute the laser beams. The bottom two lines are for the (0→1) transition.

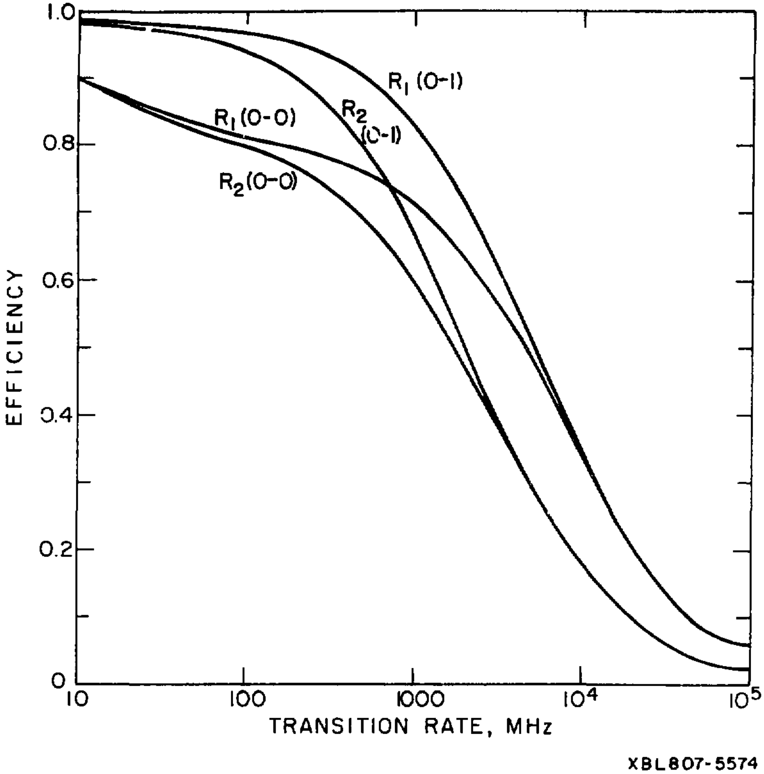

Figure II.7 Analyzing power vs. $7P_{\frac{1}{2}}$-8S induced absorption rate.

analyzing power as a function of the ir absorption rate. At 2.0×10^{8} sec^{-1}, the most striking feature is the 15 percent reduction of analyzing power when the laser is tuned to the 0-0 line. The effects of different polarizations in region 1 and 2 will be discussed later.

G. Experimental Asymmetry

From Tables II-1, II-3, and II-4, we extract the F = 0 → F = 1 amplitudes for laser polarization $\hat{\varepsilon}_{\pm}$ with the experimental geometry shown in Fig. II.2:

$$A(0\text{-}1) = \begin{bmatrix} \mp \frac{E\beta}{2} \pm \frac{M}{2} - \frac{i\mathcal{E}_P}{2} \\ \frac{M}{\sqrt{2}} \mp \frac{i\mathcal{E}_P}{\sqrt{2}} \\ \pm \frac{E\beta}{2} \pm \frac{M}{2} - \frac{i\mathcal{E}_P}{2} \end{bmatrix} \qquad \text{(II-20)}$$

The polarization is

$$P_{0-1} = -\frac{2M}{\beta E} \pm \frac{2i\mathcal{E}_P}{\beta E} = -\frac{2M}{\beta E}\left(1 \pm \frac{\delta}{2}\right) \quad . \qquad \text{(II-21)}$$

As the figure shows, there are two interaction regions. When R1 has h = -1 light, R2 has h = +1 light and vice versa. The fluorescent signals S1 and S2 therefore have an asymmetry: $\Delta = (S1 - S2)/(S1 + S2) = dP_{0-1}$, where d is a dilution factor ~ 1. By reversing the ir polarization or E, Δ will reverse sign. If the uv polarization is reversed, Δ will change its <u>size</u> by an amount δ. By chopping rapidly between the eight configurations (2uv x 2ir x 2E), we accumulate statistics for $2\mathcal{M}/\beta$ and $2i\mathcal{E}_p/\beta$ simultaneously.

H. Preliminary Experiments

In a previous paper (Conti et al., 1979) we reported preliminary results of this work. Twenty-one million laser pulses of data were taken, half on the 0-1 transition and half on the 0-0 transition as a null experiment. The results are shown in Fig. II.8.

In our efforts since then to reduce the uncertainty to 25 percent, we have made enormous progress in understanding and eliminating systematic errors. We have had difficulties, including 6 months lost when we tried to use the $7P_{1/2} \to 11S_{1/2}$ transition at 813.2 nm to analyze the polarization. It turned out that the backgrounds in the detection channel at 258 nm were so large, and the pumping efficiency so small, that the 11S experiment had to be abandoned. We returned to the 8S experiment, and made many significant improvements. We now feel a 25 percent measurement is possible.

Figure II.8 Data of Conti et al (1979). Δ_p is normalized by rescaling the data by the fraction required to make the M1-Stark inference equal to 5.5×10^{-3}. UV+,-, and IR1,2, designate changes in the laser beams which reverse the sign of the effect in our apparatus. The data shown have been corrected as required to eliminate these sign changes.

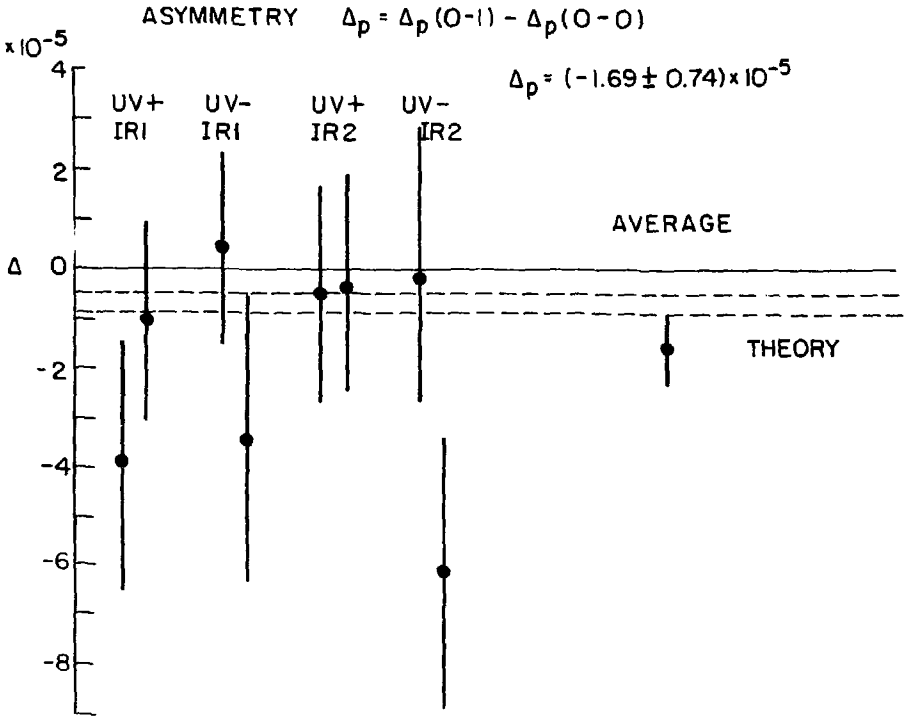

Fig. II.8

XBL 807-5575

CHAPTER III: APPARATUS

The experiment is shown in Fig. III.1(a). The laser which produces 293 nm light is in the foreground. The ir laser is on the right. Optical components are mounted on the steel surfaced wooden tables by means of magnetic bases. The two laser beams converge in the thallium cell which is buried within the vacuum can at the top left of the picture. Figure III.1(b) is a schematic diagram of the apparatus. In the rest of this chapter we will describe the components in detail.

A. Laser Discharge Circuit

The lasers used in this experiment are flashlamp pumped pulsed dye lasers. Both were designed in our laboratory by Steven Chu (Chu and Smith 1979) and built by the group. The two lasers are essentially identical. The basic discharge circuit is shown in Fig. III.2. The lamps (ILC #L-2339) are constantly kept in a conducting state by means of a 700 ma current-regulated dc simmer. This reduces both the inductance and the mechanical shock to the lamps caused by the expanding plasma sheath during discharge. The simmer is responsible for giving us outstanding lamp lifetimes, typically 2 x 10^7 shots (~10^8 joules) per lamp change. The main discharge circuit contains a capacitor (0.2 μF, 25 kV low inductance) and a thyratron (EEV 2506). In typical operation, 10 joules are discharged through the lamps on each pulse, and the repetition rate is 20 Hz. The discharge time is approximately 1.2 μs. Quick recharging of the capacitor is performed by a large resonant tank circuit, consisting of a 7 5 μf capacitor and a 25 Hy inductor. This is

Figure III.1 (a) View of the laboratory. Laser L1 is in the foreground; L2 is on the right. The frequency monitor cell is out of view to the left, behind the main vacuum can. Racks on the far wall hold the oven power supplies, experimental control equipment, detection electronics, and an LSI 11/2 computer.

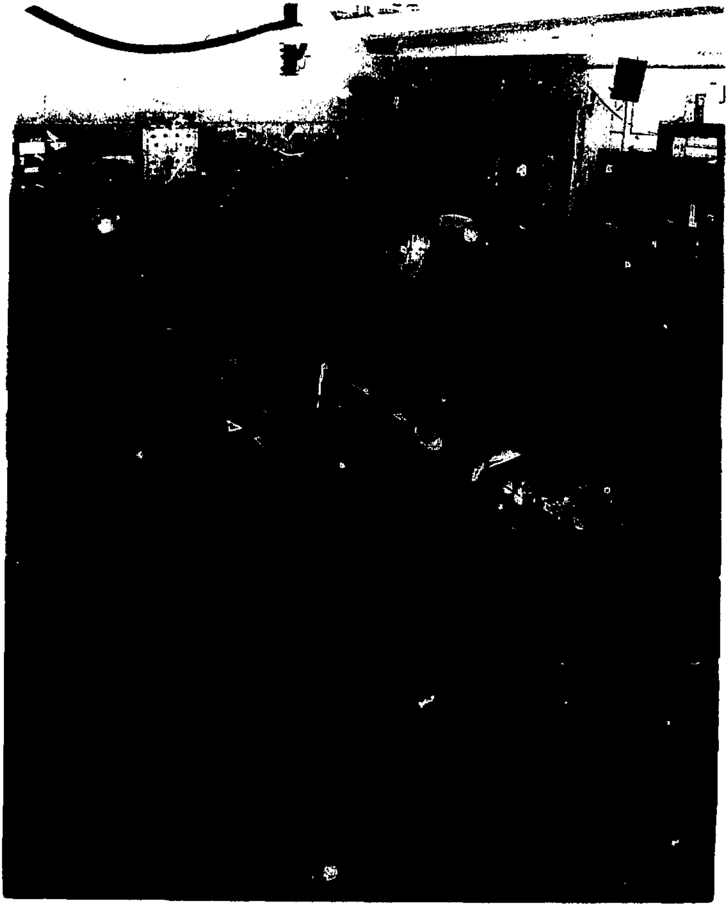

CBB 807-8792

Fig. III-1a

Figure III.1 (b) Block diagram of the apparatus. L1: 6P → 7P laser. ADA: frequency doubler. GP: Glan-Air prism polarizer. P.C.: Pockels cell. E: electric field. M: back surfaced uv dielectric reflector. L: f/1 quartz lens. λ/4: crystalline quartz quarter wave plate. 1,2: interaction regions. F: optical filter. PMT: photomultiplier tube. MC: frequency monitor cell. L2: 7P → 8S laser. OPO: optical parametric oscillator. BS: silicon beamsplitter. LP: Polaroid infrared linear polarizer. CP: quartz quarter wave plate for 2.18μ.

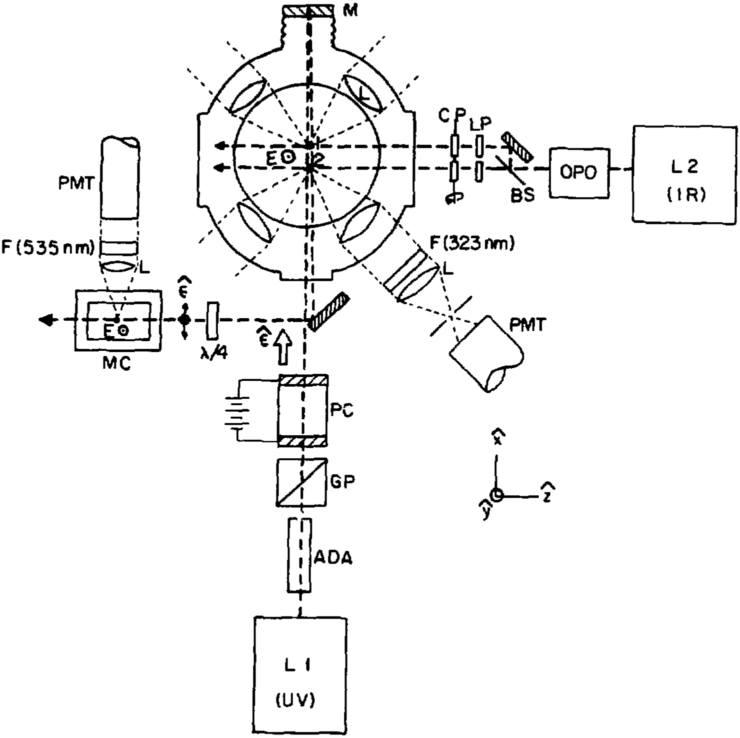

XBL 808-5751

Fig. III-1b

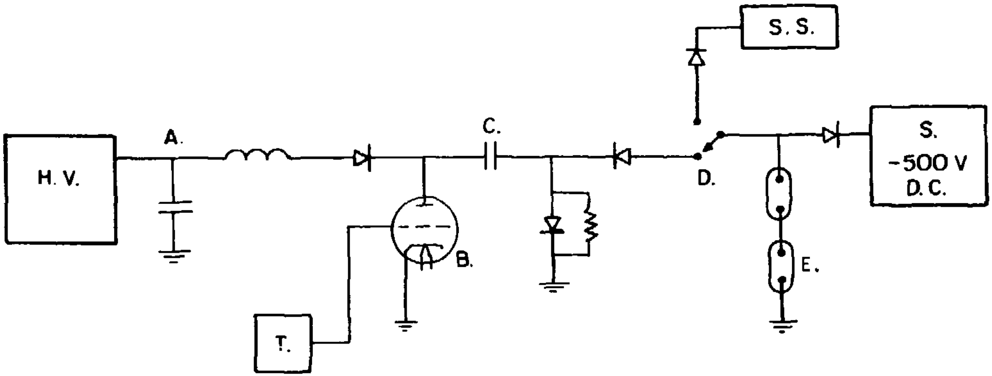

XBL 807-5576

Figure III.2 Laser discharge circuit. H.V.: High voltage power supply. A: Resonant charging circuit. B: Thyratron. T: Thyratron trigger circuit. C: Main discharge capacitor. D: High voltage vacuum relay. E: Flashlamps. S: Simmer power supply. S.S.: Simmer start circuit.

supplied with 6 kV at 50 ma from a dc power supply. The resonant frequency of the tank circuit has been set to slightly less than the repetition rate. As a consequence, the voltage on the main discharge capacitor is a decreasing function of pulse rate, and so is the laser output energy.

When the laser is fired, a logic pulse turns on an SCR, which triggers a pulse transformer and which drives the thyratron grid positive. The thyratron becomes conducting, which causes the capacitor to discharge through the lamps. The total time jitter in the system is about 5 ns, or 1 percent of the pulse width. The great virtue in the design is its simplicity. The two lasers together have been fired over half a billion times. So far we have only had to replace two resonant charger inductors, one thyratron, one pulse transformer, and a few diodes.

B. Laser Cavity

The flashlamps are enclosed in a double elliptical cavity (Fig. III.3). The geometry is similar to a Zeiss laser head #FL3B (Carl Zeiss, Inc.), but it is home-made out of Pyrex (Chu 1978). The cavity is formed by deforming a softened Pyrex tube (28 mm) in a heated carbon mold. The double ellipse is then trimmed and the edges fire polished. After annealing, the outside is coated with a pinhole-free film of aluminum, and overcoated by Krylon plastic. De-ionized water floods the cavity during laser operation, flowing in near the lamp supports, and out through a tubulation in the middle. The main function of the water is to cool the lamps, but it also acts as an index match to the Pyrex

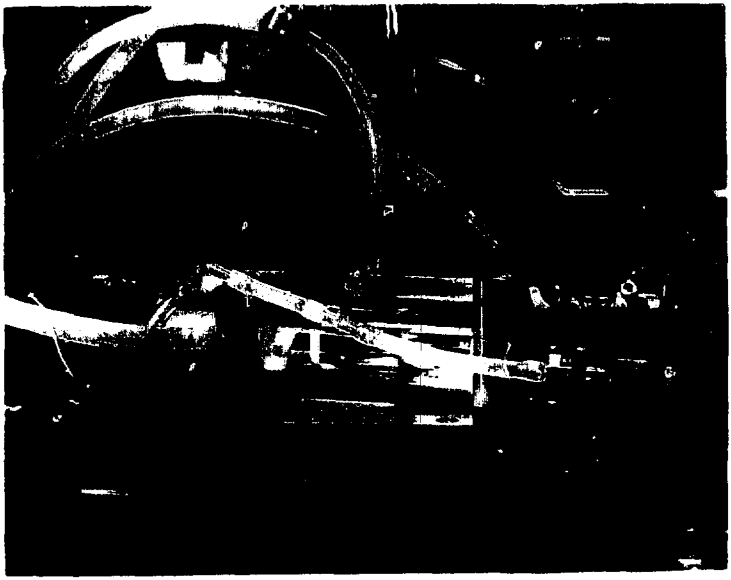

CBB 784-4090

Figure III.3 (a) Pyrex laser head in place in laser L1.

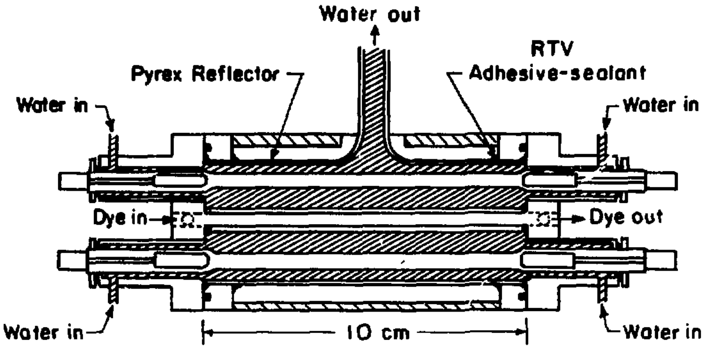

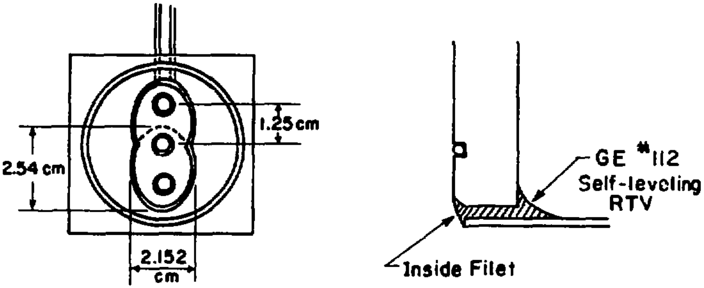

XBL 788-5548

Figure III.3 (b) Cross sectional diagram of the Pyrex double ellipse, showing lamp placement and RTV water seal.

inner surface, eliminating ripple irregularities. We have found that the back surface aluminum mirror is about twice as efficient as the Zeiss polished aluminum cavity. In addition it does not degrade significantly with time, since the reflective surface is not in direct contact with the water. There is also qualitative evidence that the pyrex improves dye lifetime, since the uv radiation which breaks down the dye molecules is not transmitted through the Pyrex to the reflector, but is down-converted to less harmful wavelengths.

Ellipse failure modes have so far always been cracks that appear near the ends of the lamps due to uneven heating. This could be solved by increasing the dimensions of the ellipse slightly. However, it is also strongly dependent on the individual ellipse. Bad ellipses last only ~2×10^7 shots. One particularly good one has lasted at least 10^8 shots.

C. Dye

The dye flows through a pyrex cuvette with a 4 mm bore at the common focus of the double ellipse. The inner walls of the curvette are ground to inhibit laser modes due to low angle scattering from the walls ("whisper" oscillations). Cuvette and lamps are held in place by O-ring seals in stainless steel endplates.

The dye flow rate must be fast enough so that the dye in the cuvette is completely replaced between laser shots, or else the laser performance suffers dramatically. Also, the dye and cooling water must enter the cavity at the same temperature (within 0.5°C) or else thermal distortions will seriously affect the shot-to-shot stability and bandwidth. To satisfy these requirements we have adopted the dye flow system shown in Fig. III.4. The system components are made entirely of teflon, polyethylene and stainless steel to avoid contamination. The heart of the system is a 60 psi gear pump (Micropump 114-64-316). The dye flows through a 5μ teflon filter (Millipore 142 mm) and then through a heat exchanger where cooling water and dye come to within 0.3°C of each other. Immediately after leaving the heat exchanger, the water and dye enter the laser head. Then they return to separate 20-liter glass reservoirs. With the exception of periodic replacement of drive gears in the pump, this system has proven highly reliable over thousands of hours of almost continuous use.

The dye is Rhodamine 6G (New England Nuclear, Pilot 559, Lot NEN 4-27). The quality of the dye varies significantly from lot to lot; for instance, Lot GG IV-20 had about 30 percent shorter lifetime than the present one. The solution used is 7×10^{-5} M in a 2:1 mixture of distilled water and reagent grade methanol. Although the wavelength of our laser (595 nm) is closer to peak efficiency for R6G dissolved in pure ethanol (and as much as we would prefer to use ethanol simply because the fumes are nontoxic), the water/methanol mixture has a higher heat capacity and smaller dn/dT where n is the refractive index. Consequently, the laser bandwidth and stability requirements dictate using methanol/water.

Figure III.4 Dye and cooling water flow system. The reservoirs are 20 liter glass bottles. P: pump. F: teflon disk filters. H: heat exchanger. L1, L2: dye lasers. D: deionization column.

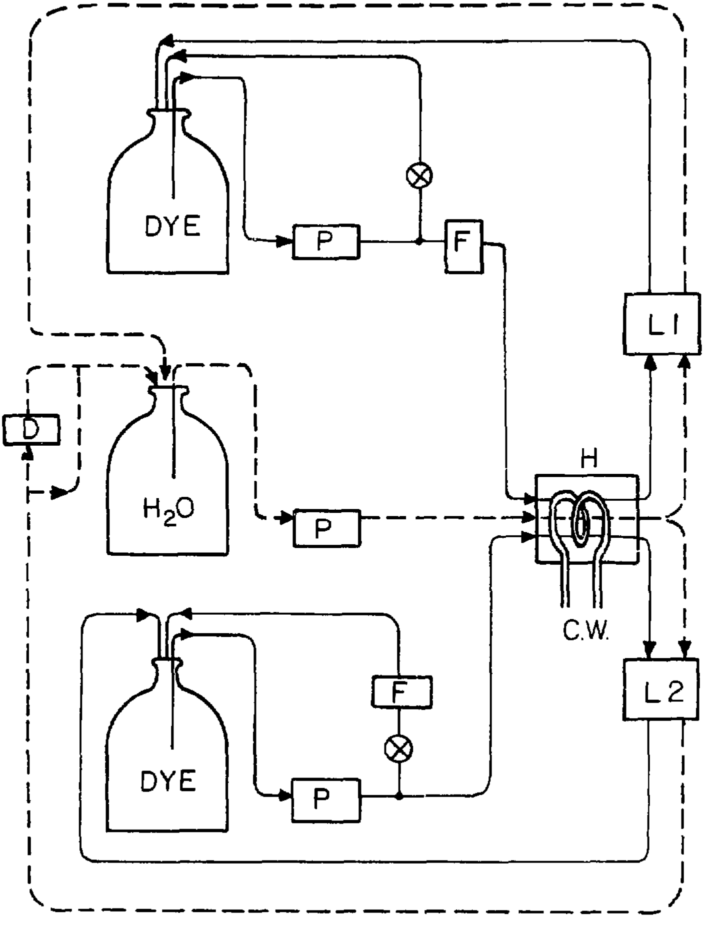

XBL807-5577

Fig. III.4

Dye lifetime is affected by lot, temperature, and system contamination. Old dye has a slightly greenish appearance compared to the bright orange-pink of a freshly mixed solution. A small amount of dye seems to be removed from solution by the teflon filters, but this does not account for the color change; for if more dye concentrate is added to an old solution it will not regain its original appearance or performance. We suspect that chemical decomposition of the dye is occurring, probably assisted by uv flashlamp light. To retard this process, the solution is purged of dissolved oxygen by bubbling dry nitrogen through it at all times. Our dye lifetime averages 1 million lamp joules/liter of dye.

D. Optical Cavities

The optical cavities in the two lasers are not the same. The laser which pumps the $6P_{1/2} \rightarrow 7P_{1/2}$ 293 nm transition (L1) has its dye cavity tilted horizontally at Brewster's angle. The purpose of this is to reduce the window reflection losses, and to insure that the output polarization is horizontal. It has the unfortunate side effect of introducing a noticeable astigmatism into the beam. The laser which pumps the infrared optical parametric oscillator (L2) was designed with normal incidence laser head windows which were antireflection coated. An intracavity Brewster plate defines the polarization. This has not proven as satisfactory, since lasing from the cuvette windows is observed as a dim laser spot slightly displaced from the main laser beam.

The optics for L1 have been chosen to optimize the narrow bandwidth (see Fig. III.5). The back reflector is a 6 meter spherical high reflector, and the output coupler is a 50 percent reflecting flat mirror with an antireflection coat on the back. The cavity is 1 m long. The intracavity optics consist of three tuning elements: an interference filter (Lambda Physik), a thin etalon (.15 mm thick, 63 percent reflective, from Lambda Physik), and a thick etalon (1 cm thick, 20 percent reflective, made by Coherent Radiation for use in the CR590 dye laser). The thick etalon is held in a pivot mount so that it can be tilted automatically by a piezoelectric pusher (Burleigh).

The laser pulse is 0.5 μs fwhm, and approximately .03 cm^{-1} in bandwidth. It is multimode both transverse and longitudinal, and has a divergence of about 2 x 10^{-3} radians.

Laser L2 has an optical cavity that has been optimized for pumping the optical parametric oscillator. It consists of a flat high-reflector, a 40 percent reflecting output coupler, a 4 nm interference filter (Lambda Physik), and a single thin etalon. The bandwidth of this laser depends on the finesse of the etalon, and has been empirically set to produce the most stable OPO output. We use a .15 mm etalon (Lambda Physik) with a reflectivity at 585 nm (the operating wavelength) of only 35-40 percent. The bandwidth (analyzed with a direct view etalon) is .5 cm^{-1}. The length of the cavity is 1 m, which is a compromise between ir frequency stability and laser alignment stability. This will be discussed in the next section.

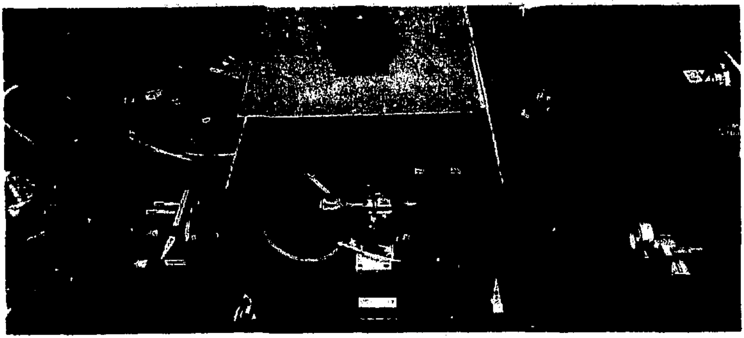

XBB 807-8797

Figure III.5 Optical cavity of laser L1. The components, from left to right, are a 6 m spherical back reflector; thick etalon with piezoelectric tilt mount; thin etalon; interference filter; laser head, output coupler.

E. Optical Parametric Oscillator (OPO)

The infrared laser light is produced by a Chromatix CMX-4/IR OPO. This is a .4x.4x4.0 cm crystal of $LiNbO_3$ placed in a confocal cavity (see Figs. III.6 and III.7). The crystal is maintained in a low gradient oven at a temperature of 350°C. The OPO works by converting a visible photon γ_P into two lower frequency photons γ_S and γ_I subject to the energy conservation and phase matching conditions $\omega_P = \omega_S+\omega_I$ and $\vec{k}_P = \vec{k}_S+\vec{k}_I$, inside the nonlinear crystal. The theory of optical parametric amplification is discussed by Yariv (1975) and Harris (1969). An input "signal" wave (ω_S) interacts via the crystal with an input "pump" wave (ω_P) to produce an "idler" wave ω_I. In the Chromatix OPO, the confocal cavity is designed to resonate at $\lambda_S = 2.18\mu$ by means of dielectric V-coatings on the mirrors. ω_P is supplied by our pump laser, and focused to match the confocal beam parameters of ω_S with an extracavity lens. λ_I is about 800 nm, and is not used. The forward mirror coating is partially transmitting, so that some signal photons escape. The signal frequency is changed by changing the crystal temperature which alters the phase matching condition.

In this mode of operation we must use signal photons to excite the 2.18μ $7P_{1/2} \rightarrow 8S$ transition. The high finesse of the OPO cavity means that the frequency distribution of signal photons looks like a comb, with high spikes spaced at intervals of 600 MHz. Unfortunately, the Doppler width for the transition is only 230 MHz. It is very difficult to keep the OPO on resonance because of this. We have

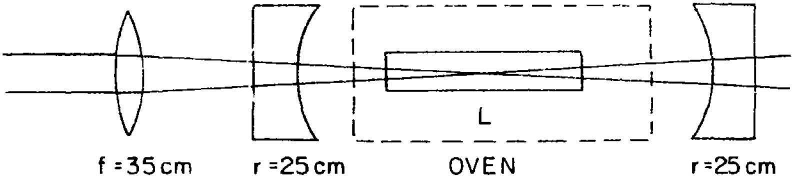

XBL 807-5578

Figure III.6 Chromatix CMX4/IR Optical Parametric Oscillator (OPO) cavity.

L: lithium niobate crystal.

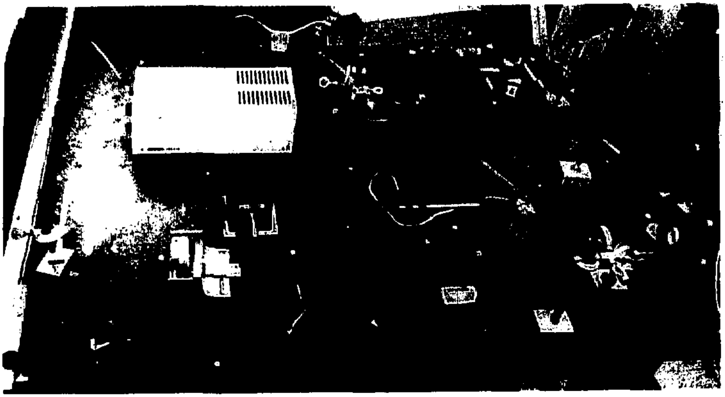

XBB 807-8794

Figure III.7 Infrared optical table, showing laser L2, the Chromatix OPO, and the ir optical path. Silicon wafer on a tilt mount at the upper right acts as a beam splitter for the two interaction regions.

modified the design as follows: The mirrors now reflect at 800 nm and the crystal has been antireflection coated at 800 nm. Now the idler photons are $\lambda_I = 2.18\mu$. Their wavelength is changed by tilting the thin etalon on L2. The longitudinal mode structure of the ir beam is the superposition of the OPO cavity modes and L2 cavity modes, and the comb spacing is about 150 MHz. This still produces a 10-20 percent pulse-to-pulse jitter in the 323 nm signal from the thallium cell, since the mode spacing and Doppler width are comparable. As a test, we lengthened the L2 cavity to 277 cm. This improved the stability of the 323 nm signal further. However, this makes L2 difficult to tune and subject to large drifts due to room temperature fluctuations, so we have returned the length to 1 meter.

The 2.18μ laser beam enters region 1 and region 2 separately, along the z-axis. This is accomplished by splitting the beam with a thin wafer of polished Si (an integrated circuit substrate). The transmission through both surfaces is 50 percent. The perpendicularity to the uv laser beam, although not critical, has been checked to within about 1°. The ir beams pass through individually adjustable linear polarizers (Polaroid HR plastic) and crystalline quartz quarter wave plates (Virgo Optics). The quarter wave plates can be flipped about the horizontal axis to reverse the helicity of the beams (Fig. III.13).

The output energy of the OPO is 0.25 mj per pulse with a bandwidth of 2 cm^{-1} (Chromatix specification). This corresponds to a photon conversion efficiency of 15 percent, and a peak spectral intensity of 5 watts/GHz. Only one watt/GHz is needed to saturate the transition, so an attenuator is placed in the beam.

F. Doubling Crystal

The light from L1 is focused with an f = 62 cm lens into a .5x.5x5.0 cm cystal of $NH_4H_2AsO_4$(ADA). The ADA is a second harmonic generator (Yariv 1975). It is 90° phase matched, and temperature stabilized to maintain the phase matching condition. An aluminum oven surrounds it which is dessicated and sealed against moisture (see Fig. III.8). The oven temperature of 25°C is maintained to within .01°C by a thermoelectric heater/cooler, and a home-built temperature controller. We have measured the laser beam waist size directly, and we estimate peak intensities of 10-20 MW/cm^2 in the crystal. With an input to the crystal of 8.5 mj in a .5 µs pulse, the ADA generates .95 - 1 mj of frequency-doubled light. The temperature for peak doubling efficiency differs by about .01°C for the two hyperfine transitions F = 0 → F' = 0,1 ($\Delta\nu$ = 2.13 GHz), and the phase matching condition is broad enough that no retuning of the crystal temperature is necessary. To tune to the F = 1 → F' = 0,1 transitions, however, the crystal must be warmed by .1°C.

G. UV Circular Polarization

The 293 nm light is polarized vertically, orthogonal to the 585 nm pump beam. We use a Glan-Air calcite prism to separate the beams and define the uv linear polarization before entering the circular polarizer.

XBB 807-8795

Figure III.8 Ultraviolet optical table. The light passes through: focusing lens; ADA doubling crystal oven; two lens quartz telescope; Glan Air prism (rejects fundamental wavelength); Pockels cell, aperture and final quartz lens. Rack behind holds the ADA temperature controller and L1 power supplies. The upright cylinder is the vacuum enclosure for the frequency monitor cell.

Two completely different methods have been used to circularly polarize the uv laser beam. As will be shown in Section F of Chapter IV, the quality of polarization is critical. If we designate - (+) helicity photons in the experiment as having polarization $\hat{R}$ ($\hat{L}$), then we may parametrize $\hat{R}$ and $\hat{L}$ in terms of perfect circular polarization $\hat{\epsilon}_R$ and $\hat{\epsilon}_L$ as follows:

$$\hat{R} = \hat{\epsilon}_R(1 - \eta^2)^{1/2} + \eta e^{i\delta}\hat{\epsilon}_L \;;\quad \hat{L} = \hat{\epsilon}_L(1 - \eta'^2)^{1/2} + \eta' e^{i\delta'}\hat{\epsilon}_R \qquad \text{(III-1)}$$

We will show later that false parity effects can occur, which are proportional to $(\eta \cos \delta - \eta' \cos \delta')$, or $(\eta \sin \delta + \eta' \sin \delta')$.

The old method for creating circular polarization used a precision crystalline quartz quarter wave plate. The plate was multiple order, retarding the component of polarization along the optic axis by approximately 7 1/4 waves. It was held in a mount which was attached to the shaft of a motor along the $\hat{z}$ axis (horizontal, normal to uv beam). As the motor shaft turned, the quarter wave plate flipped between positions of right and left circular polarization. A marker attached to the motor triggered the laser.

To align this quarter wave plate, we placed a mirror directly behind it, and reflected the beam beak through the quartz and the Glan-Air prism. This light had been retarded by 1/2 wave (two passes through the quartz), so it was almost completely extinguished by the polarizer. The wave plate was adjusted to minimize the polarizer transmission. Typical extinction ratios of 5×10^{-3} were obtained at normal incidence. By having the laser fire when the wave plate was not exactly at normal incidence, we were able to achieve extinction ratios of $0.5 - 1 \times 10^{-4}$. This corresponds to an intensity ratio for circularly polarized light of $I(R)/I(L) \approx 2 \times 10^{-5}$, an extraordinary figure, much better than required to do the experiment. In spite of this, the method has several drawbacks:

1. Birefringence in the vacuum can window and cell window degrade the polarization in the interaction region, and there is no satisfactory way to correct it.

2. Crystalline quartz is optically active along the optic axis. When the plate is tilted, this causes slight depolarization effects which cancel out in the half wave alignment procedure, but not in the actual experiment.

3. Mechanically triggering the laser causes a small timing jitter which is correlated with the circular polarization. This couples to the lasers by causing an intensity jitter due to the resonant charger and a frequency jitter (Section D, Chapter IV). These introduce systematic errors which are difficult to compensate, and eventually forced us to change the way we polarize the light.

The rotating quarter wave plate was replaced by a Pockels cell (INRAD). This is a 2 cm crystal of KD*P (KD_2PO_4) aligned with its principal axis along the beam direction. Ring electrodes attached to the ends produce a longitudinal electric field which causes phase retardation via the Pockels effect. The KD*P has been antireflection coated (UVIRA, Mountain View, CA) and is kept in a sealed dessicated environment. ±$\lambda/4$ retardation is produced by applying ±1000 V to the electrodes. The voltage is pulsed to eliminate the effects of long term relaxation in the retardation which occurs with a dc electric field. To avoid very strong electromechanical resonances in the crystal, the pulse has a slow (100 μs) rise time. It is produced by a high voltage pulse generator consisting of two series stacks of DTS-723 transistors, connected to individual plus and minus regulated power supplies.

The chief advantage of a Pockels cell is that the retardation can be adjusted electrically, rather than by moving the device. The disadvantage is that initial physical alignment is very difficult. The laser beam must be aligned within a few milliradians of the $\hat{z}$ axis, or else a large residual birefringence will occur. Since the electric field in the crystal is non-uniform, the beam must be small, and it must be collimated. We use a two lens telescope before the linear polarizer to produce a beam size of 0.08 cm, with the waist in the Pockels cell. We can consistently achieve ± half wave extinction ratios of 7×10^{-4}, measured by placing a second Glan-Air prism behind the KD*P as an analyzer, and applying 1/2 wave voltage (~ 2000 V). The alignment procedure begins with this step. Reducing the voltage to half the $\lambda/2$ values does not produce a $\lambda/4$ retardation because of second order nonlinear effects; so we use a fixed $\lambda/4$ plate in series with the Pockels cell to find the approximate $\lambda/4$ voltage.

The final alignment makes use of the Stark effect in thallium: Let $S_L(S_R)$ be the 323 nm fluorescent signal size for $\hat{L}$ ($\hat{R}$) polarization. Then define

$$\delta_{uv} = \frac{S_L - S_R}{S_L + S_R} \quad ,$$

where we have averaged over regions 1 and 2. Then, for the 0-1 line, it is easily shown that $\delta_{uv} = 2(\eta \cos \delta - \eta' \cos \delta')$ where $\eta(')$ and $\delta(')$ have been previously defined in Eq. (III-1). δ_{uv} can be made to be nearly zero by fine adjustment of the Pockels cell voltages.

H. Absolute Determination of UV Photon Helicity

The helicity of the uv photons determines the relative sign of Im $(\mathcal{E}_p)$ and M. We can measure it in two independent ways: optically, and using the 1-1 transition in thallium.

The optical method uses zero order uv quarter wave plates as circular polarization analyzers. The sense of polarization produced by these plates can be determined by the procedure in Fig. III.9 (a). A HeNe laser beam passes through two of the uv plates in series. This produces circularly polarized red light which can be analyzed with a Polaroid left circular polarizer. (Helicity +1 light is transmitted through the Polaroid filter.) Once the uv $\lambda/4$ plate orientation is known it can be used with a calcite linear polarizer to analyze the 293 nm photons which have passed through the Pockels cell in the experiment, as shown in Fig. III.9 (b).

Figure III.9 (a) Determining the sense of retardation of quartz zero order retardation plates (see text). P: linear polarizer. Q_1, Q_2: zero order crystalline quartz uv quarter wave plates. L: Polaroid left circular polarizer. D: detector or screem.

(b) Determining Pockels cell polarization. P_1, P_2: linear polarizers. P.C.: Pockels cell. Q: quarter wave plate from Fig. III.9(a). D: detector. ADA: frequency doubling crystal.

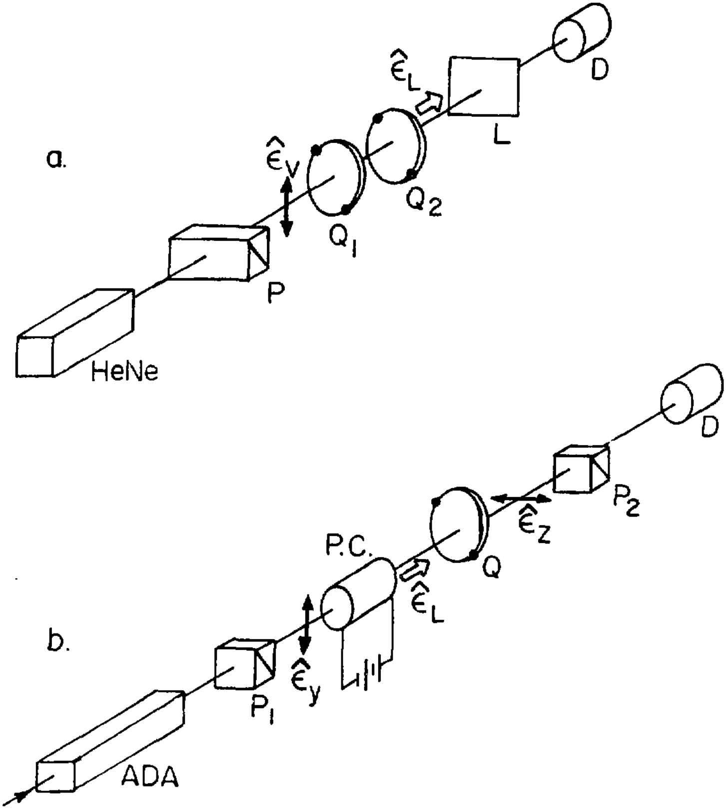

XBL 807-5579

Fig. III.9

We also take advantage of the interference between α and β Stark effect amplitudes in the 1-1 line. The $7P_{1/2}$ state which results from 1-1 absorption is polarized along $\hat{x}$ (see Section E, Chapter IV)

$$P_x^{1-1} = \pm \frac{4\alpha b}{3\alpha^2 + 2\beta^2} = \pm .76 \quad \text{for } \pm 1 \text{ helicity.} \qquad \text{(III-3)}$$

By measuring the sign of P, we determine photon helicity. This can be done with circularly polarized 2.18μ selective optical pumping as described in Chapter II, except propagating the ir beam along $\hat{x}$ instead of $\hat{z}$. Alternatively, if we apply a magnetic field along $\hat{y}$, the polarization along $\hat{x}$ will precess into the $\hat{z}$ axis (Hanle effect, Section E, Chapter IV).

I. Cell and Electrodes

The quartz cell which confines the thallium remains the most difficult technological problem in the experiment. It has undergone at least seven different major design changes since the model which was used to measure the M1 amplitude in 1976. All cells must be made out of fused quartz, since this is the only material known which is:

1. transparent at 293 nm, 323 nm, and 2.18μ;
2. non-birefringent;
3. able to withstand temperatures of 800°C for long periods; and
4. relatively nonreactive with thallium.

In addition, an electric field must be present in the interaction region, and this is produced by electrodes either inside or outside of the cell. The cell consists of four parts: the main body, the stem region with a reservoir of thallium, the pumpout pipe which is connected to a vacuum system, and the electrodes.

Figure III.10 shows a cell design with external electrodes which we have used extensively, but which we have recently replaced. It consists of two suprasil spectrophotometer cells (Precision Cells) which have been fused together at their open ends. A quartz stem extends down from the middle. This contains a tantalum boat which holds the thallium metal. During the experiment, this portion is 50°C cooler than the main part of the cell to provide a condensation point for the thallium. A tube extends up from the main body and connects to a remotely actuated ground quartz ball-and-socket valve, as shown. The valve connects to a pipe which leads out of the oven, and eventually out of the rough vacuum can to a Varian Vacion pump, and an adsorption pump.

When a new cell is installed, or an old cell is recharged with fresh thallium, it must be baked out to keep compounds of Tl from forming. The adsorption pump is used in the early stages of this process; as the pressure drops below 10^{-4} torr, the Vacion pump takes over. When the temperature of the stem goes above 500°C, the ball valve must be closed to avoid losing thallium. The purification process is then continued by the use of a getter (Getterloy) which continues to adsorb impurities, possibly oxygen from dissociating Tl_2O or Tl_2O_3. The normal operating rage for the cell is 750-800° C, and the thallium density determined by the stem temperature is $\sim 10^{15}$ cm^{-3}.

Figure III.10 Cell with external electrodes. A: Stem holds a tantalum boat with thallium. B: Chips of getter. C: Nickel electrodes. D: Ball valve leading to pumpout pipe. E: Two spectrophotometer cells fused together.

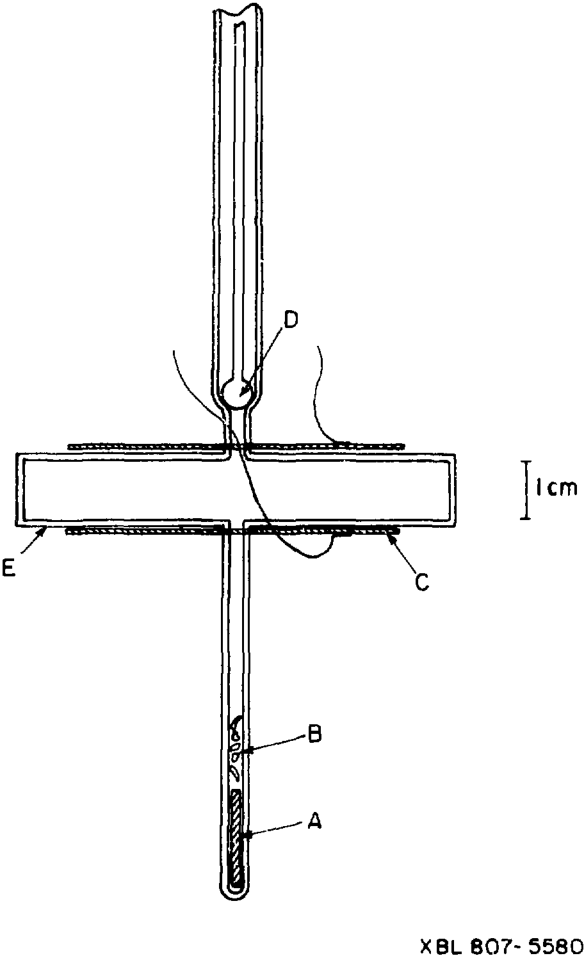

Fig. III.10

The external electrodes for this cell were made out of nickel or stainless steel, and were either attached directly to the top and bottom of the cell, or supported by the oven. Quartz becomes a fair conductor at running temperatures, and the field inside the cell from a constant potential placed on the external electrodes will largely disappear in a millisecond, due to the migration of ionic charge carriers in the quartz. The small temperature gradient in the vertical direction ($\hat{y}$) in the cell walls, caused by thermal conduction to the cool pumpout pipe, produces a dramatic asymmetry in the effective electric field when the potential V on the electrodes is reversed. If the negative plate is on top, ions are forced into a cooler region, where they become immobile, and the field is cancelled to a lesser degree; if the positive plate is on top, ions are forced into a warmer region and the field cancellation is more complete. This effect can cause signal asymmetries of as much as 10-20 percent. To minimize this, we have built a fast pulser which uses 500 MHz transmitter tubes (Eimac 4x150A) with an SCR grid switch to form a square pulse several hundred volts high, with a 150 ns rise time and a width of 2-3 μs. The laser pulse begins immediately at the top of the rise of the electric field pulse. In this way we have limited the electric field signal asymmetry to less than 1 percent. This residual asymmetry can be eliminated by adjusting the plus and minus applied voltages to obtain an equal signal size.

Although this cell had many advantages, including small background sources and ease of construction, it was susceptible to stray electric fields in the $\hat{z}$ direction (see Section E.1, Chapter IV), so it was abandoned.

Some of our cells have had tantalum electrodes installed inside. The obvious disadvantage is that these cells are difficult and expensive to make. A possible advantage is that the field is very uniform, and cannot decay with time. A recent example is shown in Fig. III.11. The body of this cell is a 69 mm o.d. suprasil cylinder (Amersil Corp.). The electrodes are suspended from the top plate by quartz rods. The electrode feedthroughs are a unique design: tantalum wires in closely fitted quartz capillary. Unlike previous designs where we actually collapsed the quartz onto a short section of wire, these are only a sliding fit, but they are long enough to extend into the cold region of the vacuum can. Thallium migrates up the tube until it condenses, and then it forms a permanent plug so that no more can escape.

This cell showed great initial promise, but after a few days it developed large electric field dependent backgrounds. These are the bane of all internal electrode cells. Although it now seems clear that the backgrounds have a number of sources, they are all associated with the presence of metal and scattered uv in the cell.

These unacceptable electric field backgrounds temporarily forced us to reconsider cells with external electrodes. A design which possibly unites the advantages of the previous two cells is shown in

Figure III.11 Cell with internal electrodes. The quartz capillary tubes A are electrical feedthroughs. B: 69 mm Suprasil cylinder. C: Tantalum electrodes. D: Getter.

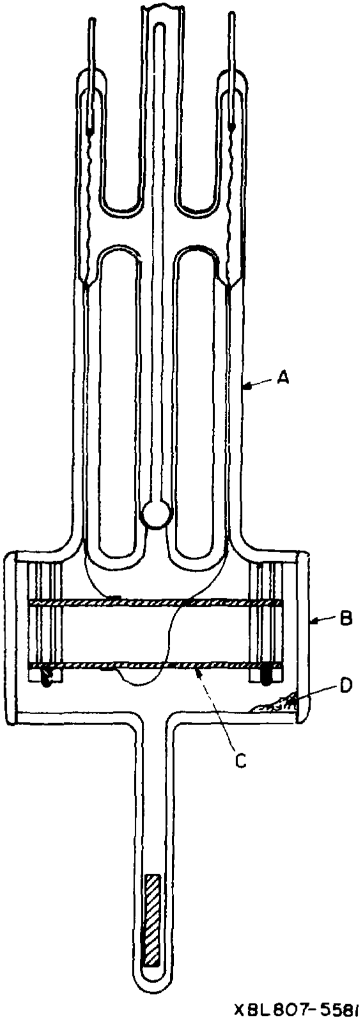

XBL807-5581

Fig. III.11

Fig. III.12. The electrodes are external, but the vertical cell walls are still far away from the electric field. We believe that this hydrid design would be free of large backgrounds and stray electric fields.

The hybrid cell with external electrodes is rather difficult to construct. The first model of this cell exploded on the glassblower's work bench while undergoing leak testing. We have returned to the cell in Fig. III.11, and are having more success with it. The electric field background becomes much smaller when the electrodes are baked in a vacuum furnace prior to installation in the quartz cell, and when care is taken to avoid scattered uv light on the electrode surfaces. This cell now has a background of less than 50 v/cm equivalent.

J. Oven Design

The cell is suspended by its pumpout pipe in a stainless steel oven which is heated electrically Care has been taken to eliminate stray magnetic fields by winding the heater wires in symmetrical pairs of counterpropagating helices, and by the simple expedient of using alternating heater current to randomize residual effects. The precaution of gating the heaters off during a laser pulse has never been necessary. A separate stem heater maintains the stem temperature below the main temperature, and determines the vapor pressure. The oven contains four 1 1/2 inch f/1 quartz lenses, two focused on each interaction region, to collect 323 nm light. It also has 3/8" holes for the uv and ir laser beams to enter and leave. The temperature is measured with chromel-alumel thermocouples in the main and stem ovens.

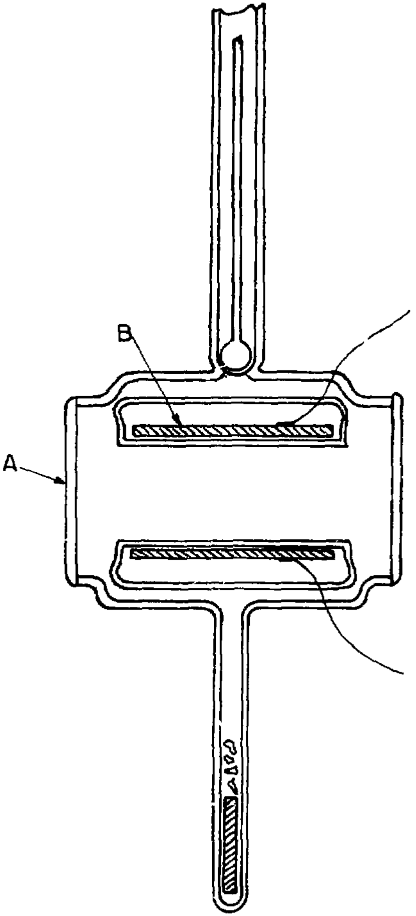

XBL 807-5582

Figure III.12 New cell design with external electrodes. A: 69 mm Suprasil cylinder. B: Disk shaped electrodes.

Since, at these temperatures, the principal heat loss mechanism is radiation, three stainless steel heat shields completely surround the oven.

The ovens are enclosed in a vacuum can where a pressure of 1μ is maintained. Quartz becomes semipermeable at high temperatures, and this keeps impurities from diffusing into the cell. In addition, stress birefringence in the cell windows is reduced. The vacuum is purposely kept poor to prevent what we believe to be chromium from diffusing out of the stainless steel at high temperatures. The chromium attacks quartz and permanently fogs the lenses and cooler parts of the cell when the vacuum is below 10^{-4} or so. In rough vacuums the stainless steel oxidizes instead of reducing, and the oxide does not harm the quartz.

The vacuum can contains on off-axis rotating window in the front through which the uv beam enters. A bellows attaches to a tilt mount in the back. This holds a dielectric mirror to reflect the uv light back through the cell. The mirror is back-surfaced, so that contamination which beams out of the oven cannot harm the dielectric film. It is also mounted on an off-axis rotating seal, so that we can move it to a clean spot when it becomes dirty. A two inch gate valve can isolate the tilt mount bellows from the rest of the vacuum, and an axuiliary pump can be used to evacuate it separately. This air lock arrangement allows us to remove the mirror for cleaning, which must be done every twelve hours or so during a run. We can also replace the mirror with a window for alignment of the uv laser beam, while the ovens are hot.

Water cooled magnetic field coils, capable of producing 8 gauss fields in the $\hat{x}$ direction, have been placed along the uv axis. These are used for diagnostic purposes (see Section E). Large diameter coils along the $\hat{y}$ axis outside the vacuum system can be used to cancel the earth's field (see Fig. IV.13).

K. Frequency Monitor Cell

Figure IV.14 is a plot of 7P population as a function of frequency which was obtained by scanning the laser across the hyperfine structure and observing the $7S \rightarrow 6P_{3/2}$ fluorescence at 535.0 nm. For laser polarization $\hat{\varepsilon} \parallel \vec{E}$ in the cell, only the 0-0 transition is allowed; for $\hat{\varepsilon} \perp \vec{E}$, only 0-1 transition is allowed. This fact is used to monitor the frequency of the light. After the uv laser beam is reflected through the thallium cell twice, it leaves the vacuum can. It then goes through two 90° reflections from aluminum mirrors with orthogonal planes of incidence. The retardation effects of each reflection cancel, leaving the beam still circularly polarized, but deflected along $-\hat{z}$ perpendicular to the original beam, as in Fig. III.1 (b). It then passes through a fixed quarter wave plate, which changes the ± helicity photons into alternating $\hat{\varepsilon}_x$ or $\hat{\varepsilon}_y$ polarizations. The light enters a second vacuum can which houses a separate oven and thallium cell with external electrodes. This cell is viewed by a single 8575 phototube with a 535 nm filter. By observing the signal asymmetry between $\hat{\varepsilon}_x$ and ε_y, the frequency can be determined directly, in terms of the ratio I(0-1)/I(0-0).

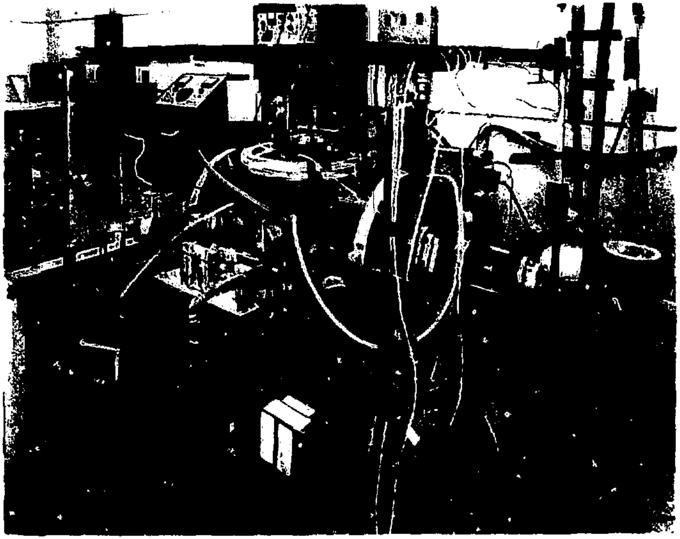

XBB 807-8796

Figure III.13 Vacuum can which houses the oven and cell. The bellows on the right is an airlocked tilt mount for the uv mirror. The bellows on top holds the cell in place by means of the pumpout pipe. The ir circular polarizers are in front, mounted on a pneumatic rack and pinion switching mechanism. Magnetic field coils are used for canceling the earth's field and for diagnostic purposes.

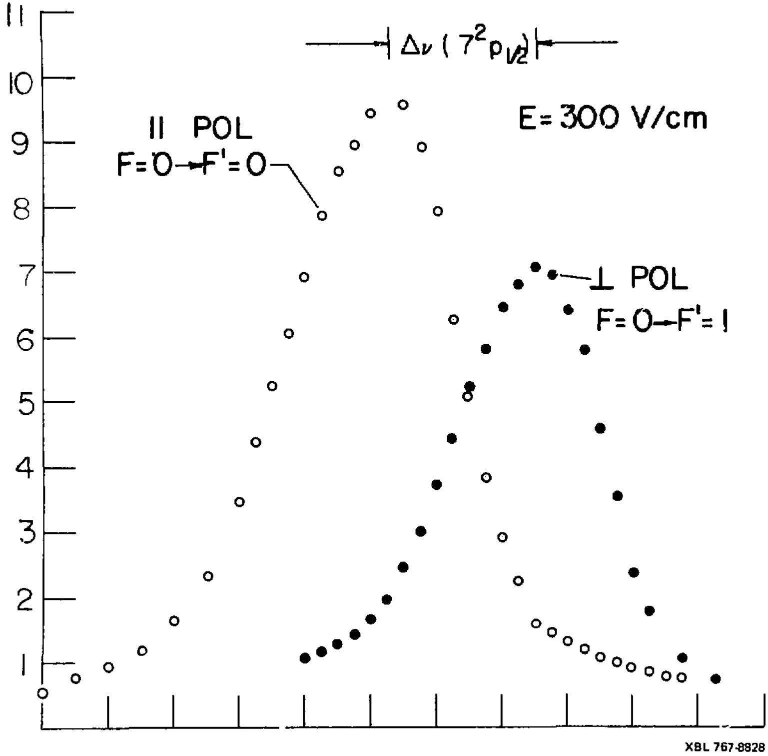

Figure III.14 Stark induced absorption for $6P_{\frac{1}{2}} \rightarrow 7P_{\frac{1}{2}}$, (0→0) and (0→1) lines. Note that the lines are slightly askew, due to the isotope shift in $T\ell^{203}$.

The requirements for the monitor cell are much less stringent than for the main cell. The spectrophotometer-type cell is sealed, and a single external electrode on top is pulsed with 2000 V from a high voltage pulse transformer. The other electrode is a grounded platform on which the cell rests. The density of thallium is an order of magnitude lower than in the main cell, to keep the background due to impurities small.

L. Frequency Control

The signal from the monitor photomultiplier tube is integrated and amplified twice, as shown in Fig. III.15. The computer selects which amplifier output pulse to digitize, depending on which polarization is present. It also can inhibit the monitor electric field in order to measure the background in the monitor cell. The ratio I(0-1)/I(0-0), corrected for background dilution, is averaged over 256 pulses. If the frequency of L1 has drifted, a correction is applied by the computer, via a D to A converter (PMI DAC-08) and a high voltage op-amp (Burleigh RC-42), to the piezoelectric crystal which tilts the thick etalon of L1.

M. Detectors

Each interaction region is viewed by two photomultiplier tubes (see Fig. III.16). The 323 nm fluorescence is collimated by the f/1 lenses in the oven. It passes through holes in the heat shields, and then through windows in the detector ports. These windows are cooled by a flowing filtered solution of phthalic acid (6 gm potassium acid phthalate per liter distilled water). The acid is a liquid filter

Figure III.15 Detection electronics. A: 9750 QB (EMI) photomultipliers. B: FET charge integrators. C: Computer controlled preamplifiers. D: High rate linear amplifiers. E: Pulse stretchers.

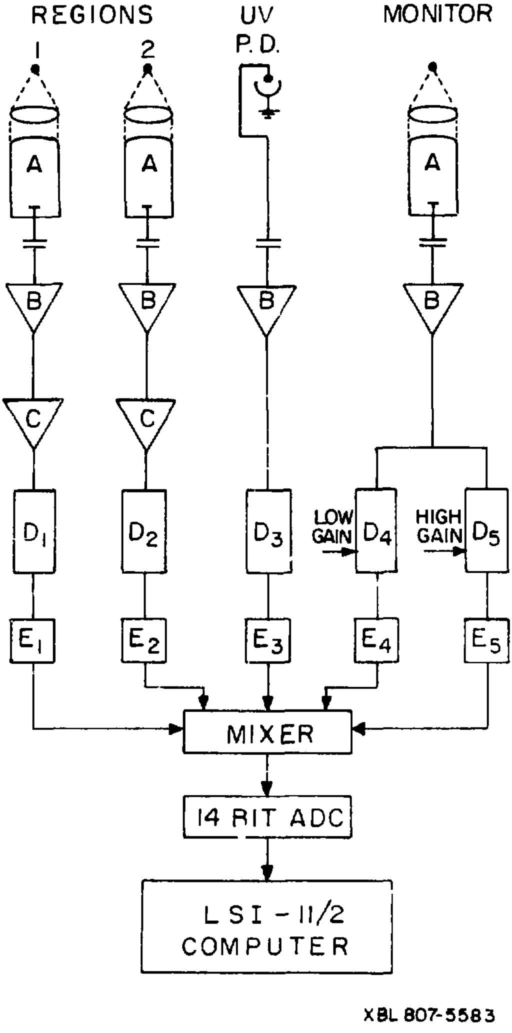
REGIONS
1
2
UV
P.D.
MONITOR
A
A
A
B
B
B
B
C
C
LOW GAIN
HIGH GAIN
D1
D2
D3
D4
D5
E1
E2
E3
E4
E5
MIXER
14 RIT ADC
LSI - 11/2 COMPUTER
XBL 807-5583

Fig. III.15

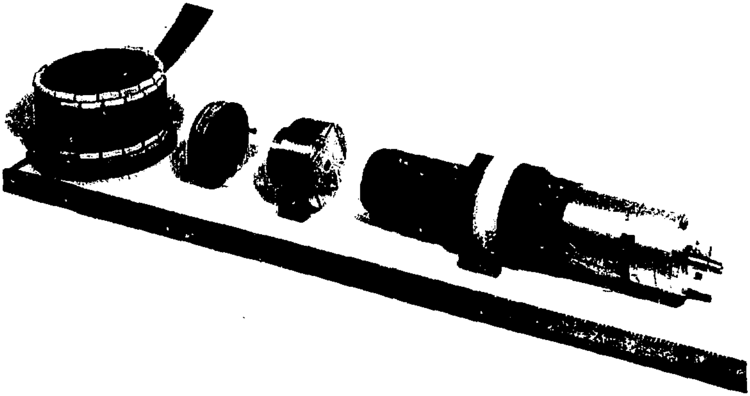

CBB 784-4092

Figure III.16 323 nm detection. Left to right: Quartz lens (in oven); phthalic acid cell (not shown); 323 nm interference filter; spatial filter; photomultiplier.

with a sharp lowpass cutoff between the 293 nm laser wavelength and the 323 nm signal wavelength (Kasha 1948). Unlike most organic filters, it does not fluoresce, so it is an ideal first filter. Tests show that the scattered light whicn gets through this has already been downshifted by fluorescence in the quartz. Next in line is a 3 nm bandwidth interference filter at 323 nm (Continental Optics), which also contains a UG-11 infrared and visible blocking filter (Schott). Finally, there is a spatial filter consisting of a 1 1/2 inch f/1 quartz lens and an aperture at the focus. This increases the signal to background ratio by an additional factor of 2, but it also reduces the signal somewhat because of the large spherical aberration in the quartz lenses. The total transmission of the filters is about 20 percent.

The photomultiplier tubes are 9780 QB (EMI), with bialkali photocathodes and quartz windows. The quantum efficiency is about 25 percent, and the tube gain is 10^4. On each laser pulse about 10^4 photoelectrons are produced at the photocathode. In order to avoid space charge saturation in the last dynodes, the tube gain has been reduced by connecting the last two dynodes to the anode. This improves the linearity, and does not appear to produce any ill effects in the venetian-blind type tubes. We operate the photocathodes at negative high voltage, and surround them with electrostatic shields. The anodes are close to ground. The tubes are enclosed by mu-metal to protect them from the magnetic fields we occasionally apply in the vacuum can.

N. Detection Electronics

The anodes of the two tubes which view each region are connected together, and capacitively coupled to charge integrating preamps. The preamps are homemade, consisting of an FET op-amp (National Semiconductor LF356H) with a switch selectable series feedback capacitor. When the lasers fire, the output of the preamps is a step function proportional to the total fluorescence in the interaction region. The greatest source of noise is the statistical fluctuation in the number of photoelectrons emitted by the photocathode of the tube (about 1 percent). The preamp outputs are ac coupled into high rate linear amplifiers (11 x 5501) with a time constant of 8 μs. The signals are then put into pulse stretchers (11 x 9421). These are active sample-and-hold devices which store the signals in analog form until a 14-bit A to D converter (ADAC Corp.) can digitize them. The whole process has been designed so that no component introduces electrical noise or digitizing noise above 10^{-3} per laser pulse.

O. Counting Statistics

The random fluctuations in the measured polarization are primarily caused by photon counting statistics. The fluorescent intensity, in turn, depends on the thallium density, collection efficiency, and the square of the electric field. A figure of merit for the data collection efficiency is the time (or number of shots) required to reach a given standard error for a given M1 polarization Δ_M. We define

$$\eta = \left[\frac{\Delta_M}{(\sigma_M)_{256}}\right]^2 ,$$

the square of the ratio of Δ_M to the standard deviation based on bins of 256 shots. Then the time required to reach a desired precision is proportional to η^{-1}.

The operating points are chosen to maximize η. Naturally, increasing the uv power helps by reducing σ_M, until photon counting statistics no longer dominate σ_M. We must also work at a field where the signal is above the background, since dilutions reduce η quadratically. Increasing the density helps to a point, but above 10^{15}cm^{-3} backgrounds increase faster than signal.

If we neglect background dilutions, changing the electric field has no effect on η, since $\Delta_M = -2M/(\beta E) \propto E^{-1}$, and $\sigma \propto 1/\sqrt{\text{signal}} \propto E^{-1}$. In practice the allowable electric field is bracketed on the low side by background dilutions which reduce the numerator of η, and on the high side by random noise sources (principally fluctuations in the OPO) not caused by counting statistics, which begin to dominate σ.

CHAPTER IV: SYSTEMATIC ERRORS AND CORRECTIONS TO THE DATA

A. Introduction

Although the parity violating effects in thallium are larger than in any other atom under investigation, they are still terribly small. The "instrumental parity," i.e., the parity-violating asymmetry which our apparatus records, is typically $1\text{-}2\times10^{-5}$. We have tried to eliminate all sources of systematic "false parities" by building an instrument with a high degree of symmetry. This was described in the previous chapter. To summarize:

1. Two interaction regions are viewed on each laser shot. They have the opposite handedness, defined by $\vec{\sigma}_{uv}$, $\vec{E}$, and $\vec{\sigma}_{ir}$. ($\vec{\sigma}_{uv}$ and $\vec{\sigma}_{ir}$ are the angular momenta of the uv and ir photons.)
2. $\vec{E}$ reverses on each shot.
3. $\vec{\sigma}_{uv}$ reverses every two shots or so, according to a syncopated rhythm which eliminates the correlations between $\vec{E}$ and $\vec{\sigma}_{uv}$.
4. $\vec{\sigma}_{ir}$ switches each 128 shots in each region.
5. Data have been taken on the 0-0 transitions as a null experiment, and on backgrounds, as well as with the retroreflecting mirror blocked.

B. Data Collection

The experiment is controlled by an LSI 11/2 computer (Digital Equipment Corp.). Larry Hunter has been responsible for the design and maintenance of the running program (Appendix A, part 2). Each time the laser fires, four digitized signals are received by the computer:

two from the two interaction regions, (S_1,S_2), one from a photodiode which monitors the uv light intensity, and one from the monitor cell. In addition, a fifth word, made up of a combination of received logic pulses and the computer's own program shot counter, indicate which of the eight instrument configurations was present $(2\vec{\sigma}_{uv} \times 2\vec{\sigma}_{ir} \times 2\vec{E})$. S_1 and S_2 are summed in three registers $(\Sigma S_1)_i$, $(\Sigma S_2)_i$ and $\{\Sigma[(S_1-S_2)/(S_1+S_2)]\}_i$, where i = 1,8 represents the configuration. The first two have large standard deviations, characteristic of the ~10 percent pulse-to-pulse jitter in the signal. They are used to make calibration and systematic corrections to the data during off-line analysis. The third is dominated by photon counting noise, and is used to compile the polarization asymmetry.

The running program compiles the raw signal sizes into sixteen sums, which may be denoted by an array $S_{ijk\ell}$. Subscripts i,j,k,ℓ are 1 or 2, representing the two possible positions of the uv helicity, electric field, infrared helicity, and region, respectively. After 256 shots, each element in $S_{ijk\ell}$ contains the sum of 32 laser pulses. The computer then calculates eight polarizations by making the region subtraction:

$$P_{ijk} = (S_{ijk1} - S_{ijk2})/(S_{ijk1} + S_{ijk2}). \qquad \text{(IV-1)}$$

The P_{ijk} are then used to calculate Δ_P, Δ_M and the other polarizations. Specifically,

$$\Delta_P = \frac{1}{8}(P_{000}-P_{001}-P_{010}+P_{011}-P_{100}+P_{101}+P_{110}-P_{111}) \qquad \text{(IV-2)}$$

$$\Delta_M = \frac{1}{8}(P_{000}-P_{001}-P_{010}+P_{011}+P_{100}-P_{101}-P_{110}+P_{111}) \qquad \text{(IV-3)}$$

$$\Delta_E = \frac{1}{8}(P_{000}-P_{001}+P_{010}-P_{011}-P_{100}+P_{101}-P_{110}+P_{111}) \qquad \text{(IV-4)}$$

Δ_P is the parity violating polarization:

$$\Delta_P = 2i\mathcal{E}_p/\beta E \quad . \qquad \text{(IV-5)}$$

Δ_M is the polarization caused by the Stark-M1 interference:

$$\Delta_M = \frac{-2M}{\beta E} \qquad \text{(IV-6)}$$

Δ_E is used for diagnostics.

After 1024 shots, the computer prints out accumulated averages for Δ_M and Δ_P. An additional number which is proportional to the ratio S(0-1)/S(0-0) as measured by the monitor cell, is also printed out. With our laser pulse rate of 16-18 pps, a short printout occurs about once per minute, and the Δ_P numbers have a standard deviation (σ) of $(1.5-4)\times10^{-4}$, depending on running conditions. The line ratio generally stays within 20 percent of its preset value (usually 15) in the monitor cell, which turns out to be a ratio of about 10 in the main cell. The discrepancy is due to the 7P-8S transition in the main cell (see Fig. II.4).

After calculating the averages for the short printout, the computer immediately returns to running the experiment. It continues on the same hyperfine line for a present number of shots, and then instructs the experimenter to switch lines. During the run, various different running conditions are imposed by the computer at preset intervals. These are:

1. Blocking the uv reflector. This prevents 292.7 nm light from returning through the cell after reflection. The M1 polarization Δ_M which reverses with $\vec{k}_{uv}$ assumes its full value. Δ_P should be unaffected. σ goes up, since part of the signal is cut off.

2. (a) Disable the electric field. This eliminates the Stark effect, so Δ_M and Δ_P vanish. The background signal which is left is mainly scattered light from the uv lasers.

(b) Block the ir laser. This can be done instead of 2(a) to measure the electric field dependent part of the background in addition to scattered light.

3. Blocked background. The electric field is off or the ir beam is blocked and the uv reflector is blocked.

The same 24 averages are collected for each of these modes. All the averages are stored in groups of 256 shots on floppy diskettes.

A long printout, which uses data averaged over more than one set of 1024 shots, is output when we switch hyperfine transitions, or at the request of the operator. This gives more detailed information, for example:

1. Δ_P and Δ_M averaged over all data since the last line switch, with σ for each.

2. $\delta_{uv} = \left.\frac{S(uv+) - S(uv-)}{S(uv+) + S(uv-)}\right|$ Region 1 or 2.

This is the asymmetry in the total signal size for (uv+) vs (uv-), and may be nonzero for a number of reasons, to be discussed later.

3. $\delta_E = \frac{S(E+) - S(E-)}{S(E+) + S(E-)}$

This indicates whether the electric field has the same size when it is reversed. Despite our efforts, small false asymmetries remain. It seems that nature abhors perfect symmetry, even in the absence of parity nonconservation. Our task has been to identify, measure, and correct or eliminate all sources of false asymmetries and dilutions, and come up with arguments for the absence of more such effects in the data.

The two broad categories of systematics are dilutions and false asymmetries.

C. Dilution

1. Backgrounds. Dilutions are any effects which cause the asymmetry we measure to be smaller than the polarization of the atomic state. Backgrounds are a main source.

It is convenient to calibrate the size of backgrounds in terms of the electric field we would need in order for the background and Stark effect to be the same size in the 0-1 line. Thus a "100 v/cm" background is equal to the fluorescent signal at 323 nm with circularly polarized uv and ir laser light on the 0-1 line, when the electric field in the interaction region is 100 v/cm.

SCATTERED LIGHT When the laser beam passes through a window in the cell, it scatters light in a cone. This can hit the walls of the cell and be further scattered toward the detectors. Although 292.7 nm is blocked by the flowing phthalic acid liquid filter, a small amount fluoresces in the quartz cell and window, and some light is converted to the 3 nm wide passband at 323 nm.

The scattered light has always been the largest source of background in the 323 nm experiments. Through a combination of improved filter designs (described in Section D) and better cell geometry, we have reduced it significantly. Most recently, we began using a cell with vertical cylindrical walls and widely spaced internal electrodes, which has reduced our scattered light background to only 50 V/cm equivalent.

MOLECULAR BACKGROUNDS While it is known that thallium atoms do not form stable dimers (a fact of chemistry for which we are fortunate) there is a broad nonresonant background at the level of a few V/cm which is probably caused by sticky collisions between thallium atoms and impurities or each other. This was first observed at 535 nm by our group in the early days of the experiment (Chu 1976), and caused us to abandon the original zero field experiment, described in Chapter II. The frequency dependence is many cm^{-1} wide at 292.7 nm but has the narrow profile of an atomic line at 2.18μ. This tends to suggest a process such as photodissociation, in which Stark mixing from the field of a temporary neighbor causes the initial absorption:

$Tl_2 + \gamma_{292.7\ nm} \rightarrow Tl + Tl^*(7P)$, and then $Tl^*(7P) + \gamma_{2.18\mu} \rightarrow Tl^*(8S) \rightarrow Tl + \gamma_{323.0\ nm}$. We have not investigated this carefully, since these backgrounds are so small that they pose no major problem to the current experiment.

ELECTRIC FIELD DEPENDENT BACKGROUNDS We have good evidence that there are some free charges present in our cell during a laser pulse. These may be formed by multi-photon ionization, or by scattered light on the walls of the cell. The problem is generally much worse when internal electrodes are used, and especially if the electrodes are closely spaced about the path of the uv laser. Background light may be emitted by recombination fluorescence, or simply resonance scattering of electrons with thallium as they are accelerated in the electric field. In the cells with external electrodes, this background was 10 V/cm equivalent or less. In the new cell, which has internal electrodes, it can be larger.

DISCHARGES If a dc field of larger than about 100 V/cm is applied to internal electrodes, a thallium discharge may occur, depending on the specific electrode geometry. To prevent this, we pulse the field on about 1 μs before the laser pulse. Small embryonic discharges may still be present, and these can contribute to the E field dependent backgrounds.

2. <u>0-0 Dilution</u>. Figure III.14 is a scan of the 0-1 resonance for $\hat{\epsilon}\perp\vec{E}$ superimposed on he 0-0 line for $\hat{\epsilon}\parallel E$. This cleary shows the frequency resolution of the system. Since the parity violation only exists in the 0-1 line, the hyperfine transition overlap for circular

polarization causes a dilution. This can be a serious problem for imperfect polarization (see Section F). In practice, the computer controls a feedback mechanism to keep the ratio I(0-1)/I(0-0) fixed, usually at 15:1.

3. Impure ir Polarization. In section F of Chapter II, when the 7P-8S rate equations were solved, we showed that the analyzing power is a function of ir intensity and polarization, and uv frequency. The dilution is typically ~ 15 percent, but can fluctuate as high as 25 percent. Since the optical parametric oscillator needs to operate well above threshold to be stable, we generally control the intensity with graded attenuator flats.

4. Reflections. The parity violating polarization does not reverse with the direction of the uv laser, but the M1 polarization does. We therefore must correct the M1 polarization by the factor (1+x)/(1-x), where x is the fraction of light going the wrong way. This amounts to a 17 percent correction for the experiment with no uv retroreflector.

5. Dilution correction methods. All dilution mechanisms except for the window reflections affect the M1 and parity polarizations equally. The M1 was measured in a previous experiment. We therefore scale the parity violation signal by the known dilution of the M1, which we measure simultaneously. This means we do not have to know the exact sources and sizes of the dilution. All we need do is take sufficient data with the mirror blocked to measure the M1 to 15 percent. This is always done in the course of running anyway as a check for systematics in the parity channel.

An equivalent viewpoint is that we do not measure $i\mathcal{E}_p$, but rather $i\mathcal{E}_p/\mathcal{M}$. This has the ultimate drawback that our knowledge of $i\mathcal{E}_p$ is limited by our ability to measure $\mathcal{M}$ in subsidiary experiments. For the present work, our 15 percent measurement of $\mathcal{M}$ is sufficient.

D. Dilution Errors Which Can Cause False Effects

If a dilution correction D is different for the two uv polarizations, $\hat{R}$ and $\hat{L}$, then a false parity violation effect will occur. Even with $i\mathcal{E}_p = 0$, the parity channel will contain the term $\Delta_P = (-\mathcal{M}\beta E_y)D_R + (\mathcal{M}\beta E_y)D_L$. We define $D_R - D_L \equiv \delta_{uv}$, $\Delta_M = -2\mathcal{M}\beta E_y$. Then $\Delta_P = \Delta_M(\delta_{uv}/2)$.

The next two sections deal with the sources of δ_{uv}. The first, frequency jitter, has plagued us in the past but has now been completely eliminated from the experiment. The second section describes an effect which is an important correction to the data.

1. Systematic Frequency Jitter. The dye lasers in our experiment do not operate in single longitudinal or transverse mode. The frequency is constrained to a passband of 1.2 GHz or so by the intracavity selective optics, but the lineshape changes from shot to shot due to turbulence and temperature gradients in the dye. To the extent that these are random, they do no harm. In data taken during early March 1980, we began to notice effects in our data which were consistent with a systematic frequency jitter between uv+ and uvlaser shots, regardless of the state of circular polarization.

The uv circular polarizer was a quarter-wave plate and mount attached to the shaft of a motor. Since the plate position triggers the laser, care was taken to make the time interval between laser shots as uniform as possible before we began our principal run in January. This was difficult because the wheel was not dynamically balanced, so that the time interval irregularity was dependent on motor speed. Evidence indicates that this effect got much worse as time went on. Both the dye temperature and the energy discharged through the flash-lamps during a laser pulse depended on the time interval since the last shot. These could translate into a small frequency shift, as well as a systematic laser intensity asymmetry between uv+ and uv−.

We removed the quarter wave plate from the uv beam path, and measured the intensity difference $\delta_{uv} = [S(uv+) - S(uv-)]/[S(uv+) + S(uv-)]$, by observing the background (E field off). To measure the frequency shift $\Delta\nu$, we scanned the two-photon $F = 1 \rightarrow F' = 1$ resonance at 585.4 nm. $\Delta\nu$ resulted in δ_{uv} changing sign as we tuned from one side of the resonance to the other.

A systematic frequency shift can cause a false parity violation, because the 0-0 line will cause a dilution of δ_M which reverses with uv circular polarization. We can estimate the size of this false effect in our data. Let R be the ratio of 7P, F = 1 atoms to 7P, F = 0 atoms in the interaction region. R is a function of frequency, and is also weakly dependent on the infrared polarization and induced absorption rate. After correcting for the background dilution, $\Delta_M = \Delta_{M_0} \{R(\nu)/[1+R(\nu)]\}$. Then

$$\Delta_p(\text{false}) = \frac{\Delta_{M_0}}{2}\left[\frac{R(\nu+)}{1+R(\nu+)} - \frac{R(\nu-)}{1+R(\nu-)}\right] = \frac{\Delta_{M_0}}{2}\,\frac{d}{d\nu}\left[\frac{R(\nu)}{1+R(\nu)}\right]\Delta\nu \quad , \qquad \text{(IV-7)}$$

where ν^* is the frequency for uv*. From the two-photon data, $\Delta\nu \approx 30$ MHz (although for most of the parity data, it seems to average much smaller than this).

In order to eliminate this problem, we abandoned the rotating quarter wave plate altogether. The circular polarization is now produced by a Pockels cell which retards the light electro-optically. The repetition rate of the laser is controlled by an external oscillator. Systematic frequency shifts have vanished.

2. Imperfect M1 Cancellation--The Hunter Effect. The $6P_{1/2}F = 0 \rightarrow 7P_{1/2}F = 1$ Stark transition is only allowed for $\hat{\epsilon}_{uv} \perp \vec{E}$. The $F = 0 \rightarrow F' = 0$ transition goes for $\hat{\epsilon}_{uv} \parallel \vec{E}$. In other words, the thallium is a perfect linear polarization analyzer. In the idealized experiment using circular polarizations $\hat{\epsilon}_R$ and $\hat{\epsilon}_L$, $\hat{\epsilon}_R \cdot \vec{E} = \hat{\epsilon}_L \cdot \vec{E}$, so $\delta_{uv} \equiv [\text{Signal}(R) - \text{Signal}(L)]/[\text{Signal}(R) + \text{Signal}(L)] = 0$. If for some reason $\delta_{uv} \neq 0$, the M1 channel asymmetry Δ_M may be different for $\hat{R}$ and $\hat{L}$, and a false parity violation Δ_{false} may result.

Background dilution can cause Δ_{false}. The background can be slightly different due to beam motion (in the case of the rotating uv $\lambda/4$ plate) or polarization changes. Define

$$\delta_u = \frac{S(R) - S(L)}{S(R) + S(L)} \qquad \text{(IV-8)}$$

and

$$\epsilon_u = \frac{B(R) - B(L)}{B(R) + B(L)} \qquad \text{(IV-9)}$$

where S is the size of the total signal + background, and B is the size of the background which must be measured separately. Then there will be a false parity violation

$$\Delta_F = \Delta_M \frac{B}{S-B}(\delta_u - \epsilon_u) \quad , \qquad \text{(IV-10)}$$

where B and S are averages over both $\hat{R}$ and $\hat{L}$ polarizations. Δ_M is the measured M1, not corrected for dilution. Note that each quantity on the right side of this equation can be measured easily while the experiment is running. Typical values are $\Delta_M = 6 \times 10^{-3}$, $B/(S-B) = .1$, δ_u, $\delta_\epsilon \sim 1 \times 10^{-3}$ or even less, averaged over an entire data run. This gives $\Delta_F < 10^{-6}$.

If a correction is needed, it is applied after Δ_p and Δ_M are calculated. An equivalent procedure would be to perform the background subtraction before calculating the asymmetry. This is less convenient, but we have done it for some runs, and the results are almost identical to this method.

Most of our data collection is performed in the "mirror unblocked" mode, with the uv laser beam traversing the cell twice. In passing through the rear window and the back surface mirror, the uv beam generally experiences a slight polarization degradation. This means that the size of δ_{uv} is different for the forward and return beams. The false effect from this can be calculated as before. Let δ_u and ϵ_u be defined as δ_{uv} for the signal and background of the two unblocked beams. Let δ_b and ϵ_b be the same, but calculated for the blocked beam, i.e., the forward beam alone. Then Δ_{false} =

$$\Delta_{Hunter} \approx \Delta_M \frac{S_b}{S_u(S-B)_b}[2S_b(\delta_b-\delta_u) + 2B_b(\delta_u-\epsilon_b) + B_u(\epsilon_u-\delta_u)] \qquad \text{(IV-11)}$$

We call this the Hunter effect.

The second and third parts, involving ϵ, are generally insignificant. The main term is the first one. Now that we no longer switch the uv polarization mechanically, $\delta_b-\delta_u$ is limited only by the stress birefringence in the cell windows and in the back surface mirror. Averaged over an entire run can keep this to the 10^{-3} level, although sometimes it is a little worse. At this level the correction is still significant, so we must subtract the Hunter correction from the parity channel asymmetry.

Still another false asymmetry comes about because of imperfect resolution of the $7P_{1/2}$ hyperfine structure. It is described in Section F, the "η cos δ" effect.

E. Systematics Induced by Misaligned Electric Fields

A static electric field $\pm E_y$ of 100-300 V/cm exists in the thallium interaction region during a laser pulse. In the idealized experiment, the field is totally along the y-axis perpendicular to both $\vec{k}$ (the uv beam direction) and $\boldsymbol{\ell}$ (the ir beam direction). In the real experiment, however $\vec{k}$ defines the $\hat{x}$ axis, and the 2.18μ light defines the $\hat{x}$-$\hat{z}$ plane. $\vec{E}$ may then have $\hat{x}, \hat{y}$, and $\hat{z}$ components. Also, $\vec{E}_+$ and $\vec{E}_-$ may differ in both magnitude and direction. We will now analyze the consequences of this.

Let $\vec{E} = E_x\hat{x} + E_y\hat{y} + E_z\hat{z}$. We are concerned with the $6P_{1/2}F = 0 \rightarrow 7P_{1/2}F' = 1,0$ transitions which are induced by Stark effect electric dipole, and will neglect both the M1 and parity violating E1 transitions. Since $\vec{k}$ is in the $\hat{x}$ directly, $\hat{\epsilon}_{uv}$ may have $\hat{y}$ and $\hat{z}$ components: $\hat{\epsilon}_{uv} = \hat{\epsilon}_y + \hat{\epsilon}_z$, where $|\epsilon_y|^2 + |\epsilon_z|^2 = 1$. It is straightforward to extend the results of Section C of Chapter II to an arbitrary electric field direction: Define new coordinate axes $\hat{x}'$, $\hat{y}'$, and $\hat{z}'$ such the $\vec{E}$ lies along $\hat{y}'$, and $\hat{\epsilon}_{uv}$ lies in the $\hat{y}'$-$\hat{z}'$ plane. Then, reading from Table II-1

$$\psi'_{01} = \begin{pmatrix} \dfrac{i\beta E\epsilon_{z'}}{\sqrt{2}} \\ 0 \\ \dfrac{-i\beta E\epsilon_{z'}}{\sqrt{2}} \end{pmatrix}, \quad \psi'_{00} = \alpha E\epsilon_{y'} \qquad \text{(IV-12)}$$

Now rotate this state back to the unprimed axes. The result is:

$$\psi_{01} = \beta \begin{pmatrix} \frac{i}{\sqrt{2}} E_y \epsilon_z - \frac{1}{\sqrt{2}} E_x \epsilon_z + \frac{i}{\sqrt{2}} E_z \epsilon_y \\ - E_x \epsilon_y \\ \frac{-i}{\sqrt{2}} E_y \epsilon_z \ \frac{1}{\sqrt{2}} E_x \epsilon_z - \frac{i}{\sqrt{2}} E_z \epsilon_y \end{pmatrix} \qquad \text{(IV-13)}$$

$$\psi_{00} = \alpha[E_y \epsilon_y + E_z \epsilon_z] \qquad \text{(IV-14)}$$

Note that $\psi_{00} = \alpha(\hat{\epsilon} \cdot \vec{E})$, and $\psi_{01} = \beta \vec{d} \cdot \vec{E} \times \hat{\epsilon}$, where tne components of $\vec{d}$ form a rank 1 irreducible tensor.

1. Electric Field Induced Polarization. When the light is circularly polarized, $\hat{\epsilon} = (\hat{\epsilon}_y \pm i \hat{\epsilon}_z)/\sqrt{2}$. Substituting this into Eqs. IV-13) and (IV-14),

$$\psi_{01} = \beta \begin{pmatrix} \mp \frac{E_y}{2} \mp \frac{iE_x}{2} + \frac{iE_z}{2} \\ - \frac{E_x}{\sqrt{2}} \\ \pm \frac{E_y}{2} \mp \frac{iE_x}{2} - \frac{iE_z}{2} \end{pmatrix} \qquad \text{(IV-15)}$$

$$\psi_{00} = \frac{\alpha}{\sqrt{2}} (E_y \pm iE_z) \qquad \text{(IV-16)}$$

The polarization of ψ_{01} is

$$P_E = \mp \frac{2E_x E_z}{E_y^2} , \quad \text{for } E_y^2 \gg E_x^2 , \ E_z^2 . \qquad \text{(IV-17)}$$

The ∓ sign means that this polarization reverses when the circular polarization switches. In this respect it behaves the same as a partiy violation. However, it is even in the field E, so that when $E_+ \to E_-$, P_E is unchanged. We may therefore expect that this effect will cancel to the precision with which we reverse E. The field may be separated into reversing and non-reversing components: $\vec{E}_+ = \vec{E}_0 + \Delta\vec{E}$; $\vec{E}_- = -\vec{E}_0 + \Delta\vec{E}$. The false parity violating asymmetry is

$$\Delta_{false} = -\frac{(E_{ox} + \Delta E_y)(E_{oz} + \Delta E_z)}{(E_{oy} + \Delta E_y)^2} + \frac{(-E_{ox} + \Delta E_x)(-E_{oz} + \Delta E_z)}{(E_y - \Delta E_y)^2} \qquad \text{(IV-18)}$$

$$\Delta_{false} = -\frac{2E_{ox}\Delta E_z + 2E_{oz}\Delta E_x}{E_{oy}^2} + \frac{4E_{ox}E_{oz}\Delta E_y}{E_{oy}^3}, \qquad \text{(IV-19)}$$

where we assume $E_{oy} >> \Delta E_y$ so that we can expand the denominator. If we assume, as seems reasonable, that $\Delta E_i/E_i$ is the same order of magnitude for all i, and that $E_x \approx E_z \lesssim \Delta E_y << E_y$, then the three terms are all the same order of smallness. Curiously, if all $\Delta E_i/E_i$ are equal, the expression vanishes exactly. That is when the reversal direction is perfect.

During the experimental runs of Winter and Spring 1980, we continuously monitored $2\Delta E/E$, and $(2E_{ox}E_{oz})/E_y^2$. The first is obtained by separately averaging over all signals with E_+ and E_-, and calculating the asymmetry. Since the signal "S" is proportional to E^2,

$$\frac{S(E_+) - S(E_-)}{S(E_+) + S(E_-)} = \frac{2\Delta E}{E} \equiv \delta_E \ . \qquad \text{(IV-20)}$$

The second quantity is a polarization which is averaged over E_+ and E_-, but reverses sign with the uv polarization, ir polarization, and region. The computer compiles each of these averages continuously. This is all the information which can be extracted from the data about the misaligned and non-reversing fields while the parity violation experiment is running. More can be learned from auxiliary experiments with linear uv polarization or magnetic fields (see the next section). From the data, we concluded:

(a) $\Delta E_y/E_y \approx 4 \times 10^{-3}$ averaged overall, and is occasionally as large as 10^{-2} for short periods (a few hours, typically at the beginning of a run before temperatures have become stable.)

(b) $(E_{ox}E_{oz})/E_y^2 \approx 1 \times 10^{-4}$, and is always within 30 percent of this value regardless of other running conditions. E_{ox} and E_{oz} might be expected to wander with beam alignment, except that a system of fixed apertures kept the beams from wandering by more than about 2 milliradians.

Based on this information and the assumptions in the preceding paragraph, we presumed that the maximum false effect in the parity violating channel for our cell with external electrodes was ~ 2×10^{-6}. Since this was below our anticipated total uncertainty, we felt it was safe to run. Unfortunately, this was wrong. Nature can be subtle. Table IV-1 lists our current measured values for the misaligned and nonreversing fields, and our requirements. Section H is a description

Table IV-1. Systematic effects, measured in two cells

Field	Measured Value		Methods(s) of Measurement	Required size[a]
	external electrodes(4/80)	internal electrodes(6/80)		
ΔE_y	$4\text{x}10^{-3}$	0 (adjustable)	during run	$<10^{-2}$
E_{ox}	$4\text{x}10^{-3}$	$5\text{x}10^{-3}$	apply B_x	$<5\text{x}10^{-3}$
E_{oz}	$2\text{x}10^{-2}$	10^{-2}	$\eta \sin \delta$ effect apply B_x	$<5\text{x}10^{-3}$
ΔE_z	$<10^{-3}$(region 1) $2\text{x}10^{-3}$ (region 2)	$4\text{x}10^{-4}$	linear pol. at 45°	$<5\text{x}10^{-4}$
ΔE_x	$<2\text{x}10^{-4}$, consistent with zero	$5\text{x}10^{-4}$, consistent with zero	apply B_x	$<4\text{x}10^{-4}$
$E_{ox}E_{oz}$	$2\text{x}10^{-4}$	consistent with zero	during run	$<3\text{x}10^{-5}$

[a] Required Size column is based on required Δ_{false} x $2\text{x}10^{-6}$.

of the auxiliary experiments which measured these quantities. The table shows that the assumption $\Delta E_z/E_z = \Delta E_y/E_y$ is invalid, and that ΔE_z is much larger than is acceptable with the small cell design. After discovering this, we designed larger cells with internal or external electrodes which are currently in use (see description, Chapter III).

The methods used to discover the sizes of the residual electric fields are the subject of Section H. The mechanism for a large ΔE_z in the cell with external electrodes was discovered experimentally. We found that by moving the position of the uv beam from side to side, it was possible to change the size of ΔE_z, or even reverse it. We now think that it is caused by a build up of static positive charge on the sides of the cell. When the uv beam strikes the cell wall which is at 750°C, it ejects electrons, either because of impurities in the quartz or contamination on the surface. These electrons are swept away very quickly, since they are deep within the region of the externally imposed field. The resulting net positive charge is the source of ΔE_z. Small imperfections and misalignments insure that the charge will not be equal on two opposite sides of the cell, but by moving the beam, this can be altered. The only permanent solution to this problem is a cell with walls as far as possible from the interaction region.

2. Magnetic Fields. The measured parity nonconserving polarization will be altered by the presence of perturbing magnetic fields. Three effects can occur: Hanle precession, hyperfine mixing, and Zeeman effect. In the absence of stray electric fields, the first and third are unimportant. Hyperfine mixing can cause a false parity violation, but only for fields in the $\hat{x}$ (uv propagation) direction. This will equal the predicted weak interaction effect at 11 gauss. In practice the field is about 100 times smaller than this. However, non-reversing electric fields in the $\hat{x}$ and $\hat{z}$ directions can create false effects through coupling to B_x, and are worth considering. We will now discuss these magnetic effects in detail.

HANLE EFFECT An atomic polarization with an associated magnetic moment μ will experience a torque $\vec{\mu} \times \vec{B}$ when placed in an external magnetic field. Consider, for example, the $6P_{1/2}F = 1 \rightarrow 7P_{1/2}F = 1$ Stark transition (convenient for study since it is only 21 GHz away from the transition used in this experiment). Using our standard coordinate system, we excite the transition with circularly polarized light in the $\hat{x}$ direction. The final state polarization in the $\hat{x}$ (not $\hat{z}$) direction is

$$P_x^{1-1} = \pm\frac{4\alpha\beta}{3\alpha^2 + 2\beta^2}\,, \qquad \text{(IV-21)}$$

where

1. α and β were defined in Eqs. (II-13) and (II-14);
2. The 6P state is unpolarized;
3. We assume that the upper state hyperfine splitting of 2.13 GHz is resolved. If it is not, the polarization is diluted by the 1 → 0 transition, which is proportional to β^2: $P = \pm(4\alpha\beta)/(3\alpha^2 + 3\beta^2)$. This is a 16 percent correction.

This polarization will precess towards $\hat{z}$ in a weak magnetic field $\vec{B}_y$, with a rate equal to $\omega = g_F(\mu_0 B_y/\hbar)$. ($g_F$ equals 1/3 for $P_{1/2}F = 1$ states in thallium.) If an atom undergoes a 1-1 transition at time $t = 0$, its polarization along the $\hat{z}$ direction at a later time t is $\rho_z^{11}(t) = \rho_x^{11}(t = 0) \sin \omega t$. It will decay with probability $e^{-At}dt$, where A is the spontaneous decay rate. the average polarization of the emitted light in the $\hat{z}$ direction is

$$\langle P_z \rangle = \frac{\int_0^\infty \rho_z^{11}(t) e^{-At} dt}{\int_0^\infty e^{-At} dt} = \frac{\omega/A}{1+(\omega/A)^2}\, \rho_x^{11}(t=0) = \pm \frac{\omega/A}{1+(\omega/A)^2}\, \frac{4\alpha\beta}{3a^2+2\beta^2} \qquad \text{(IV-22)}$$

This is the Hanle effect. It was observed by us in a previous experiment (Conti et al. 1979, Commins 1978a), and provides the best measurement of the $7P_{1/2}$ lifetime (Fig. IV.1).

The Hanle effect in the present experiment is far more complicated, since the $7P_{1/2}$ and $8S_{1/2}$ states are coupled by an intense 2.18μ

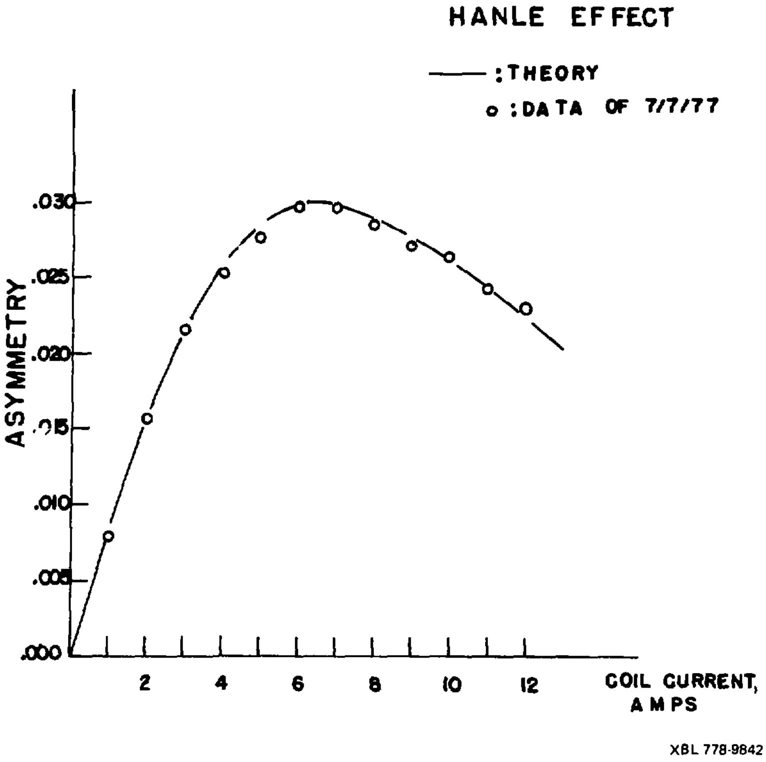

Figure IV.1 Hanle effect: polarization along $\hat{z}$ vs magnetic field along $\hat{x}$ for (1→1) line α-β Stark interference (see text).

laser field which is circularly polarized along $\hat{z}$. The magnetic field and the laser radiation field both cause the atomic polarization to precess. Spontaneous fluorescence can take place from the $7P_{1/2}$ or 8S state. Because atomic coherence is important in the Hanle precession, we must solve Schrödinger equations to find the explicit time dependence of the coupled 8S-$7P_{1/2}$ system. Since our 2.18μ laser source is 60 GHz wide, it does not resolve the 2 GHz hyperfine structure, so we could do the problem in the (J,m_J) basis. However, for greater clarity we have used the usual (F,m_F) basis. The states are labeled in Fig. IV.2. P(Q) is the $7P_{1/2}$(8S) magnetic field precession frequency $g_F eB/(2mc)$, where

$$\begin{aligned} g_F &= 1 \quad \text{for } 8S \quad F = 1 && \text{(IV-23a)} \\ &= 0 \quad \text{for } 8S \quad F = 0 && \text{(IV-23b)} \\ &= 1/3 \quad \text{for } 7P_{1/2} \quad F = 1 && \text{(IV-23c)} \\ &= 0 \quad \text{for } 7P_{1/2} \quad F = 0. && \text{(IV-23d)} \end{aligned}$$

The time dependent Schrödinger equation is ($\hbar = 1$)

$$i\dot{a}_m = \sum_n \langle m|H'|n\rangle a_n e^{-i(\omega_n-\omega_m)t} \quad . \qquad \text{(IV-24)}$$

In our problem

$$H' = H_{MAG} + H_{RAD} = -\mu_{ATOM}\cdot\vec{B} - \frac{e}{mc}\vec{A}_{RAD}\cdot\vec{P}_{ATOM} \qquad \text{(IV-25)}$$

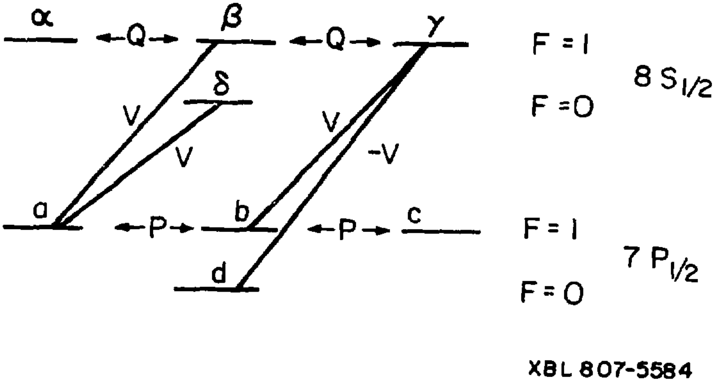

Figure IV.2 Hanle effect transitions with 7P → 8S coupling via circularly polarized ir light. Labels identify terms in Eq. (IV-29) in the text.

The second term in H' reduces, for an allowed electric dipole transition, to $ie(2\pi\omega_\gamma\rho_\gamma)^{1/2}\hat{\epsilon}\cdot\vec{r}_{ATOM}$ [see, for example, Sakurai (1967), Chapter 2]. Hence ω_γ is the photon angular frequency, and ρ_γ is the density of photons in the transition bandwidth $\Delta\omega$. For convenience, we will relate this to the rate R for stimulated absorption for $|n\rangle$ to $|m\rangle$:

$$R = (2\pi)^2 \alpha I_0 \langle m|\hat{\epsilon}\cdot\vec{r}\,|n\rangle, \tag{IV-26}$$

where I_0 is the intensity of the light/unit bandwidth: $I_0 = (\rho_\gamma\omega_\gamma c)/\Delta\omega$, so

$$\langle 8S|H'_{RAD}|7P_{1/2}\rangle = i(R\Delta\omega/2\pi)^{1/2} \equiv iV. \tag{IV-27}$$

Now, since the laser bandwidth is so large, $\Delta\omega$ is just the power broadened width of the transition: $\Delta\omega = R + 1/2\ (A_{7P} + A_{8S})$. So,

$$V = \sqrt{\frac{R}{2\pi}\left[R + \frac{(A_{7P} + A_{8S})}{2}\right]} \approx iR/\sqrt{2\pi}\ , \tag{IV-28}$$

for saturated intensity. We assume $\vec{B} = B\hat{y}$ for simplicity, and consider RCP ($h = -1$) polarization. The rate equations are as follows:

$$\dot{a} = Pb + V(\beta-\gamma) - \frac{1}{2} A_{7P}a \tag{IV-29a}$$

$$\dot{b} = P(c-a) + V\gamma - \frac{1}{2} A_{7P}b \tag{IV-29b}$$

$$\dot{c} = -Pb - \frac{1}{2} A_{7P} c \tag{IV-29c}$$

$$\dot{d} = V\gamma - \frac{1}{2} A_{7P} d \tag{IV-29d}$$

$$\dot{\alpha} = Q\beta - \frac{1}{2} A_{8S} \alpha \tag{IV-29e}$$

$$\dot{\beta} = Q(\gamma-\alpha) - Va - \frac{1}{2} A_{8S} \beta \tag{IV-29f}$$

$$\dot{\gamma} = -Q\beta - V(b+d) - \frac{1}{2} A_{8S} \gamma \tag{IV-29g}$$

$$\dot{\delta} = Va - \frac{1}{2} A_{8S} \delta . \tag{IV-29h}$$

The hyperfine mixing terms $P \exp (i\omega_{\Delta 7} t)$ and $Q \exp (i\omega_{\Delta 8} t)$, where $\omega_{\Delta 7}(\omega_{\Delta 8})$ is the $7P_{1/2}(8S)$ hyperfine splitting frequency, have been omitted. They will only change the result by admixtures of order $P/\omega_{\Delta 7,8} \approx 10^{-3}$. A more important simplification is the elimination of resonance trapping from the 8S state. This will tend to randomize the phase coherence between α, β, γ, and δ, which may dilute the Hanle polarization P_z of the 7P state after stimulated transitions from 8S → 7P. Finally, we have assumed that there is no temporal phase coherence in the infrared laser. This allows us to drop the phase factor $\exp [i(\omega_\gamma - \omega_7 + \omega_8)t]$ which should multiply V.

These equations were solved numerically using a fourth order Runge Kutta integration procedure (Abramowitz and Stegan 1964). An initial polarization was applied in the $\hat{x}$ direction or the $\hat{z}$ direction at

$t = 0$. The system evolved in time, and the total number of decays from 8S was integrated separately for each polarization.

Figure IV.3 shows this analyzing power as a function of magnetic field, for various 7P–8S transition rates. As the magnetic field increases, the state which was initially polarized along $\hat{x}$ precesses into the $\hat{z}$ direction. For high pump rates [we believe that we actually pump at 200–500 MHz (transitions/sec) during the experiment] the maximum analyzing power is about 20 percent, and occurs at a magnetic field of about 7 gauss. This is further reduced by such dilution factors as imperfect infrared polarization, backgrounds, and contamination from the (0–0) transition.

We measured the Hanle effect in the coupled 7P–8S system by applying a magnetic field along $\hat{y}$ and observing the precession of the polarization along $\hat{x}$ in the (1–1) transition, P_x^{1-1}, which is caused by the interference between Stark amplitudes α and β. To account for dilution effects, we use a previous measurement of P_x^{1-1} in the $\hat{x}$ direction, obtained by making the ir and uv beams anticollinear in the cell, as in Fig. IV.4. From this we find

$$P_x^{11}(\text{measured}) = \frac{4\alpha\beta}{3\alpha^2 + 2\beta^2} \times (\text{dilution factor}) = .50 \pm .08 \quad . \qquad \text{(IV-30)}$$

Figure IV.5 shows the Hanle effect measurements, and the theoretical prediction, assuming $R = 300$ MHz. Although the fit is not completely satisfactory, we feel that the gross features are understood, and reproduced reasonably well by the model. The 20 percent reduction of

Figure IV.3 Analyzing power for Hanle effect with 2.18μ transitions: Polarization along z as a function of B, assuming that the atoms are formed with $P_x = 1$.

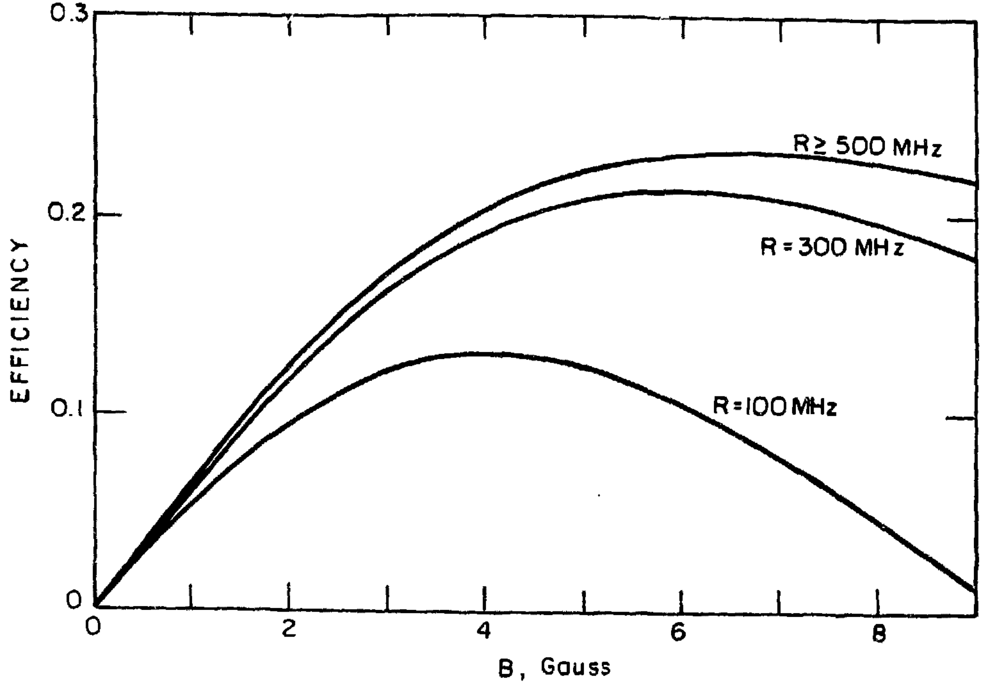

XBL 807-5585

Fig. IV.3

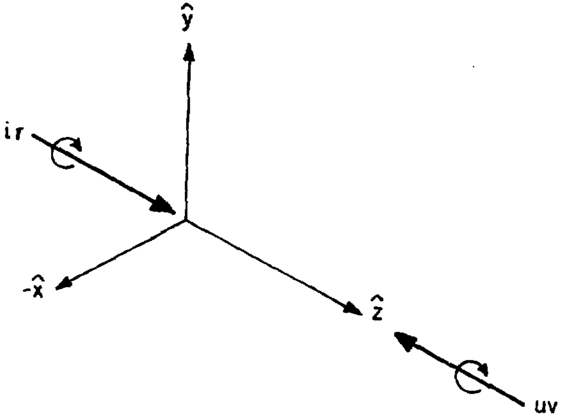

XBL 807-5586

Figure IV.4 Anticollinear experiment.

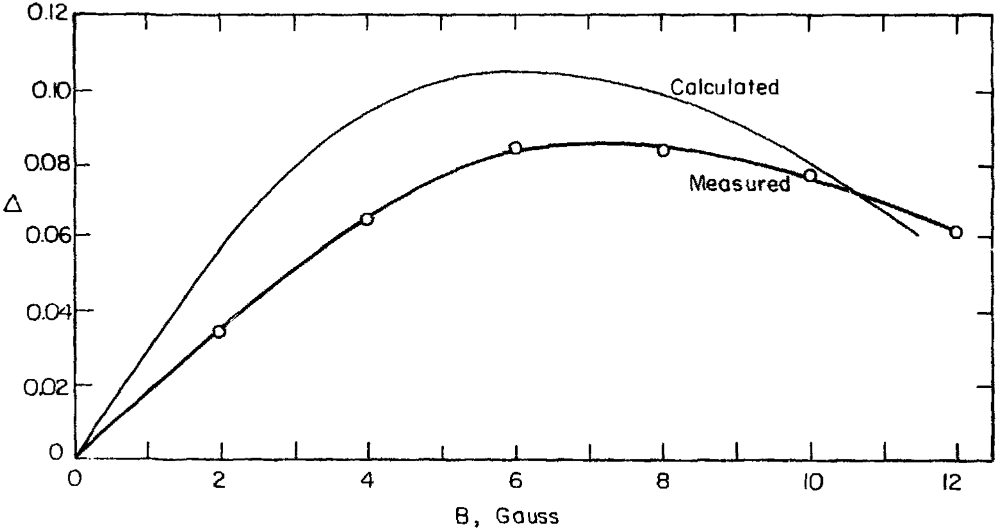

XBL807-5587

Figure IV.5 Hanle effect on the (1→1) transition, with 2.18μ pumping. Δ is the measured asymmetry in the 323 nm fluorescence which reverses with region and uv and ir helicity.

the actual analyzing power as compared to the model, is adequately explained by our neglect of resonance trapping in the 8S → $6P_{1/2}$ decay, which is a means of randomly repopulating the 8S state.

ZEEMAN EFFECT The magnetic fields present in our apparatus cause a Zeeman splitting which is much smaller than the hyperfine splitting, so only the weak field case need by considered. The frequency shift $\Delta\nu$ between the $6P_{1/2}(0,0) \rightarrow 7P_{1/2}(1,1)$ and $6P_{1/2}(0,0) \rightarrow 7P_{1/2}(1,-1)$ transitions is

$$\frac{2}{3}\,\frac{eB}{2mc} = .93B_z \text{ MHz (B in Gauss).} \qquad \text{(IV-31)}$$

B_z, due primarily to the earth's field, has been measured with a flux gate magnetometer to be 80 mg. $\Delta\nu$ = only 73 KHz. False polarizations could only result from uneven pumping between the three Zeeman states. A worst case estimate is $P_{\text{Zeeman}} \leq \Delta\nu/\Delta\nu_{\text{laser}} = 6 \times 10^{-5}$. Since this polarization will not reverse with either the electric field or the uv helicity, it will be further reduced by a factor 10^{-5} or so, and therefore we will not consider it further.

HYPERFINE MIXING When we calculated the Hanle precession we implicitly neglected magnetic mixing between F = 0 and F = 1 states, by assuming that (F,m_F) are good quantum numbers in a magnetic field. This hyperfine mixing is more important in the 6P → 7P Stark transition, where it can cause a small false parity violating signal for large enough fields.

Consider the perturbation

$$H' = -\vec{\mu}\cdot\vec{B} = -(\vec{\mu}_J + \vec{\mu}_I)\cdot B \approx -\vec{\mu}_J\cdot B \qquad \text{(IV-32)}$$

Also,

$$-\vec{\mu}_J\cdot\vec{B} = -g_J\left(\frac{J_+B_- + J_-B_+}{2} + J_zB_z\right) \qquad \text{(IV-33)}$$

where

$$B_\pm = B_x \pm iB_y \qquad \text{(IV-34)}$$

The states decompose as follows

$$\alpha = \left|\frac{1}{2},\frac{1}{2}\right\rangle ; \qquad \beta = \left|\frac{1}{2} - \frac{1}{2}\right\rangle \qquad \text{(IV-35)}$$

$|F,m_F\rangle$:

$$|1,1\rangle = \alpha_J\alpha_I \qquad \text{(IV-36a)}$$

$$|1,0\rangle = \frac{1}{\sqrt{2}}\left(\alpha_J\beta_I + \beta_J\alpha_I\right) \qquad \text{(IV-36b)}$$

$$|1,-1\rangle = \beta_J\beta_I \qquad \text{(IV-36c)}$$

$$|0,0\rangle = \frac{1}{\sqrt{2}}\left(\alpha_J\beta_I - \beta_J\alpha_I\right) \qquad \text{(IV-36d)}$$

The magnetic field mixes F = 0 and F = 1 states. Let

$$\epsilon_i^n = \frac{g_J \mu_0 B_i}{2E_n} \qquad \text{(IV-37)}$$

where E_n is the hyperfine splitting in the $nP_{1/2}$ state. To lowest order in H'_{MAG}/H'_{HFS}, the new nP states are:

$$nP|\overline{1,1}\rangle = 1,1\rangle - \frac{1}{\sqrt{2}}(i\epsilon_y^n + \epsilon_x^n)|0,0\rangle \qquad \text{(IV-38a)}$$

$$nP\ \overline{1,0}\rangle = |1,0\rangle + \epsilon_z^n|0,0\rangle \qquad \text{(IV-38b)}$$

$$nP|\overline{1,-1}\rangle = |1,-1\rangle + \frac{1}{\sqrt{2}}(-i\epsilon_y^n + \epsilon_x^n)|0,0\rangle \qquad \text{(IV-38c)}$$

$$nP|\overline{0,0}\rangle = |0,0\rangle + \frac{1}{\sqrt{2}}(-i\epsilon_y^n + \epsilon_x^n)|1,1\rangle + \frac{1}{\sqrt{2}}(-i\epsilon_y^n - \epsilon_x^n)|1,-1\rangle - \epsilon_z^n|1,0\rangle \qquad \text{(IV-38c)}$$

The transition amplitudes for $6P_{1/2}F = 0 \rightarrow 7P_{1/2}F' = 0,1$ with circularly polarized light are

$$a_{0\rightarrow 0} = \frac{\alpha E_y}{2} \mp E_y \beta(\epsilon_x^6 + \epsilon_x^7)\sqrt{2} \qquad \text{(IV-39)}$$

$$a_{0\rightarrow 1} = E_y \begin{bmatrix} \mp \frac{\beta}{2}(1+\epsilon_z^6) + \frac{\alpha}{2}(+\epsilon_x^6 - \epsilon_x^7 - i\epsilon_y^6 + i\epsilon_y^7) \pm \frac{M}{2} \\ \pm \beta\epsilon_x^6 - \frac{\alpha}{\sqrt{2}}(\epsilon_z^6 - \epsilon_z^7) - \frac{M}{\sqrt{2}} \\ \pm \frac{\beta}{2}(1-\epsilon_z^6) + \frac{\alpha}{2}(-\epsilon_x^6 + \epsilon_x^7 - i\epsilon_y^6 + i\epsilon_y^7) \pm \frac{M}{2} \end{bmatrix} \qquad \text{(IV-40)}$$

The parity violating electric dipole amplitude has been omitted. The new terms involving ϵ can cause an additional polarization ϵ_y causes no polarization, since it is out of phase with the main Stark amplitude. ϵ_z produces a large polarization $P = \epsilon_z^6$, proportional to the scalar invariant $\vec{J}\cdot\vec{B}$. Although this <u>will</u> reverse with the infrared polarization in the experiment, it does not depend on the diretion of E or the sign of the uv helicity. We may therefore ignore it. The remaining polarization is

$$P = -\frac{2M}{\beta E}\left[1 \pm (\epsilon_x^6 - \epsilon_x^7)\frac{\alpha}{\beta}\right]. \qquad \text{(IV-41)}$$

The first term is the familiar Δ_M. The second term acts exactly like a parity violating amplitude. Its size is $\Delta_M \times [2.38 \times 10^{-4}]$ B(gauss). This will equal the parity violation expected by the Weinberg model when $B_x \approx 5.5$ gauss. During the experiment $B_x < 1$ gauss in the interaction region, so we do not consider hyperfine mixing to be a serious problem.

F. <u>Imperfect Circular Polarization</u>

1. <u>The "$\eta \cos \delta$" Effect</u>. So far we have assumed that the experiment has pure circularly polarized light. We will now explore the consequences for impure polarization.

The actual polarizations $\hat{R}$ and $\hat{L}$ can be expressed in terms of pure circular polarization $\hat{\epsilon}_R$ and $\hat{\epsilon}_L$, where

$$\hat{\epsilon}_R = \frac{\hat{\epsilon}_x - i\hat{\epsilon}_y}{\sqrt{2}} \tag{IV-42a}$$

and

$$\hat{\epsilon}_L = \frac{\hat{\epsilon}_x + i\hat{\epsilon}_y}{\sqrt{2}} \tag{IV-42b}$$

The defining equations are

$$\hat{R} \approx \sqrt{1 - \eta^2}\,\hat{\epsilon}_R + \eta e^{i\delta}\hat{\epsilon}_L \tag{IV-43a}$$

$$L \approx \sqrt{1 - \eta'^2}\,\hat{\epsilon}_L + \eta' e^{i\delta'}\hat{\epsilon}_L \tag{IV-43b}$$

where η, η', δ, δ' are real and $|\eta| < 1$, $|\eta'| < 1$. We will only consider situations where $\eta^2, \eta'^2 << 1$, so the coefficients $\sqrt{1 - \eta^2}$ and $\sqrt{1 - \eta'^2}$ will be dropped. The 0-1 and 0-0 transition amplitudes are modified as follows:

$$a_{0\to 0} = \frac{\alpha}{\sqrt{2}} \to \frac{\alpha}{\sqrt{2}}\,(1 + \eta e^{i\delta}) \tag{IV-44a}$$

$$a_{0\to 1} = \begin{bmatrix} \mp \frac{\beta}{2} E \pm \frac{M}{2} - \frac{i\mathcal{E}_p}{2} \\ \\ \frac{M}{\sqrt{2}} \\ \\ \pm \frac{\beta}{2} E \pm \frac{M}{2} - \frac{i\mathcal{E}_p}{2} \end{bmatrix} \longrightarrow \tag{IV-44a}$$

$$\begin{bmatrix} \mp \beta E(1-\eta e^{i\delta}) \pm \frac{M}{2}(1-\eta e^{i\delta}) - \frac{i\mathcal{E}_p}{2}(1+\eta e^{i\delta}) \\ \\ \frac{-M}{\sqrt{2}}(1+\eta e^{i\delta}) \\ \\ \pm \frac{\beta E}{2}(1-\eta e^{i\delta}) \pm \frac{M}{2}(1-\eta e^{i\delta}) - \frac{i\mathcal{E}_p}{2}(1+\eta e^{i\delta}) \end{bmatrix} \qquad \text{(IV-44b)}$$

where ± signs refer to $\hat{L}$ (top sign) or $\hat{R}$ (bottom sign), and the quantity $\eta e^{i\delta}$ is unprimed (primed) for $\hat{R}$ ($\hat{L}$).

The false parity violating effects from $\eta e^{i\delta}$ occur because a slight difference in the relative amount of $\hat{\epsilon}_x$ vs. $\hat{\epsilon}_y$ present in $\hat{R}$ and $\hat{L}$ can cause the relative strength of the 0-0 line and 0-1 line to change. Then the M1 polarization, present only in 0-1 line, will differ for $\hat{R}$ and $\hat{L}$, causing a small false parity violation.

The polarization of the $7P_{1/2}$ state is

$$P = \frac{|A_{+1}^{0-1}|^2 - |A_{-1}^{0-1}|^2}{|A_{+1}^{0-1}|^2 + |A_{0}^{0-1}|^2 + |A_{-1}^{0-1}|^2 + F\,|A^{0-0}|^2} \qquad \text{(IV-45)}$$

F is the tuning ratio, defined by I_{0-0}/I_{0-1}. After some arithmetic, and neglecting $\mathcal{E}_p$ terms,

$$\hat{R}: \qquad P_R = \frac{4\beta M}{2\beta^2 + F\alpha^2 \left|\frac{1+\eta e^{i\delta}}{1-\eta e^{i\delta}}\right|} \qquad \text{(IV-46a)}$$

$$\hat{L}: \qquad P_L = P_R \text{ with } \eta \rightarrow \eta' \qquad \delta \rightarrow \delta' \qquad \text{(IV-46b)}$$

The false parity violation is

$$\Delta_{\text{false}} = \frac{1}{2}(P_L - P_R) \approx \frac{2M}{\beta} \times \frac{F(\alpha^2/\beta^2)}{[1 + F(\alpha^2/\beta^2)]^2} (\eta \cos \delta - \eta' \cos \delta') \quad \text{(IV-47)}$$

Note that it has the symmetry

$$\Delta_{\text{false}}(f) = \Delta_{\text{false}}(1/f) \quad . \quad \text{(IV-48)}$$

Therefore it will affect the 0-1 and 0-0 lines identically, as long as we tune to obtain the same hyperfine transition ratio in both lines, as measured in our monitor cell.

During the portion of our experiment when we used a crystalline quartz quarter-wave plate, mounted on the shaft of a motor to reverse the polarization, we were only able to reduce this "$\eta \cos \delta$" effect by careful alignment of the quarter wave plate. We tried to maintain a ratio of 12:1 on both the 0-0 and 0-1 lines, and switch between these transitions frequently, to eliminate the effects of slow drifts on the data. When we switched to a Pockels cell to produce the circular polarization, we discovered a much better way to control this systematic.

The signal size seen by the phototubes during a laser pulse with $\hat{R}$ polarization is proportional to $\beta^2 E^2(1 - 2\eta \cos \delta)$, when averaged over the infrared polarization, electric field, and regions. For $\hat{L}$, it is $\beta^2 E^2(1 - 2\eta' \cos \delta')$. We therefore constantly monitor the quantity

$$\delta_{uv} = \frac{\text{signal}(L) - \text{signal}(R)}{\text{signal}(L) + \text{signal}(R)} = \eta \cos \delta - \eta' \cos \delta' \quad . \qquad \text{(IV-49)}$$

By making small adjustment to the voltage of the Pockels cell, it is easy to keep $(\eta \cos \delta - \eta' \cos \delta') < 10^{-3}$ at all times. At this level, $\Delta_{false}/\Delta_{PNC} < .05$ for data taken with the uv retroreflecting mirror blocked; and $\Delta_{false}/\Delta_{PNC} < .01$ for data with the mirror unblocked because Δ_M is reduced.

With the older fixed quarter wave plate data, the false effect could likewise be measured, but it could not be adjusted during a run without performing a complete mechanical realignment of the quartz. We could however, correct for the effect in the analysis, by using δ_{uv}. Typical values were $\Delta_{false}/\Delta_{PNC} \approx .1 - .2$.

2. Imperfect Infrared Polarization. When the 7P → 8S rate equations were solved in Section F of Chapter II, we saw that both 323 nm signal size and the analyzing power depend on the quality of circular polarization at 2.18μ (see Figs. II.4 and II.5). Two consequences are

(a) The signal size and analyzing power will be different in Region 1 and Region 2.

(b) The signal size and analyzing power will be different for each helicity of ir light in each region.

As described in Chapter III, each region has its own crystalline quartz circular polarizer, which flips over about its $\hat{x}$ axis (horizontal, perpendicular to $\vec{k}_{ir}$) to reverse the light's polarization. The plates, although they were ground and polished simultaneously on the same lap, are not identical in thickness, and neither is a perfect 1/4 wave at 2.18μ. In addition, they do not flip over about an axis which bisects the fast and slow axes perfectly. To compensate for these unavoidable mechanical imperfections, we have installed individual linear polarizers in front of each 1/4 wave plate. While the experiment runs, the computer simultaneously calculates the following asymmetries:

$$\delta_{ir1} = \frac{S_1(ir+) - S_1(ir-)}{S_1(ir+) + S_1(ir-)} \qquad \text{(IV-50a)}$$

$$\delta_{ir2} = \frac{S_2(ir+) - S_2(ir-)}{S_2(ir+) + S_2(ir-)} \qquad \text{(IV-50b)}$$

where ir± refers to the ± helicity of the 2.18μ laser light, and subscripts 1 and 2 refer to region. By adjusting the rotational orientation of the linear polarizers with sensitive screw mechanisms, δ_{ir1} and δ_{ir2} can be made equal and both $\lesssim 10^{-3}$. Because the 7P-8S transition is heavily saturated with ir light, the asymmetry in the admixture of incorrect polarization when $\delta_{ir} = 10^{-3}$ is only $\sim 2 \times 10^{-5}$! This equalizes the analyzing power for ir+ and irin each region. The overall analyzing power will still be slightly different in the two regions. By direct measurement, the intensity ratio

$$\frac{I(\text{desired helicity})}{I(\text{unwanted helicity})} = \begin{cases} .001 & \text{in region 1,} \\ .0025 & \text{in region 2,} \end{cases} \tag{IV-51}$$

which is acceptable.

G. The Complete (0-1) Transition Amplitude

So far we have discussed the effects of electric and magnetic fields and poor polarization separately. However, some non-negligible systematics are only caused by two or more misalignments or stray fields acting in concert (an example already described is the $\eta\cos\delta$ effect which only couples to the parity violating channel through the M1). We will now write down the complete $6P_{1/2}F = 0 \rightarrow 7P_{1/2}F' = 1$ transition amplitude:

$$(0,0) \rightarrow (1,+1):\ A_{0,0}^{1,+1} =$$

$$\begin{aligned}
&\mp \frac{E_y\beta}{2}(1-\eta e^{i\delta}) \mp \frac{iE_x\beta}{2}(1-\eta e^{i\delta}) + \frac{iE_z\beta}{2}(1+\eta e^{i\delta}) \pm \frac{M}{2}(1-\eta e^{i\delta}) \\
&- \frac{i\mathcal{E}_p}{2}(1+\eta e^{i\delta}) - \theta_x \frac{E_x\beta}{2}(1+\eta e^{i\delta}) - i\theta_x \frac{M}{2}(1+\eta e^{i\delta}) \\
&- i\theta_y \frac{E_x\beta}{2}(1+\eta e^{i\delta}) + \frac{\theta_y M}{2}(1+\eta e^{i\delta}) \\
&\pm \frac{i\theta_z E_y\beta}{2}(1-\eta e^{i\delta}) \mp \frac{\theta_z E_x\beta}{2}(1-\eta e^{i\delta}) + \frac{\theta_z E_z\beta}{2}(1+\eta e^{i\delta}) \mp \frac{i\theta_z M}{2}(1-\eta e^{i\delta}) \\
&\pm \frac{E_y\beta}{2}\epsilon_z^6 + \frac{\alpha E_y}{2}(\epsilon_x^6 - \epsilon_x^7 - i\epsilon_y^6 + i\epsilon_y^7)
\end{aligned} \tag{IV-52a}$$

$(0,0)\rightarrow(1,0)$: $A^{1,0}_{0,0} =$

$$
\begin{aligned}
&-\frac{i}{\sqrt{2}}E_x\beta(1+\eta e^{i\delta}) + \frac{M}{\sqrt{2}}(1+\eta e^{i\delta}) \mp \frac{i\mathcal{E}_p}{\sqrt{2}}(1-\eta e^{i\delta}) \\
&\mp \frac{\Theta_x E_x}{\sqrt{2}}(1-\eta e^{i\delta}) \mp \frac{i\Theta_x M}{\sqrt{2}}(1-\eta e^{i\delta}) \\
&\pm \frac{\Theta_y E_y \beta}{\sqrt{2}}(1-\eta e^{i\delta}) - \frac{iE_z\beta\Theta_y M}{\sqrt{2}}(1+\eta e^{i\delta}) \\
&\pm E_y\beta\epsilon^6_x - \frac{E_y\alpha}{\sqrt{2}}(\epsilon^6_z - \epsilon^7_z)
\end{aligned}
\tag{IV-52b}
$$

$(0,0)\rightarrow(1,-1)$: $A^{1,-1}_{0,0} =$

$$
\begin{aligned}
&\pm \frac{E_y\beta}{2}(1-\eta e^{i\delta}) \mp \frac{iE_x\beta}{2}(1-\eta e^{i\delta}) - \frac{iE_z\beta}{2}(1+\eta e^{i\delta}) \pm \frac{M}{2}(1-\eta e^{i\delta}) \\
&- \frac{i\mathcal{E}_p}{2}(1+\eta e^{i\delta}) - \frac{\Theta_x E_x\beta}{2}(1+\eta e^{i\delta}) - \frac{i\Theta_x M}{2}(1+\eta e^{i\delta}) \\
&+ \frac{i\Theta_y E_x\beta}{2}(1+\eta e^{i\delta}) - \frac{\Theta_y M}{2}(1 + \eta e^{i\delta}) \\
&\pm \frac{i\Theta_z E_y\beta}{2}(1-\eta e^{i\delta}) \pm \frac{\Theta_z E_x\beta}{2}(1-\eta e^{i\delta}) + \frac{\Theta_z E_z\beta}{2}(1+\eta e^{i\epsilon}) \pm \frac{iM\Theta_z}{2}(1-\eta e^{i\delta}) \\
&\mp \frac{E_y\beta}{2}\epsilon^6_z + \frac{E_y\alpha}{2}(-\epsilon^6_x + \epsilon^7_x - i\epsilon^6_y + i\epsilon^7_y).
\end{aligned}
\tag{IV-52c}
$$

Here is the $6P_{1/2}F = 0 \rightarrow 7P_{1/2}F' = 0$ transition amplitude:

$$
A^{0,0}_{0,0} = \frac{E_y\alpha}{\sqrt{2}}(1+\eta e^{i\delta}) \pm \frac{iE_z\alpha}{\sqrt{2}}(1-\eta e^{i\delta}) \mp E_y\beta(\epsilon^6_x + \epsilon^7_x)\sqrt{2}
\tag{IV-52d}
$$

The following are notes on the expression for the 0-1 amplitude:

1. "±" signs refer to uv polarization. The bottom sign is for "$\hat{R}$" polarization = $\hat{\epsilon}_R + \eta e^{i\delta}\hat{\epsilon}_L$; the top sign is for $\hat{L} = \hat{\epsilon}_L + \eta' e^{i\delta'}\hat{\epsilon}_R$. Also, η and δ are to be read unprimed (primed) for $\hat{R}(\hat{L})$.

2. α and β are the reduced Stark matrix elements defined in Section C of Chapter II.

3. The coordinates are defined so that $\hat{k}_{uv}$ is along $\hat{x}$; $\hat{k}_{ir}$ lies in the $\hat{x}$-$\hat{z}$ plane, nominally along $\hat{z}$. $\vec{E}$ is mostly along $\hat{y}$.

4. E_x,E_y, and E_z and $\hat{x}$,$\hat{y}$, and $\hat{z}$ components of the static electric field. They each consist of two parts: $E_i = E_{oi} + \Delta E_i$, where E_{oi} reverses with the electric field and ΔE_i does not reverse.

5. θ_x,θ_y, and θ_z are slight rotation angles about $\hat{x}$,$\hat{y}$, and $\hat{z}$. They may be caused by misalignments, in which case θ_x and θ_z are redundant with E_z and E_x; or they may be caused by Hanle precession, in which case they obey the small angle formula $\theta_i \approx 0.036$ B_i (gauss), determined empirically (see Section E, part 2, Hanle Effect).

6. The terms involving ϵ come from hyperfine mixing:

$$\epsilon_i^6 = \frac{g_J \mu_o B_i}{2\sqrt{2}\, E_{6P\ hfs}} = -2.18\times 10^{-5} B_i(\text{gauss}) \qquad \text{(IV-53a)}$$

$$\epsilon_i^7 = \frac{g_J \mu_o B_i}{2\sqrt{2}\, E_{7P\ hfs}} = -2.18\times 10^{-4} B_i(\text{gauss}). \qquad \text{(IV-53b)}$$

7. Only those terms which are larger than $\mathcal{E}_p$, or first order in a misalignment, have been retained.

This equation looks quite forbidding. When you consider that the true parity violating amplitude is only one of 32 terms in the (0,0) → (1,+1) and (0,0) → (1,-1) transition amplitudes, you begin to appreciate the task of weeding out the systematics. Nonetheless, the parity violating signature is so distinctive, when one takes into account the region, infrared polarization, electric field, and uv polarization reversal, that almost every cross term in the expression for the polarization drops out. Which ones do not? There are some new terms of interest in addition to those which have been mentioned in the preceding sections.

To find the $7P_{1/2}$ polarization, we square the amplitudes $|A^{1,1}_{0,0}|^2$, $|A^{1,0}_{0,0}|^2$, $|A^{1,-1}_{0,0}|^2$, and $|A^{0,0}_{0,0}|^2$ and form the quantity

$$P = \frac{|A^{1,1}_{0,0}|^2 - |A^{1,-1}_{0,0}|^2}{|A^{1,1}_{0,0}|^2 + |A^{1,0}_{0,0}|^2 + |A^{1,-1}_{0,0}|^2 + F|A^{0,0}_{0,0}|^2} \qquad \text{(IV-54)}$$

We will retain terms to first order in θ_i and η, but second order in E_i and M. F, as defined in Section F, part 1, is the laser intensity $[I(\nu)]$ tuning ratio $I(0\text{-}0)/I(0\text{-}1)$, and we assume that F is $O(1/10)$. This is not difficult to compute, but it is a lot of writing; the answer is

$$P = \frac{-2M}{\beta E_y} \pm \frac{2i\mathcal{E}_p}{\beta E_y} \mp \frac{2E_xE_z}{E_y^2} \pm \frac{2\theta_xE_x}{E_y} \pm \frac{2\theta_yM^2}{\beta^2E_y^2} - \frac{2\theta_xE_zM}{\beta E_y^2}$$

$$\mp \eta \sin \delta \left[\frac{4\theta_xM}{\iota E_y} + \frac{4E_zM}{\beta E_y^2} - \frac{2\theta_zE_xE_z}{E_y^2} \mp \frac{2\theta_zE_z^2}{E_y^2}\right]$$

$$+ \eta \cos \delta \left[\frac{\pm 4\theta_xE_x}{E_y} \pm \frac{4\theta_yM^2}{\beta^2E_y^2} \mp \frac{4E_xE_z}{E_y^2} - \frac{4\theta_yE_x^2M}{E_y^2} - \frac{8E_z\theta_xM}{\beta E_y^2}\right]$$

$$\frac{2\alpha M}{\beta^2E_y}(\epsilon_x^6 - \epsilon_x^7) + \epsilon_z^6 + \frac{4MF(\alpha^2/\beta^2)\eta \cos \delta}{E_y\beta[1 + F(\alpha^2/\beta^2)]^2} \qquad \text{(IV-55)}$$

"±" refers to $\hat{L}$ or $\hat{R}$ polarization. The previous convention for η and δ is used here, i.e., read η, δ (η',δ') for the (top) bottom sign in a "±". All of the notes concerning Eq. (IV-52) also apply to this equation.

The polarization P may be conveniently divided into four categories, or "channels," according to the symmetry properties with respect to reversal of the electric field and laser polarizations:

1. Parity Channel. These polarizations change sign under all reversals—electric field, infrared helicity, uv helicity, and region 1 vs. region 2.

2. M1 Channel. These polarizations do not reverse when the ultraviolet helicity is changed. Otherwise, they are like the parity polarizations.

3. E Channel. These polarizations reverse with uv, region, and ir, but not with electric field reversals.

4. ir Channel. These polarizations only reverse with region and ir switches. This is the minimum requirement for an atomic polarization. Anything less is simply an intensity change due, for instance, to a change in the atomic alignment (quadrupole moment).

P splits in four pieces as follows. (We have omitted some of the negligibly small terms.):

Parity or P channel:

$$P_{PNC} = \frac{2i\mathcal{E}_P}{\beta E_{oy}} - \frac{2E_{ox}\Delta E_z}{E_{oy}^2} + \frac{4E_{ox}E_{oz}\Delta E_y}{E_{oy}^3} - \frac{2\Delta E_x}{E_{oy}}\left(\frac{E_{oz}}{E_{oy}} - \theta_x\right)$$

$$- 2(\eta \sin \delta + \eta' \sin \delta')\frac{M}{\beta E_{oy}}\left(\frac{E_{oz}}{E_{oy}} + \theta_x\right) \tag{IV-56}$$

$$- \frac{4E_{ox}M\theta_y(\eta \sin \delta + \eta' \sin \delta')}{\beta E_{oy}^2} - \frac{2\alpha M}{\beta^2 E_{oy}}(\varepsilon_x^6 - \varepsilon_x^7)$$

$$+ \frac{2MF(\alpha^2/\beta^2)(\eta \cos \delta - \eta' \cos \delta')}{E_{oy}\beta[1 + F(\alpha^2/\beta^2)]^2} + \frac{2\theta_x\Delta E_x}{E_{oy}}(\eta\cos\delta + \eta'\cos\delta') \quad ;$$

M1 channel:

$$P_{M1} = -\frac{2M}{\beta E_{oy}} + \frac{2\Delta E_x\theta_z}{E_{oy}} - \frac{2E_{ox}\Delta E_y\theta_z}{E_{oy}^2} + \frac{2MF(\alpha^2/\beta^2)(\eta \cos \delta + \eta' \cos \delta')}{E_{oy}\beta[1 + F(\alpha^2/\beta^2)]^2} \tag{IV-57}$$

$$+ 2\,\frac{\theta_x\Delta E_y}{E_{oy}}(\eta \cos \delta - \eta' \cos \delta') - \frac{2M}{\beta E_{oy}}\left(\frac{E_{oz}}{E_{oy}} + \theta_x\right)(\eta\sin\delta - \eta'\sin\delta') \quad ;$$

E channel:

$$P_E = -\frac{2E_{oz}E_{ox}}{E_y^2} - \frac{2\Delta E_z \Delta E_x}{E_y^2} + \frac{2\theta_x E_{ox}}{E_{oy}} - \frac{2\theta_x \Delta E_x \Delta E_y}{E_{oy}^2}$$

$$-\left[\frac{2\Delta E_z M}{\beta E_{oy}^2}\right](\eta \sin \delta + \eta' \sin \delta'); \tag{IV-58}$$

ir channel:

$$P_{ir} = \frac{2\theta_z E_z^2}{E_y^2}(\eta \sin \delta + \eta' \sin \delta') + \epsilon_z^6 \quad . \tag{IV-59}$$

In all channels except for parity, the first term in each expression dominates completely. In previous sections we have shown that the hyperfine mixing term $(\epsilon_x^6 - \epsilon_x^7)$ is negligible. We also showed that the η cos δ terms could be controlled so that they would not contribute. Under actual running conditions, all the terms with $\theta_{y,z}$ are likewise small, and so the terms that are left that might contribute to a false effect are:

$$\Delta_{\text{false}} = -\frac{2E_{ox}\Delta E_z}{E_{oy}^2} - \frac{2\Delta E_x}{E_{oy}}\left\{\frac{E_{oz}}{E_{oy}} - \theta_x\right\} + \frac{4E_{ox}\Delta E_y}{E_{oy}}\left\{\frac{E_{oz}}{E_{oy}} - \theta_x\right\}$$

$$-\frac{2M}{E_{oy}\beta}\left\{\frac{E_{oz}}{E_{oy}} + \theta_x\right\}[\eta \sin \delta + \eta' \sin \delta']. \tag{IV-60}$$

The first line contains three terms which all derive from the $E_x E_z / E_y^2$ term discussed in Section E, part 1. The last line has a new effect which is proportional to η sin δ, the <u>imaginary</u> part of the imperfect polarization.

H. Methods of Measuring and Eliminating Systematics Associated with Misaligned Electric Fields

We can independently measure E_{0x}, ΔE_x, E_{0z}, ΔE_z, ΔE_y, and η and δ. Our aim is to make the combined systematics less than one-fourth the size of the parity violation.

ΔE_y: The total signal for each electric field direction, summed over regions and laser polarizations is $S(E\pm) \approx E_{0y}^2 \pm 2E_yE_{0y}$. While running, we accumulate the asymmetry

$$\delta_E \equiv \frac{S(E_+) - S(E_-)}{S(E_+) + S(E_-)} = \frac{2\Delta E_y}{E_{0y}} \tag{IV-60}$$

Through a resistor network in the electric field pulser, we can change ΔE_y, and keep it less than $\sim 2 \times 10^{-3} E_{0y}$.

ΔE_z: This can be measured using linearly polarized light at 45 degrees with the $\hat{y}$ axis. Let $\varepsilon_\pm = (1/\sqrt{2})(\hat{y} \pm \hat{z})$. Then the Stark effect 0-1 transition amplitude may be written as

$$A(0\to1) = \beta \begin{bmatrix} \pm\frac{iE_y}{2} \mp \frac{E_x}{2} - \frac{iE_z}{2} \\ -\frac{E_x}{\sqrt{2}} \\ \mp\frac{iE_y}{2} \mp \frac{E_x}{2} + \frac{iE_z}{2} \end{bmatrix} \tag{IV-61a}$$

$$A(0\to0) = \frac{\alpha}{\sqrt{2}}[E_y \pm E_z] \tag{IV-61b}$$

Once again we are only interested in total signal, not polarization, so the smaller terms in the amplitude are insignificant in the sums. The signal size is

$$S_{01}(\tilde{\epsilon}_\pm) \propto \left[\frac{\beta^2 E_y^2}{2}\, 1 \mp 2\frac{E_z}{E_y}\right] \tag{IV-62a}$$

$$S_{00}(\tilde{\epsilon}_\pm) \propto \frac{\alpha^2 E_y^2}{2}\left[1 \pm 2\frac{E_z}{E_y}\right] \quad . \tag{IV-62b}$$

We form the asymmetry

$$[S(\tilde{\epsilon}_+) - S(\tilde{\epsilon}_-)]/[S(\tilde{\epsilon}_+) + S(\tilde{\epsilon}_-)] = -2E_z/E_y = -2(E_{oz} + \Delta E_z)/E_y \tag{IV-63}$$

The signal asymmetry which reverses with $\tilde{\epsilon}$, electric field, <u>and</u> hyperfine transition is $2\Delta E_z/E_y$. In principle we could also measure E_{oz}, by averaging over electric fields. In practice, the remaining two chops are insufficient to resolve the small signal cleanly.

$E_{ox}, \Delta E_x$: When a large magnetic field is imposed along $\hat{x}$, the terms involving θ_x become important. The dominant terms in the electric field channel for circularly polarized uv are:

$$-\frac{2E_{ox}}{E_{oy}}\left[\frac{E_{oz}}{E_{oy}} - \theta_x\right] \, . \tag{IV-64}$$

To measure this, we installed magnetic field coils coaxial with the uv beam inside the vacuum can. These are capable of producing up to eight gauss. A plot of the electric field channel vs. B_x is shown in Fig. IV.6 (a). The data points were measured using the new cell with internal electrodes. The slope of the line yields $E_{ox}/E_{oy} = -4 \times 10^{-4}$. The parity channel in the same experiment has a polarization

$$P \approx \frac{2\Delta E_x \theta_x}{E_{oy}} + (\text{terms independent of } \theta_x), \qquad \text{(IV-65)}$$

and this has been used to determine $\Delta E_x/E_{oy} = 6 \times 10^{-4}$ [data shown in Fig. IV.6 (b)].

$\eta \sin \delta$: Using the same method shown above, we also measure $\eta \sin \delta + \eta' \sin \delta'$, the imaginary part of the imperfect polarization in Eq. (IV-60). When the uv mirror is blocked, the M1 polarization assumes its full value. We then have an additional θ_x dependent term in the P channel:

$$P \approx \theta_x \left[\frac{2\Delta E_x}{E_{oy}} - \frac{2M}{\beta E_{oy}} (\eta \sin \delta + \eta' \sin \delta') \right] \quad . \qquad \text{(IV-66)}$$

We may extract the $\eta \sin \delta$ effect from the parity channel by imposing a large magnetic field B_x and comparing mirror blocked data to mirror unblocked data. In practice, we reverse B_x between ±5 gauss, which corresponds to $\theta_x = \pm.18$. Subtracting $P(\theta_x = +.18) - P(\theta_x = -.18)$ eliminates θ_x independent terms. Simultaneously, the M1 channel

Figure IV.6 Measurement of polarization induced by a large magnetic field along x.

(a) P channel vs. B_x, fit to $(-2\Delta E_x/E_{oy})(E_{oz}/E_{oy} - \theta_x)$.

(b) E channel vs. B_x, fit to $(-2E_{ox}/E_{oy}(E_{oz}/E_{oy} - \theta_x)$.

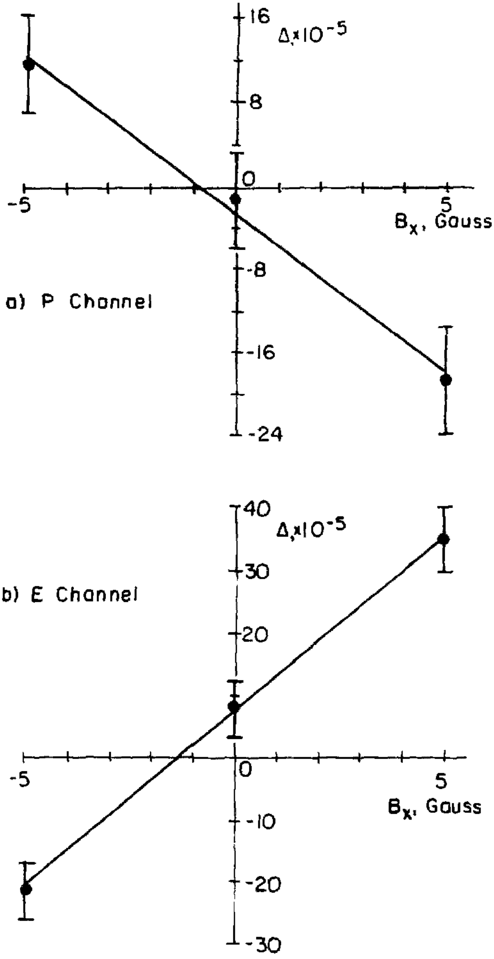

XBL 807-5588

Fig. IV.6

records $-2M/(\beta E_{oy})$ for blocked and unblocked data, and this is used to eliminate the ΔE_x term in Eq. (IV-66).

Once the quantity $\eta \sin \delta + \eta' \sin \delta'$ has been measured, the data may be corrected. Generally, $(\eta \sin \delta + \eta' \sin \delta') \sim .1$, and the correction is of order 2×10^{-6} for the unblocked data and 8×10^{-6} for blocked data. The correction contains an uncertainty due to the fact that the forward and reversed beams do not have the same $\eta \sin \delta$. Birefringence in the back surfaced mirror and the cell window will change the polarization. We know that this effect is small from our monitor of $\eta \cos \delta$, from which we estimate a difference of $5\text{-}15 \times 10^{-3}$ between blocked and unblocked $\eta \sin \delta$.

E_{oz}: Returning now to the experiment with linearly polarized uv at 45°, we can get more information by using the atomic polarization channels. The total 0-1 and 0-0 amplitudes may be found by substituting 1 for $1+\eta e^{i\delta}$, and i for $1-\eta e^{i\delta}$ into Eq. (IV-52). The atomic polarization is

$$P \approx \mp \frac{2M}{\beta E_{oy}}\left[\theta_x + \frac{E_{oz}}{E_{oy}}\right] \quad \Big\} \text{ P channel} \qquad \text{(IV-66a)}$$

$$\pm \frac{2\theta_x M \Delta E_y}{\beta E_{oy}^2} \mp \frac{2M\Delta E_z}{\beta E_{oy}^2} \quad \Big\} \text{ E channel} \qquad \text{(IV-66b)}$$

$$- \frac{2M}{\beta E_{oy}}\,, \quad \Big\} \text{ M1 channel} \qquad \text{(IV-66c)}$$

where only the most significant terms have been retained. "±" signs now refer to switching between $\hat{\varepsilon}_\pm = (1/\sqrt{2})(\hat{\varepsilon}_y \pm \hat{\varepsilon}_z)$. The second term in the P channel is the "$\eta \sin \delta$" polarization described earlier; now $\eta \sin \delta = 1$.

Figure IV.7 shows data taken in the P channel with the 45° polarization, as a function of B_x. The θ_x term shows up clearly as a Hanle precession. The intercept misses the origin due to the E_{0z} term. By tuning the magnetic field, we can cancel out the asymmetry with a field of .25 Gauss. During our actual run we cannot use B_x to cancel the effect of E_{0z} in the $\eta \sin \delta$ effect. Although this effect is proportional to $(E_{0z}/E_{0y} + \theta_x)$, there is another false parity term, caused by E_x, which is proportional to $(E_{0z}/E_{0y} - \theta_x)$ [see Eq. (IV-56)]. We cannot make one better without making the other worse.

I. Scalar Invariants

In our search for systematic errors in this experiment, we have occasionally been assisted by the use of scalar invariants. All false parity violating signals must be proportional to scalar quantities. Only the true parity violation is pseudoscalar. Furthermore, those effects which do not depend on the unstable nature of the 7P or 8S states must be even under time reversal (T-even). A notable exception is the Hanle effect, which only occurs because the 7P state decays a short time after it is created. Hanle scalars are therefore T-odd. Table IV-2 lists the scalar and pseudo-scalar quantities of interest in this experiment. They are all made up of the physical observables

Figure IV.7 P channel polarization for $\eta \sin \delta = 1$ experiment. The curve is the Hanle effect prediction for $\Delta_M = 6.8 \times 10^{-3}$, with a zero offset of 9×10^{-5}. ($\Delta_M = -2M/\beta E_y$).

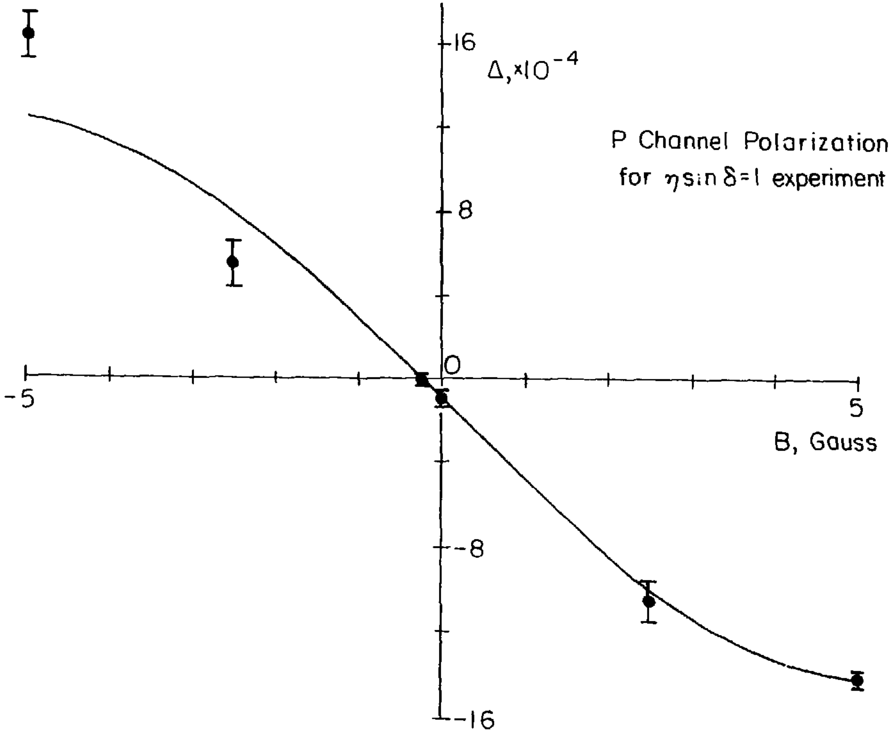

XBL 807-5589

Fig. IV.7

Table IV.2. Scalar and pseudoscalar invariants.

Quantity	Effect	Symmetry	
		P	T
$\vec{h}\,\vec{k}_{uv}\times\vec{E}\cdot\vec{J}$	Parity violation	-1	+1
$(\hat{\epsilon}_{uv}+\hat{\epsilon}^{*}_{uv})\,\vec{E}\,\vec{k}_{uv}\times\vec{J}\cdot(\hat{\epsilon}_{uv}+\hat{\epsilon}^{*}_{uv})$	M1 (α)	+1	+1
$(\hat{\epsilon}_{uv}-\hat{\epsilon}^{*}_{uv})\cdot\vec{J}\,\vec{k}_{uv}\times\vec{E}\cdot(\hat{\epsilon}_{uv}-\hat{\epsilon}^{*}_{uv})$	M1 (β)	+1	+1
$h\,\vec{k}_{uv}\cdot\vec{E}\,\vec{J}\cdot\vec{E}$	$(E_xE_z)/E_y^2$	+1	+1
$h\,\vec{k}_{uv}\cdot\vec{E}\,\vec{J}\times\vec{B}\cdot\vec{E}$	$(E_x/E_y)\theta_x$ (Hanle effect)	+1	-1
$(\hat{\epsilon}_{uv}-\hat{\epsilon}^{*}_{uv})\cdot\vec{E}\,\vec{k}_{uv}\times\vec{J}\cdot(\hat{\epsilon}_{uv}-\hat{\epsilon}^{*}_{uv})$	$\eta\sin\delta\,ME_z$	+1	+1
$(\hat{\epsilon}_{uv}-\hat{\epsilon}^{*}_{uv})\cdot\vec{E}\,\vec{k}_{uv}\times(\vec{J}\times\vec{B})\cdot(\hat{\epsilon}_{uv}-\hat{\epsilon}^{*}_{uv})$	$\eta\sin\delta\,M\theta_x$ (Hanle effect)	+1	-1

in the thallium system: $\hat{\varepsilon}_{uv}$, $\vec{k}_{uv}$, $\vec{E}$, $\vec{B}$, and $\vec{J}$. $\hat{\varepsilon}_{uv}$ is the polarization, and not a true vector since its head and tail are not well defined, and it can be complex. Therefore, $\hat{\varepsilon}_{uv}$ always enters an expression an even number of times. $\vec{J}$ is the polarization vector of the 7P state in thallium. In our experiment the ir photon's angular momentum analyzes J_z. In the anticollinear experiment, the ir analyzes J_x. The polar vectors are $\hat{\varepsilon}_{uv}$, $\vec{k}_{uv}$, and $\vec{E}$. Axial vectors are $\vec{B}$ and $\vec{J}$. Finally, $h = (\hat{\varepsilon}_{uv} x \hat{\varepsilon}_{uv}{}^{*}) \cdot \vec{k}_{uv} / |k_{uv}|$, the uv helicity.

CHAPTER V: DATA

The data consist of runs obtained during the period January through June 1980. Although the combined statistical uncertainty is quite small (approximately 4 standard deviations), we do not feel that the systematic errors are small enough to claim this precision for the measurement. These data must therefore be considered preliminary. Work continues on the high precision measurement.

A. Data Analysis

An offline analysis program, run on the LSI 11/2 computer between experimental runs, summarizes the data stored on floppy disks, and computes average asymmetries. An example of output from this program is shown in Fig. V.1. We compute asymmetries for each of our experimental configurations, as described in Section A of Chapter IV: uv mirror unblocked; uv mirror blocked; background, mirror unblocked; background, mirror blocked; and the same four, but on the (0-0) resonance. The two in Fig. V.1 are (0-1), unblocked and blocked.

The line which is labeled "total" contains the M1 and parity violating asymmetries Δ_M and Δ_P, along with σ based on 256 laser pulses. "N" above this line is the number of 256-shot sets in the run. The standard error is $\sigma/\sqrt{N}$. The rest of the lines contain Δ_M and Δ_P for only a selected fraction of the data, as indicated (e.g., "E+" only contains data with one polarity of electric field). Note that σ is generally $\sqrt{2}$ larger for these, except when the regions are not subtracted. In that case, σ reflects the laser pulse-to-pulse jitter.

```
  1866      9
N=7464       M-1        SIGMA          P         SIGMA
TOTAL     0.0018172  0.0008958  0.0000153  0.0007570
REG 1     0.0019880  0.0143000 -0.0001296  0.0075888
REG 2     0.0016430  0.0147206  0.0001584  0.0076773
E+        0.0020292  0.0024267  0.0000638  0.0010687
E-        0.0016052  0.0025149 -0.0000333  0.0010761
IR+       0.0018897  0.0012673  0.0000082  0.0010668
IR-       0.0017446  0.0013064  0.0000223  0.0010818
UV+       0.0018324  0.0011820
UV-       0.0018019  0.0011635
DELTAS   -0.0001661  0.0084014 -0.0001327  0.0086282
SIGNAL SIZES
              UV+E+      UV-E+      UV+E-      UV-E-
REG1,IR-    4116.55    4118.09    4133.33    4137.25
REG1,IR+    4137.12    4138.29    4123.74    4122.95
REG2,IR-    4139.41    4139.86    4127.59    4131.21
REG2,IR+    4125.76    4128.06    4143.60    4143.73
UV+ INTENSITY=  32735.34  UV- INTENSITY=  32735.37
  1103      10
N=4412       M-1        SIGMA          P         SIGMA
TOTAL     0.0068183  0.0011650  0.0000106  0.0009480
REG 1     0.0076207  0.0151036  0.0000198  0.0078928
REG 2     0.0060178  0.0150886  0.0000024  0.0078339
E+        0.0071839  0.0026032  0.0000392  0.0013348
E-        0.0064527  0.0029806 -0.0000180  0.0013740
IR+       0.0068883  0.0014627  0.0000355  0.0013327
IR-       0.0067483  0.0016050 -0.0000144  0.0013760
UV+       0.0068289  0.0015044
UV-       0.0068077  0.0014995
DELTAS   -0.0000233  0.0088690  0.0001600  0.0086209
SIGNAL SIZES
              UV+E+      UV-E+      UV+E-      UV-E-
REG1,IR-    2438.41    2439.05    2479.16    2480.24
REG1,IR+    2481.23    2479.69    2446.77    2446.41
REG2,IR-    2571.06    2570.74    2545.52    2545.45
REG2,IR+    2541.93    2540.09    2577.44    2576.12
UV+ INTENSITY=  32738.67  UV- INTENSITY=  32738.69
```

Fig. V.1. Offline analysis program output. For explanation, see text.

The line which begins "Deltas" contains the average for δ_{uv}, defined in Section F of Chapter IV. As explained there, this is used during a run to maintain the purity of uv polarization in the cell.

Below this is a 4x4 matrix which gives the average digitized signal size for each configuration. This information is equivalent to the lines above, but not identical, because the region subtraction, which is made after 256 shots in the calculated asymmetries, cannot be reconstructed from the matrix, which has averaged each region over the whole run.

B. Data Summary

Based on the information in this summary, necessary corrections are applied to the data.

1. M1 normalization (all data normalized to an M1 asymmetry of 5.5×10^{-3}.)
2. Hunter correction (see Chapter IV).
3. $\eta \cos \delta$ effect (usually negligible).

In addition, systematic corrections can be made by using these summaries in conjunction with the auxiliary experiments detailed in Chapter IV.

Several changes were made in the apparatus during this period. During part of the time we used the fixed quarter wave plate, and equal amounts of data are listed for the "uv+" and "uv-" positions. Sometimes a Pockels cell half wave plate was inserted before the polarizer. The last runs had a Pockels cell quarter wave retarder. Also, most of the time we used electrodes outside the cell, but the last runs used a new cell with internal electrodes. The data are tabulated in Table V-1.

Table V-1. Data

RUN		E(V)	Δ_M	Δ_p(uncorr)	Δ_H	Δ_p(corr)	Δ_p(norm)	ESE
122-140	UV+	200	70200	+ 66 ± 88	+ 46	+ 20 ± 88	+ 16 ± 69	50
141-165	UV-	200	64800	+232 ± 71	- 26	+258 ± 71	+219 ± 60	50
167-177	UV-	200	62200	+177 ± 109	+116	+ 61 ± 109	+ 54 ± 96	50
178-196	UV+	200	62900	+ 55 ± 84	+331	+386 ± 84	+337 ± 73	50
197-209	UV+	400	42023	+287 ± 76	+ 78	+207 ± 76	+271 ± 99	100
210-225	UV-	400	41000	+389 ± 78	+146	+243 ± 78	+326 ± 105	100
226-233	PUV-	400	39500	-197 ± 104	- 95	-102 ± 104	-142 ± 145	200
241-251	PUV+	200	56071	+181 ± 149	- 76	+257 ± 149	+252 ± 146	200
257-261	PUV-	400	39700	-381 ± 133	- 6	-375 ± 133	-520 ± 184	>200
263-278	P+	400	40100	- 10 ± 100	+ 66	- 76 ± 100	-105 ± 137	100
279-338	P+	300	48900	+ 90 ± 45	+ 42	+ 48 ± 45	+ 54 ± 51	100
355-390	P+	200	68200	+153 ± 88	+ 17	+136 ± 88	+109 ± 71	10
396-413	P+	200	70400	- 90 ± 116	+(50±2[illegible]	- 31 ± 119	- 24 ± 93	10
414-430	P+	200	69000	199 ± 137	-(20±39)	179 ± 143	143 ± 114	10

NOTES: UV± refers to orientations of the rotating quarter wave plate. Runs with PUV± have a half wave plate inserted in front of the quarter wave plate, and P+ uses a Pockels cell quarter wave plate. All signs of Δ_p have been adjusted so that +1 helicity light produced by the retardation plate is added, and -1 helicity light is subtracted. Asymmetries and errors are in units of 10^{-7}. ESE is the estimated systematic error. Starting with run 355, Δ_H includes the Hunter correction as well as corrections due to $n \sin \delta$, $n \cos \delta$, and stray electric fields E_x and E_z, as described in Chapter IV.

Our early running (January through March) was done with a succession of quartz spectrophotometer cells with external nickel electrodes. At this time we still took equal amounts of data on the 0-1 and 0-0 lines as a safeguard against the $\eta \cos \delta$ effect. We used the rotating crystalline quartz quarter wave plate, which was reversed periodically by rotating it about the vertical axis perpendicular to the uv beam. Careful subsequent analysis reveals that the earlier 200V (150 V/cm) data show minimal signs of systematic frequency jitter as described in Chapter IV. However, this systematic error increased dramatically during February's 400 V (300 V/cm) data, and runs 226-261 are completely dominated by this effect. The total amount of data to this point is about 1.5×10^7 laser shots. If the unaffected data are taken alone (runs 122-209), the asymmetry $\Delta_p = (182 \pm 61) \times 10^{-7}$ is consistent with our previously published result of $(170 \pm 70) \times 10^{-7}$. Unfortunately, stray electric fields associated with the new geometry may have created systematic errors which prevent us from claiming that the experimental agreement is significant. It is noteworthy that the (0-0) data during these runs averages $-(35 \pm 32) \times 10^{-7}$, showing that the $\eta \cos \delta$ effect was absent. As explained in Chapter IV, (0-0) data is free of the other systematic errors.

We have already described our change over to a Pockels cell, which eliminated the frequency jitter systematic errors. Pockels cell data continued, using the same type of cell as before. As we continued to run, we noticed that the electric field channel was consistently

2×10^{-4}, many standard deviations from zero. As we have discussed extensively in Chapter IV, this was caused by the presence of large (~1 V/cm) electric fields in the $\hat{z}$ and/or $\hat{x}$ direction. Some fraction of these fields did not reverse with the voltage on the electrodes, and this caused false effects on the order of 5-10 x 10^{-6}.

Runs 279-430 in the table are data taken with a new cell with internal electrodes. This cell showed great promise, and has proven to be our best design. The runs were cut short, however, by the sudden appearance of large electric field dependent backgrounds. These have since been traced to contaminated electrode surfaces, and we believe the problem has been eliminated.

We have continued to run with this cell or a new design with external electrodes, and we hope to achieve a 25 percent measurement in the near future. The most recent runs look encouraging. The systematic errors are now under control.

C. Future Work

Beyond our current plans to make a four sigma measurement of $\mathcal{E}_p$, two projects remain. First, we would like to measure some of the $7P_{1/2}$ → nP and $7P_{1/2}$ → nS oscillator strengths, so that the errors in the parity violation and magnetic dipole asymmetry calculations will not be limited by our knowledge of the Stark effect. The $7P_{1/2}$ → 7S rate is measured by the Hanle effect. The 6D → 7P rates can be measured by observing the intensity ratios of 6D fluorescence lines and comparing them to the known 6D → 6P rates. These are the two most important dipole matrix elements involving the $7P_{1/2}$ state, which are used in the Stark effect calculation.

The second project is a much higher resolution experiment in the $6P_{1/2} \rightarrow 7P_{1/2}$ transition. Persis Drell is working on a linear polarization experiment. A static electric field is set up parallel to the 293 nm laser beam. The amplitudes for transitions to each of the components in the (0-1) and (0-0) lines are:

$$(7P_{1/2}F=1) = \begin{pmatrix} \cos\phi\left(\frac{i\beta+M}{2}\right) + \frac{\mathcal{E}_p}{2}\sin\phi \\ \sin\phi\,(i\beta+M) - \mathcal{E}_p\cos\phi \\ -\cos\phi\left(\frac{i\beta+M}{2}\right) - \frac{\mathcal{E}_p}{2}\sin\phi \end{pmatrix}$$

$$(7P_{1/2}F=0) = 0.$$

The polarization angle ϕ is defined in Fig. V.2. Note that now the Stark and M1 amplitudes are relatively imaginary so that there is no M1 interference. There is also no polarization of the $7P_{1/2}$ state. However, if a static B field is imposed along $\hat{z}$ perpendicular to $\vec{E}$ and $\vec{k}$, a Zeeman splitting will result. If the splitting is large enough, the laser can be tuned to excite the $0 \rightarrow (1,-1)$ transition only. Now a reversal of the sign of the electric field will give rise to an intensity asymmetry of

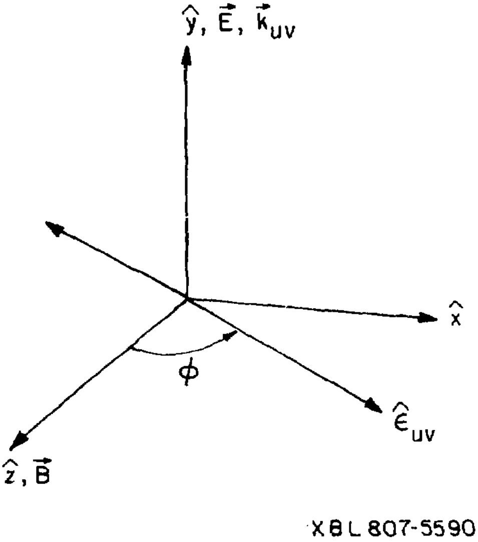

Figure V.2 Coordinate system for a linear polarization experiment. The electric field is along the laser beam axis.

$$\Delta_p = \frac{i\mathcal{E}_p \sin \phi}{\beta \cos \phi}$$

(see Fig. V.3). This can be observed as an asymmetry in the fluorescence at 535 nm. The parity violation is proportional to the pseudoscalar $(\hat{\varepsilon}+\hat{\varepsilon}^*)\cdot\vec{B}\ (\hat{\varepsilon}+\hat{\varepsilon}^*)\times\vec{B}\cdot\vec{E}$.

This experiment is subject to a different set of systematic errors than the present one, and this fact alone makes it worthwhile. However, it also has several other advantages. Since no second transition is needed, the fluorescent intensity will be an order of magnitude higher. Since there is no OPO or beam overlap, σ should be limited only by counting statistics. In addition, a Nd:YAG pumped frequency doubled dye laser (Drell and Chu 1979) which is 5-10 times more powerful than our flashlamp pumped lasers will be used to generate 292.7 nm light. It is conceivable that 1σ counting times might be reduced to about two hours of running time.

Figure V.3 Zeeman effect in $7P_{\frac{1}{2}}$ Tl^{205}, showing the $6P_{\frac{1}{2}} \rightarrow 7P_{\frac{1}{2}}$ lineshape as a function of magnetic field, for two linear polarizations. The point where the parity violating interference described in the text is largest occurs at 3.2 kilogauss, at the frequency indicated.

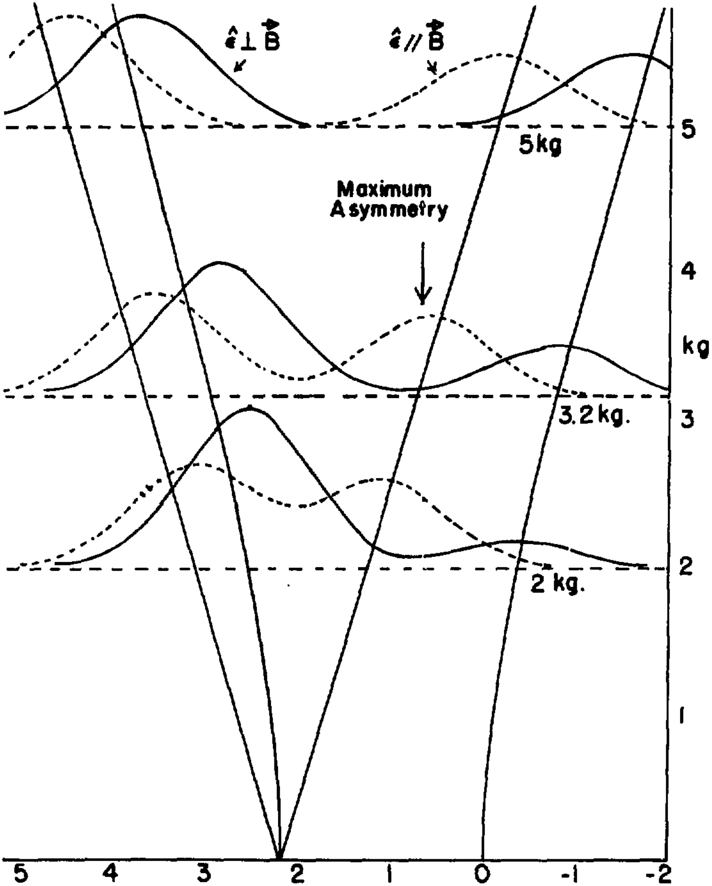

XBL 807-10679

Fig. V.3

APPENDIX A: COMPUTER PROGRAMS

1. OPO Selective Excitation. The rate equations (II-18a) through (II-18h) were solved as functions of uv tuning, ir intensity, and ir polarization, using a simple computer program which inverts a square matrix. The program follows:

```
C  OPO SOLVES THE 7P-8S RATE EQUATIONS FOR OPO OPTICAL PUMPING.
C A0 IS THE 7P-7S RATE
C A  IS THE 8S TOTAL RATEC
C A1 IS THE 8S-6P1/2 PARTIAL RATE
C K  IS (1/3)8S-7P RATE
      REAL K,L
      A0=2.14
      A =4.36
      A1=.45
      K =.119
C  WHEN B=1.083, THE INHOMOGENEOUS LINEWIDTH IS 1.6 GHZ.
      B=1.083
C   FREQ IS IN GHZ . 0 IS AT 0-1 LINE IN TL205, AND THE 00 LINE
C   IS HIGHER IN 'FREQ' (ALTHOUGH NOT IN FREQUENCY).
      FREQ=0.
C   R IS IN UNITS OF 10**7 (SEC)-1.
      R=10.
      X=.01
      PRINT*, '   FREQUENCY      OPO POWER      ANALYZING     SIGNAL SIZ
     1E  RATIO OF LINES'
  1   CONTINUE
      TYPE*, '   INPUT FREQ., OPO POWER, POL. RATIO (END=-100)'
      ACCEPT*,FREQ,P,X
      IF (FREQ.EQ.-100.) GO TO 7
      ILEFT=0
      R=P/(1+X)
      L=X*R
      S00=1.44*.7*EXP(-B*(FREQ-2.13)**2)
     1+.432*EXP(-B*(FREQ-3.396)**2)
      S01=(.7)*EXP(-(B*FREQ**2))+(.3)*EXP(-B*(FREQ-1.266)**2)
C   S01 IS THE TOTAL STARK TRANSITION. S11 GOES TO (1,1) AND
C   S1M1 GOES TO (1,-1).
      S11=S01/2.+.005*S01/2.
      S1M1=.995*S01/2.
  5   CONTINUE
      F11=A+2.*R-A1/4.-(R*2.*(K+R))/(A0+R+L)
      F12=-R*2.*K/(A0+R+L)-A1/2.
      F13=-(2.*R*(K+L))/(A0+R+L)-A1/4.
      F21=-(K*L)/(A0+2.*L)-A1/4.
      F22=A-(R*2.*(K+R))/(A0+2.*R)-(2.*L*(K+L))/(A0+2.*L)-A1/2.
     1+R+L
      F23=-R*K/(A0+2.*R)-A1/4.
      F31=-L*2.*(K+R)/(A0+R+L)-A1/4.
      F32=-L*2.*K/(A0+R+L)-A1/2.
      F33=-L*2.*(K+L)/(A0+R+L)-A1/4.+2.*L+A
C NOW CALCULATE THE DETERMINANT
      DETF=F11*(F22*F33-F23*F32)+F12*(F23*F31-F21*F33)+
```

```
     1F13*(F21*F32-F22*F31)
C THIS IS THE INVERSE MATRIX.
      G11=(F22*F33-F32*F23)/DETF
      G12=(F13*F32-F12*F33)/DETF
      G13=(F12*F23-F13*F22)/DETF
      G21=(F23*F31-F21*F33)/DETF
      G22=(F11*F33-F13*F31)/DETF
      G23=(F13*F21-F11*F23)/DETF
      G31=(F21*F32-F22*F31)/DETF
      G32=(F12*F31-F11*F32)/DETF
      G33=(F11*F22-F21*F12)/DETF
C
      C1=R*S00/(A0+R+L)
      C2=R*S1M1/(A0+2.*R)+L*S11/(A0+2.*L)
      C3=L*S00/(A0+R+L)
      IF(ILEFT.EQ.1) GO TO 6
      ILEFT=1
      SIGR=C1*(G11+2.*G21+G31)+C2*(G12+2.*G22+G32)+C3*(G13+2.*G23+G33)
      L=R
      R=X*L
      GO TO 5
  6   R=L
      L=X*R
      SIGL=C1*(G11+2.*G21+G31)+C2*(G12+2.*G22+G32)+C3*(G13+2.*G23+G33)
      EFF=((SIGL-SIGR)/(SIGR+SIGL))*((S00+S11+S1M1)/(S11-S1M1))
      RATIO=(C2*(G12+2.*G22+G32))/
     1(C1*(G11+2.*G21+G31)+C3*(G13+2.*G23+G33))
      TYPE*, 'ANALYZING POWER IS ',EFF
      TYPE*, 'SIGNAL SIZE IS     ',SIGR
      TYPE*, 'RATIO OF LINES IS  ',RATIO
      PRINT*,FREQ,P,EFF,SIGR,RATIO
      GO TO 1
  7   CONTINUE
      END
```

2. Running Program. As the modifications discussed in Chapters III and IV were implemented, the running program evolved in sophistication. The current version, written in Fortran IV with a data collection subprogram in Macro, performs the following functions:

1. Collects data
2. Performs calculations of asymmetries
3. Records data summaries on floppy disks
4. Controls field and polarization switching
5. Determines when background data is taken, and controls this function
6. Controls blocking of the uv mirror
7. Monitors uv frequency and tunes uv laser.

```
C       PARITY .018 IS THE SAME AS PARITY.017 EXCEPT THE 12 BIT ADC IS USED
C       THE UV IS NOW SWITCHED FROM THE COMPUTER WITH A POCKEL CELL
C       TO THE RHYTHM OF THE DELHI KAIDA
C       THE MONITOR CELL BACKGROUND IS SUBTRACTED DIGITALLY
C       THE ELECTRIC FIELD IS CONTROLLED BY THE BOX
C       AND THE UV HAS AN ADDITIONAL RANDOMIZATION
C        FIRST ACCEPT INITIAL PARAMETERS FROM THE TELETYPE
        COMMON SS,N,NIR,SB,NB
        COMMON /BLK1/AUV,AES,D,T,S,IRS
        COMMON /BLK2/MSR,MSR,NPR1,NPRO
        OPEN (UNIT=6,BUFFERCOUNT=2)
        CALL ASSIGN(12,'DX1:FILE.000',-1,'NEW')
        CALL START
        TYPE *, ' NUMBER OF IR SWITCHES/PRINTOUT'
        PRINT *,  ' NUMBER OF IR SWITCHES/PRINTOUT'
        ACCEPT*,NIR
        PRINT*,NIR
        SR=MSR
C  INITIALIZE CONSTANTS
        LOGICAL*1 I,IK
        DIMENSION  D(8), T(8)
        DIMENSION ISTAT(8), DATAS(8,11), DATA(12), JDATA(6)
        DIMENSION SDATA(12), S(14), SS(14), TS(14), SB(6), TB(6)
        IK=7
        IRAN=0
        JRAN=0
        M1STAT=0
        N3=0
        IREQB="100000
        IOUT2="167762
        ICSR="167770
        IOUTBF="167772
        INBUF="167774
        IE="100000
        IR="20000
        LIN="10000
        IUVN=1
        IUV=2
        IUVSW=2
        ITWEAK=1
        ITUNE=16
        JRAT=0
        JTUNE="100000
        MO=1
        I='W'
C  STATEMENT 100 INITIALIZES THE LARGE PRINTOUT SUMS
        IP=1
```

```
        ICONT2=IP+IUVSW
        CALL IPOKE(IOUT2,ICONT2)
        CALL IPOKE("176770,0)
100     M=0
        MB=0
        DO 112 K=1,6
112     SB(K)=0
        IT=0
        DO 110 K=1,14
110     SS(K)=0
        ISTROB=1+JTUNE+M15TAT
        CALL IPOKE(IOUTBF,ISTROB)
        JDATA(6)=IPEEK(INBUF)
        LINST=JDATA(6).AND.LIN
        IF(LINST.NE.LIN) GO TO 120
        LINS=1
        WRITE(6,*) ' LINE IS 0-1'
        TYPE *, ' LINE IS 0-1'
        NPR=NPR1
        LSS=IUV
        GO TO 130
120     LINS=-1
        WRITE(6,*) ' LINE IS 0-0'
        TYPE *, ' LINE IS 0-0'
        NPR=NPR0
        LSS=LINST
130     I='W'
        GO TO 202
C  STATEMENT 200 IS THE RETURN POINT AFTER COMPLETING A PRINTOUT
200     CONTINUE
        IF(M.EQ.5) GO TO 315
        IF(M.EQ.15) GO TO 315
        IF(((M/2)*2-M).EQ.0) GO TO 319
202     IF (M.LT.NPR) GO TO 320
        I='X'
        GO TO 314
C  STATEMENT 304 IS THE BRANCH POINT FOR TT INTERUPT OPTIONS
304     CONTINUE
        ACCEPT 900,I
        IF(I.EQ.'E') GO TO 999
        IF(I.EQ.'W') GO TO 320
        IF(I.EQ.'C') GO TO 320
        IF(I.EQ.'T') GO TO 320
        IF(I.EQ.'B') GO TO 310
        IF(I.EQ.'P') GO TO 314
        IF(I.EQ.'L') GO TO 100
        IF(I.EQ.'R') GO TO 316
```

```
        IF(I.EQ.'A') GO TO 317
        IF(I.EQ.'M') GO TO 319
        IF(I.EQ.'H') GO TO 315
306     IT=0
        M1STAT=0
        IP=1
        ICONT2=1+IUVSW
        CALL IPOKE(IOUT2,ICONT2)
        GO TO 318
C  STATEMENT 310 IS THE BACKSPACE OPTION
310     CONTINUE
        IF(M.EQ.0) GO TO 318
        BACKSPACE 12
        MO=MO-1
        IF(KT.EQ."100000) GO TO 317
        IF(KT.EQ."40000) GO TO 311
        IF(KT.EQ."140000) GO TO 315
        M=M-1
        DO 312 K=1,14
312     SS(K)=SS(K)-TS(K)
        IF(IT.NE.0) GO TO 306
        GO TO 318
311     DO 313 K=1,6
313     SB(K)=SB(K)-TB(K)
        MB=MB-1
        GO TO 319
C  STATEMENT 314 IS THE LONG PRINTOUT OPTION
314     IF (M.LT.2) GO TO 318
        CALL LONGPR
        IF(I.NE.'X') GO TO 318
        TYPE*, ' CHANGE LINES'
C  STATEMENT 316 RESETS THE PZT.
316     JTUNE="100000
        ITUNE=16
        JRAT=0
        NC=JTUNE+M1STAT
        CALL IPOKE(IOUTBF,NC)
        TYPE 901,IK
        TYPE*,'PZT HAS BEEN RESET. PLEASE RETUNE LASER 1'
        GO TO 318
C       STATEMENT 315 IS THE BLOCKED BACKGROUND OPTION
315     IP=0
        ICONT2=IUVSW
        CALL IPOKE(IOUT2,ICONT2)
        IT="140000
        GO TO 703
317     IP=0
```

```
        ICONT2=IUVSW
        CALL IPOKE(IOUT2,ICONT2)
        DO 701 K=1,100
701     CONTINUE
        IT='100000
        GO TO 320
C       STATEMENT 318 IS THE WAIT OPTION
318     I='W'
        GO TO 320
C  STATEMENT 319 IS THE M-1 OPTION
319     IT='40000
703     M1STAT='400
        NC=M1STAT+JTUNE
        CALL IPOKE(IOUTBF,NC)
        DO 700 K=1,30000
700     CONTINUE
C       STATEMENT 320 IS THE CONTINUE OPTION
320     CONTINUE
        IRST=1
        DO 322 K=1,14
322     S(K)=0
        SCH4=0
        SCH5=0
C  NOW BEGIN THE IR LOOP
        DO 500 N1=1,NIR
        IESTO=1
C  NOW UPDATE IOUTBF VALUES
        NC=JTUNE+M1STAT
        IRSWIT='200+JTUNE+M1STAT
        ISTROB=NC+1
C GET IR STATUS HERE AND WAIT FOR THE CHANGE
324     CONTINUE
        CALL IPOKE(IOUTBF,ISTROB)
        JDATA(6)=IPEEK(INBUF)
        IRSTO=JDATA(6).AND.IR
        IF(IRSTO.NE.IRST) GO TO 330
        GO TO 324
330     CONTINUE
        IRST=IRSTO
        IF(IRST.NE.IR) GO TO 332
        IRS=1
        GO TO 334
332     IRS=-1
334     CONTINUE
        DO 335 K=1,12
335     SDATA(K)=0
        ISUMUV=0
```

```
      IESS=0
      CALL IPOKE(IOUTBF,NC)
C  THIS IS A WAIT LOOP TO BE SURE THE IR IS REPOSITIONED
      DO 336 L=1,15000
336   CONTINUE
C  BEGIN LOOP OF INDIVIDUAL LASER SHOTS
      DO 400 N2=1,128
338   CONTINUE
C  THIS IS THE INTERUPT LOOP
      II=IPEEK(ICSR)
      III=II.AND.IREDB
      IF(III.EQ.0) GO TO 304
C  BEGIN WAIT LOOP FOR THE READY COMMAND
      CALL IDATA(NC,LSS,JDATA(6),JDATA(2),JDATA(3),JDATA(1),IUVSW,
     E  JDATA(4),JDATA(5))
C  CALCULATE THE ELECTRIC FIELD STATUS
      IEST=IE.AND.JDATA(6)
      IF(IEST.NE.IEST0) GO TO 359
      TYPE 901,IK
      TYPE*, ' E MISS'
      GO TO 338
359   CONTINUE
      IEST0=IEST
      IES=-1
      IF(IEST.NE.IE) IES=1
C  CALCULATE THE NEXT UV POLARIZATION
      N3=N3+1
      IF(N3.GT.16) N3=1
      IF(N2.EQ.128) N3=16.*RAN(IRAN,JRAN)
      IUVS=IUVN
      IUVSL=IUVSW
      I1=N3/8
      I2=N3/2
      I3=N3/4
      I3=((1-((-1)**I3))/2)*(N3+1)
      I3=I1+I2+I3
      IUVN=(-1)**I3
      IF(IUVN) 367,368,368
367   IUVSW=0
      GO TO 369
368   IUVSW=2
369   ICONT2=IUVSW+IP
      CALL IPOKE(IOUT2,ICONT2)
C  THE NEXT STATEMENT CLOSES THE WAIT LOOP
      IF(I.EQ.'W') GO TO 338
C  THEN BEGIN CALCULATIONS
      IF (I.EQ.'T') GO TO 395
```

```
      IF(JDATA(3).LT.50) GO TO 390
      IF(JDATA(2).LT.50) GO TO 390
      IF(JDATA(2).GT.2046) GO TO 390
      IF(JDATA(3).GT.2046) GO TO 390
395   CONTINUE
      DATA(1)=JDATA(2)
      DATA(2)=JDATA(3)
      DATA(3)=IES*DATA(1)
      DATA(4)=IES*DATA(2)
      DATA(5)=IUVS*DATA(3)
      DATA(6)=IUVS*DATA(4)
      DATA(7)=IUVS*DATA(1)
      DATA(8)=IUVS*DATA(2)
      DATA(9)=JDATA(1)
      DATA(10)=IUVS*DATA(9)
      DATA(11)=JDATA(4)
      DATA(12)=JDATA(5)
      IF(JDATA(5).EQ.2047) GO TO 409
      IF(DATA(12).GE.2047) DATA(12)=0
      IF(IUVSL.NE.LSS) GO TO 370
      DATA(12)=DATA(12)*IES
      GO TO 372
370   DATA(11)=DATA(11)*MGR-DATA(12)
      DATA(12)=0.
372   CONTINUE
      DO 380 NN=1,12
380   SDATA(NN)=SDATA(NN)+DATA(NN)
      IESS=IESS+IES
      ISUMUV=ISUMUV+IUVS
      GO TO 392
390   TYPE 901,IK
      TYPE*, ' NO SIGNAL
      TYPE*, JDATA(2), JDATA(3)
      GO TO 320
392   CONTINUE
400   CONTINUE
C  THIS IS THE END OF A IR SET . NEED TO SWITCH IR
      IF(N1.EQ.NIR) GO TO 404
      CALL IPOKE(IOUTBF,IRSWIT)
      CALL IPOKE(IOUTBF,NC)
      GO TO 405
404   M1STAT=0
      NC=JTUNE
      CALL IPOKE(IOUTBF,NC)
405   IF(IT.EQ."40000) GO TO 407
      IF(IT.EQ."140000) GO TO 407
      IF(SDATA(12).NE.0.) GO TO 406
```

```
409     TYPE 901,IK
        TYPE*, ' AUXILIARY CELL SATURATION?'
        GO TO 318
406     DATAS(N1,11)=SDATA(11)/SDATA(12)
        GO TO 408
407     DATAS(N1,11)=999.
408     CONTINUE
        DO 410 K=1,10
        DATAS(N1,K)=SDATA(K)
410     CONTINUE
        SCH4=SCH4+SDATA(11)
        SCH5=SCH5+SDATA(12)
        IF(IESS.NE.0) GO TO 411
        IF(ISUMUV.NE.0) GO TO 411
        GO TO 412
411     TYPE 901,IK
        TYPE*, '  SEQUENCE ERROR'
        TYPE*, ISUMUV,NSUMUV,IESS
        GO TO 318
412     CONTINUE
        ISTAT(N1)=IT+IRST+LINST+NO
        IF(IRS.EQ.-1) GO TO 415
        DO 413 N=1,4
        NPL=2*N
        NP1=NPL-1
        D(N)=SDATA(NPL)-SDATA(NP1)
413     T(N)=SDATA(NPL)+SDATA(NP1)
        GO TO 418
415     DO 417 N=1,4
        NPL=2*N
        NP1=NPL-1
        NP2=N+4
        D(NP2)=SDATA(NPL)-SDATA(NP1)
417     T(NP2)=SDATA(NPL)+SDATA(NP1)
418     CONTINUE
        IF((N1/2)*2-N1) 440,420,440
420     N1M=N1-1
        AES=DATAS(N1,3)+DATAS(N1,4)+DATAS(N1M,3)+DATAS(N1M,4)
        AES=AES/(DATAS(N1,1)+DATAS(N1M,1)+DATAS(N1,2)+DATAS(N1M,2))
        AUV=(DATAS(N1,10)+DATAS(N1M,10))/(DATAS(N1,9)+DATAS(N1M,9)+1)
        CALL CALC(DATAS(N1,1),DATAS(N1M,1),DATAS(N1,2),DATAS(N1M,2),
      E DATAS(N1,7),DATAS(N1M,7),DATAS(N1,8),DATAS(N1M,8))
        IF(IT.EQ."140000) GO TO 440
        IF(IT.EQ."40000) GO TO 440
C  RETUNE THE UV LASER NEXT:
        FRAT=((DATAS(N1,11)+DATAS(N1M,11))/SR)*10.-20.
        IRAT=INT(FRAT)
```

```
      IF(IRAT)697,699,697
697   IF(IRAT*JRAT) 695,695,696
695   ITWEAK=ITWEAK*(-1)
      GO TO 694
696   JAB=IABS(JRAT)
      IAB=IABS(IRAT)
      IF(JAB-IAB)695,694,694
694   ITUNE=ITUNE+ITWEAK
      IF(ITUNE.GT.31) GO TO 316
      IF(ITUNE.LT.0) GO TO 316
699   JRAT=IRAT
      JTUNE=ITUNE*2048
      NC=JTUNE+M1STAT
      CALL IPOKE(IOUTBF,NC)
      IF(I.NE.'T') GO TO 500
      IF(IRAT.GE.2) GO TO 320
      IF(IRAT.LE.-2) GO TO 320
      TYPE 901,IR
      TYPE*, ' LINE IS TUNED'
      I='W'
      GO TO 320
440   CONTINUE
C  THIS ENDS THE IR LOOP
500   CONTINUE
C  TIME FOR A PRINTOUT AND A DATA DUMP
      WRITE(12) (ISTAT(J), (DATAS(J,L), L=1,11), J=1,NIR)
      KT=IT
      NO=NO+1
      PAR=2*S(1)/NIR
      EM1=2*S(2)/NIR
      DEL1=2*S(3)/NIR
      DEL2=2*S(4)/NIR
      DIR1=2*S(5)/NIR
      DIR2=2*S(6)/NIR
      IF(IT.NE.0) GO TO 520
      RAT=SCH4/SCH5
      M=M+1
      WRITE(6,902) M, RAT, EM1, PAR
      WRITE(7,906) M,RAT,EM1,PAR,DEL1,DEL2,DIR1,DIR2
      DO 510 K=1,14
      SS(K)=SS(K)+S(K)
      TS(K)=S(K)
510   CONTINUE
      GO TO 200
C  THAT SENDS CONTROL BACK TO BEGIN THE NEXT POINT
520   IP=1
      ICONT2=IUVSW+IP
```

```
      CALL IPOKE(IOUT2,ICONT2)
      IF (IT.NE."40000) GO TO 540
      DO 530 K=1,6
      SB(K)=SB(K)+S(K)
530   TB(K)=S(K)
      NB=NB+1
540   CONTINUE
      TYPE 907,IT,EM1,PAR,DEL1,DEL2,DIR1,DIR2
      PRINT 904,IT,EM1,PAR,DEL1,DEL2
      IF(IT.EQ."140000) GO TO 317
      IF(IT.EQ."100000) GO TO 319
      IT=0
      GO TO 202
900   FORMAT(A)
901   FORMAT(1X,A)
902   FORMAT('0',I4,F10.2,2(2X,F10.7))
904   FORMAT('0',O6,4(2X,F10.7))
907   FORMAT('0',O6,3X,2(2X,F10.7),4(2X,F7.4))
906   FORMAT('0',I2,F7.2,2(2X,F10.7),4(2X,F7.4))
999   CONTINUE
      STOP 'END OF RUN'
      END
      SUBROUTINE CALC(X1,X1M,X2,X2M,X7,X7M,X8,X8M)
C   CALCULATE THE BASIC DATA POINTS ON EVERY SECOND IR SWITCH
      COMMON /BLK1/AUV,AES,D,T,S,IRS
      DIMENSION S(14),D(8),T(8)
      DPPP=(D(1)+D(2)+D(3)+D(4))/(T(1)+T(2)+T(3)+T(4))
      DPPM=(D(1)+D(2)-D(3)-D(4))/(T(1)+T(2)-T(3)-T(4))
      DPMP=(D(1)-D(2)-D(3)+D(4))/(T(1)-T(2)-T(3)+T(4))
      DPMM=(D(1)-D(2)+D(3)-D(4))/(T(1)-T(2)+T(3)-T(4))
      DMPP=(D(5)+D(6)+D(7)+D(8))/(T(5)+T(6)+T(7)+T(8))
      DMPM=(D(5)+D(6)-D(7)-D(8))/(T(5)+T(6)-T(7)-T(8))
      DMMP=(D(5)-D(6)-D(7)+D(8))/(T(5)-T(6)-T(7)+T(8))
      DMMM=(D(5)-D(6)+D(7)-D(8))/(T(5)-T(6)+T(7)-T(8))
      PIRP=(DPPP-DPPM-DPMP+DPMM)/4.
      PIRN=-(DMPP-DMPM-DMMP+DMMM)/4.
      PIRAVE=(PIRP-PIRN)/2.
      PEP=(DPPP-DPPM-DMPP+DMPM)/4.
      PEN=-(DPMP-DPMM-DMMP+DMMM)/4.
      EMIRP=(DPPP+DPPM-DPMP-DPMM)/4.
      PEAVE=(PEP-PEN)/2.
      EMIRN=(-DMPP-DMPM+DMMP+DMMM)/4.
      EMIRA=(EMIRP-EMIRN)/2.
      EMONE=(EMIRP+EMIRN)/2.
      EMEA=(DPPP+DPPM+DPMP+DPMM-DMPP-DMPM-DMMP-DMMM)/8.
      PARITY=(PEP+PEN)/2.
      S(1)=S(1)+PARITY
```

```
      S(13)=S(13)+PARITY**2
      S(2)=S(2)+EMONE
      S(14)=S(14)+EMONE**2
      S(11)=S(11)+PEAVE
      S(12)=S(12)+EMEA
      S(7)=S(7)+PIRAVE
      S(8)=S(8)+ENIRA
      SIN1=1./(X1+X1M)
      SIN2=1./(X2+X2M)
      S(3)=S(3)+(X7M+X7)*SIN1
      S(4)=S(4)+(X8M+X8)*SIN2
      S(5)=S(5)+IRS*(X1-X1M)*SIN1
      S(6)=S(6)+IRS*(X2-X2M)*SIN2
      S(9)=S(9)+AES
      S(10)=S(10)+AUV
      RETURN
      END
      SUBROUTINE LONGPR
      COMMON SS,M,NIR,SB,MB
      DIMENSION SS(14),Q(14),SB(6),QB(6)
      NM1=(NIR*M)/2
      RNM1=1.0/NM1
      DO 800 K=1,12
800   Q(K)=SS(K)*RNM1
      Q(13)=((SS(13)-(Q(1)**2)*NM1)/(NM1-1))**.5
      Q(14)=((SS(14)-(Q(2)**2)*NM1)/(NM1-1))**.5
      PRINT 950,Q(1),Q(13),Q(2),Q(14)
      TYPE 950,Q(1),Q(13),Q(2),Q(14)
      PRINT 950,Q(7),Q(8),Q(11),Q(12)
      TYPE 950,Q(7),Q(8),Q(11),Q(12)
      PRINT 949,Q(9),Q(10),Q(3),Q(4),Q(5),Q(6)
      TYPE 949,Q(9),Q(10),Q(3),Q(4),Q(5),Q(6)
      IF (MB.EQ.0) GO TO 850
      RMB=2.0/(NIR*MB)
      DO 840 K=1,6
840   QB(K)=SB(K)*RMB
      TYPE 949,QB(1),QB(2),QB(3),QB(4),QB(5),QB(6)
      PRINT 949,QB(1),QB(2),QB(3),QB(4),QB(5),QB(6)
850   RETURN
949   FORMAT(1X,6(1X,F10.7))
950   FORMAT(1X,4(1X,F10.7))
      END
      SUBROUTINE START
      COMMON /BLK2/MGR,MSR,NPR1,NPRO
      TYPE*, ' MONITOR GAIN RATIO?'
      PRINT*, 'MONITOR GAIN RATIO?'
      ACCEPT*, MGR
```

```
PRINT*, MGR
TYPE*, ' DESIRED MONITOR SIGNAL RATIO?'
PRINT*, ' DESIRED MONITOR SIGNAL RATIO?'
ACCEPT*,MSR
PRINT*,MSR
TYPE *, ' NUMBER OF PRINTOUTS/LINE? (0-1)'
PRINT *, ' NUMBER OF PRINTOUTS/LINE? (0-1)'
ACCEPT*,NPR1
PRINT*,NPR1
TYPE *, ' NUMBER OF PRINTOUTS/LINE? (0-0)'
PRINT *, ' NUMBER OF PRINTOUTS/LINE? (0-0)'
ACCEPT*,NPR0
PRINT*,NPR0
RETURN
END
```

3. Hanle Effect. Eight time dependent Schrödinger equations were solved numerically, using a fourth order Runge Kutta method, to find the time evolution of the eight coupled $7P_{1/2}$ and $8S_{1/2}$ levels in the presence of a magnetic field and circularly polarized laser field.

```
C  THIS PROGRAM DOES THE HANLE EFFECT BY INTEGRATING EIGHT
C  COUPLED SCHRODINGER EQUATIONS WHICH REPRESENT THE EIGHT
C  HYPERFINE SUBSTATES IN THE 8S AND 7P(1/2) STATES:
C
C
C          S(5)          S(6)          S(7)
C        ------        ------        ------
C
C                      S(8)
C                    ------
C
C
C
C
C         S(1)          S(2)          S(3)
C        ------        ------        ------
C
C                      S(4)
C                    ------
C
      DIMENSION S(8), SZ(8), DUM(8), SA(8), SB(8), SC(8), SD(8)
      REAL MAG
      DIMENSION CON(5),SIN(4),SS(8)
      TYPE *,'ENTER NUMBER OF STEPS, STEP SIZE IN USEC'
      ACCEPT *, NSTEP, DT
      PRINT 200
C      THE NEXT 5 LINES SET UP THE SEQUENCE OF CALCS.
  200 FORMAT('    B   7P8S RATE    P(X)      S(X)      P(Z)      S(Z)')
      DO 41 MR=1,10
      R=MR*100
      DO 40 MA=1,10
      MAG=MA
C  FOR THE 8S STATE, G(F)=1
      Q=6.2*MAG
C  FOR 7P, G(F)=1/3
      P=2.05*MAG
      V=(SQRT(R*(R+43.6)))/2.51
      CON(1)=P
      CON(2)=Q
      CON(3)=V
      CON(4)=21.4
      CON(5)=43.6
C  CON(4)=GAMMA(7P)/2;  CON(5)=GAMMA(8S)/2.
      DO 50 J=1,4
      SINT=0.
      T=0.
      SSS=0.
```

```
      SSP=0.
      IW=-1
      GO TO (51,52,53,54), J
C     BRANCH HERE IF P(X)=+1
   51 S(1)=.5
      S(2)=.707
      S(3)=.5
      S(4)=0.
      GO TO 55
C   BRANCH HERE IF P(X)=-1
   52 S(1)=.5
      S(2)=-.707
      S(3)=.5
      S(4)=0.
      GO TO 55
C   BRANCH HERE IF P(Z)=+1
   53 S(1)=1.
      S(2)=0.
      S(3)=0.
      S(4)=0.
      GO TO 55
C   BRANCH HERE IF P(Z)=-1
   54 S(1)=0.
      S(2)=0.
      S(3)=1.
      S(4)=0.
   55 CONTINUE
      S(5)=0.
      S(6)=0.
      S(7)=0.
      S(8)=0.
      DO 30 NN=1,NSTEP
C  INTEGRATE THE EQUATIONS ONE STEP BY RUNGA CUTTA
      DO 10 N10=1,8
      MM=N10
      SA(N10)=DOT(MM,S,CON)*DT
C     TYPE *,MM,N10,SA(MM)
   10 CONTINUE
      DO 11 N11=1,8
      DUM(N11)=S(N11)+SA(N11)*.5
   11 CONTINUE
      DO 12 N12=1,8
      MM=N12
      SB(N12)=DOT(MM,DUM,CON)*DT
   12 CONTINUE
      DO 13 N13=1,8
      DUM(N13)=S(N13)+.5*SB(N13)
```

```
   13 CONTINUE
      DO 14 N14=1,8
      MM=N14
      SC(N14)=DOT(MM,DUM,CON)*DT
   14 CONTINUE
      DO 15 N15=1,8
      DUM(N15)=S(N15)+SC(N15)
   15 CONTINUE
      DO 16 N16=1,8
      MM=N16
      SD(N16)=DOT(MM,DUM,CON)*DT
   16 CONTINUE
      DO 17 N17=1,8
      S(N17)=S(N17)+(SA(N17)+2.*SB(N17)+2.*SC(N17)+SD(N17))/6
   17 CONTINUE
      T=T+DT
C    SQUARE THE LEVELS
      DO 20 N20=1,8
      SS(N20)=S(N20)*S(N20)
   20 CONTINUE
      SSS=SS(5)+SS(6)+SS(7)+SS(8)
      SSP=SS(1)+SS(2)+SS(3)+SS(4)
D     TYPE *,SSP
C   INTEGRATE BY SIMPSON'S RULE
      IW=IW*-1
      INT=3+IW
      SINT=SINT+INT*SSS*DT*43.6/3.
   30 CONTINUE
      SIN(J)=SINT
      SINT=0.
   50 CONTINUE
      POL=(SIN(1)-SIN(2))/(SIN(1)+SIN(2))
      SIG=(SIN(1)+SIN(2))/2.
      POLM=(SIN(3)-SIN(4))/(SIN(3)+SIN(4))
      SIGM=(SIN(3)+SIN(4))/2.
      TYPE *,MAG,R,POL,SIG,POLM,SIGM
      PRINT 100,MAG,R,POL,SIG,POLM,SIGM
  100 FORMAT (' ',2F6.0,4F10.5)
   40 CONTINUE
   41 CONTINUE
      END
      FUNCTION  DOT(NF,SZ,CON)
      DIMENSION SZ(8),CON(5)
      P=CON(1)
      Q=CON(2)
      V=CON(3)
      GP=CON(4)
```

```
      GS=CON(5)
      GO TO (1,2,3,4,5,6,7,8), NF
    1 DRIP=P*SZ(2)+V*(SZ(6)-SZ(8))-GP*SZ(1)
      GO TO 9
    2 DRIP=V*SZ(7)-SZ(2)*GP+SZ(3)*P-SZ(1)*P
C     TYPE *,P,SZ(3),SZ(1),V,SZ(7),GP,SZ(2),DRIP
      GO TO 9
    3 DRIP=-P*SZ(2)-GP*SZ(3)
      GO TO 9
    4 DRIP=V*SZ(7)-GP*SZ(4)
      GO TO 9
    5 DRIP=Q*SZ(6)-GS*SZ(5)
      GO TO 9
    6 DRIP=Q*(SZ(7)-SZ(5))-V*SZ(1)-GS*SZ(6)
      GO TO 9
    7 DRIP=-Q*SZ(6)-V*(SZ(2)+SZ(4))-GS*SZ(7)
      GO TO 9
    8 DRIP=+V*SZ(1)-GS*SZ(8)
      GO TO 9
    9 CONTINUE
      DOT=DRIP
      END
```

REFERENCES

Abers, E. S. and B. W. Lee, 1973, Phys. Lett. C 9C, 1.

Abramowitz, M., and I. A. Stegan, 1964, Handbook of Mathematical Functions, AMS 55, Nat. B. of Stand.

Baird, P.E.G., et al., 1977, Phys. Rev. Lett., 39, 98.

Barkov, L. M. and M. S. Zolotorev, 1979, Phys. Lett. 85B, 308.

Beg, M.A.B. and A. Sirlin, 1974, Ann. Rev. Nuc. Sci. 24, 379.

Benvenuti, A., et al., 1974, Phys. Rev. Lett. 32, 800.

Bouchiat, C., 1975, Phys. Lett. 57B, 284.

Bouchiat, M. A. and C. Bouchiat, 1974a, Phys. Lett. 40B, 111.

Bouchiat, M. A. and C. Bouchiat, 1974b, J. de Physique, 35, 889.

Bouchiat, M. A. and C. Bouchiat, 1975, J. de Physique, 36, 493.

Bouchiat, M. A. and L. Pottier, Proc. Workshop on Parity Violation in Atoms, Cargese, Sept. 1979, in press.

Chu, S., 1976, LBL Rep. 5731 (Ph.D. Thesis), Lawrence Berkeley Laboratory.

Chu, S., E. D. Commins, and R. Conti, 1977, Phys. Lett. 60A, 96.

Chu, S., and E. D. Commins, 1977, Appl. Optics, 16, 2619.

Chu, S., and R. Smith, 1979, Opt. Commun. 28, 221.

Cline, D., and W. Fry, 1977, Ann. Rev. Nuc. Sci. 27, 209.

Conti, R., 1979, Ph.D. Thesis (unpublished).

Conti, R., P. Bucksbaum, S. Chu, E. Commins, and L. Hunter, 1979, Phys. Rev. Lett. 42, 343.

Commins, E., 1973, Weak Interactions, New York: cGraw Hill.

Commins, E., 1978, University of California course on gauge theories, unpublished.

Commins, E., and P. Bucksbaum, 1980, Ann. Rev. Nuc. and Part. Sci. 30, 1.

De Rujula, A., 1975, Proc. of the First Formigal Winter School on Fundamental Physics.

Drell, P. and S. Chu, 1979, Opt. Commun. 28, 343.

Fair 1979, Phys. Lett. 82B, 97.

Flusberg, A., and T. Mossberg, 1976, Phys. Rev. A14, 2146.

Fowler, W., 1977, in Unification of Elementary Forces and Gauge Theories, ed. D. B. Cline and F. E. Mills, London: Harwood.

Gardner, M., 1964, The Ambidextrous Universe, New York: Basic Books.

Glashow, S. L., J. Iliopoulos, and L. Miani, 1970, Phys. Rev. D2, 1285.

Gould, H., 1970, Phys. Rev. Lett. 24, 1091.

Gribov, V., and B. Pontecorvo, 1969, Phys. Lett. 28B, 493.

Handbook of Chemistry and Physics, 1965, ed., R. Weast, Cleveland: Chem. Rubber Co.

Harris, R. A., and L. Stodolsky, 1978, Phys. Lett. B, 78B, 313.

Harris, S., 1969, Proc. IEEE 57, 2096.

Hasert, F. J., et al., 1973, Phys. Lett. 46B, 138.

Higgs, P. W., 1964a, Phys. Lett. 12, 132.

Higgs, P. W., 1964b, Phys. Rev. Lett. 13, 508.

Higgs, P. W., 1966, Phys. Rev. 145, 1156.

Hinds, E. A., C. E. Loving, P.G.H. Sandars, 1976, Phys. Lett. 62B, 97 (1976).

Hung, P. Q., and J. J. Sakurai, 1977a, Phys. Lett. 6[illegible]B, 323.

Hung, P. Q., and J. J. Sakurai, 1977b, Phys. Lett. 7[illegible]B, 208.

Iliopoulos, J., 1976, CERN Rep. 76-11.

Kasha, M., 1948, J. Opt. Soc. Am. 38, 929.

Khriplovich, I. B., V. N. Novikov, O. P. Sushkov, 197[illegible], Sov. Phys. (JETP) 44, 872.

Lee, T. D., and C. N. Yang, 1956, Phys. Rev. 104, 254.

Lewis, L. L., et al., 1977, Phys. Rev. Lett. 39, 795.

Neuffer, D. V., and E. Commins, 1977a, Phys. Rev. A16, 844.

Neuffer, D. V., and E. Commins, 1977b, Phys. Rev. A16, 1760.

Newman, H. H., 1940, Multiple Human Births, Chapter 5, New York: Doubleday.

Pasierb, E., et al., 1979, Phys. Rev. Lett. 43, 96.

Player, M. A., and P.G.H. Sandars, 1970, J. Phys. B., 3, 1620.

Prescott, C. Y., et al., 1978, Phys. Lett 77B, 347.

Sakurai, J. J., 1964, Invariance Principles and Elementary Particles, Princeton: Princeton University Press.

Sakurai, J. J., 1967, Advanced Quantum Mechanics, Reading, MA: Addison Wesley.

Sakurai, J. J., 1979, UCLA Rep/78/TEP/27 University of California at Los Angeles.

Salam, A., 1968, in Relativistic Groups and Analyticity (Nobel Symposium No. 8), ed. N. Svartholm, Stockholm: Almqvist and Wiksell.

Sandars, P.G.H., 1968, J. Phys. B1, 499.

Sobelman, I. I., et al., 1980, Quantum Radiophysics Laboratory Preprint 43, Lebedev Physical Institute.

Tietz, T., 1954, J. Chem. Phys. 22, 2094.

Weinberg, S., 1967, Phys. Rev. Lett. 19, 1264.

Weinberg, S., 1972, Phys. Rev. D, 5, 1412.

Weinberg, S., 1974, Rev. Mod. Phys. 46, 255.

Wu, C. S. et al., 1957, Phys. Rev. 105, 1413.

Yang, C. N. and R. N. Mills, 1954, Phys. Rev. 96, 191.

Yariv, A., 1975, Quantum Electronics, 2nd ed., New York: John Wiley.